Light Harvesting and Energy Transfer in Metal-Organic Frameworks

Shaunak Mehboob Shaikh

Dissertation submitted to the faculty of the Virginia Polytechnic Institute and State University in partial fulfillment of the requirements for the degree of

Doctor of Philosophy

in

Chemistry

Amanda J. Morris, Chair

James M. Tanko

Diego Troya

Feng Lin

May 7th, 2021

Blacksburg, VA

Key words: Metal-Organic Frameworks, pyrenes, porphyrins, excitation energy transfer, interchromophoric distance, orientation factor

Light Harvesting and Energy Transfer in Metal-Organic Frameworks

Shaunak Mehboob Shaikh

Abstract

A key component of natural photosynthesis are the antenna chromophores (chlorophylls and carotenoids) that capture solar energy and direct it towards the reaction centers of photosystems I and II. Highlighted by highly-ordered crystal structures and synthetic tunability via crystal engineering, metal–organic frameworks (MOFs) have the potential to mimic the natural photosynthetic systems in terms of the efficiency and directionality of energy transfer. Owing to their larger surface areas, MOFs have large absorption cross sections, which amplifies the rate of photon collection. Furthermore, MOFs can be constructed using analogues of chlorophyll and carotenoids that can participate in long-range energy transfer. Herein, we aimed to design photoactive MOFs that can execute one of the critical steps involved in photosynthesis - photon collection and subsequent energy transfer.

The influence of spatial arrangement of chromophores on the efficiency and directionality of excitation energy transfer (EET) was investigated in a series of mixed-ligand pyrene- and porphyrin-based MOFs. Due to the significant overlap between the emission spectrum of 1,3,6,8-tetrakis(p-benzoic acid)pyrene (TBAPy) and the absorption spectrum of meso-tetrakis(4-carboxyphenyl)porphyrin (TCPP), the co-assembly of these two ligands in a MOF should enable facile energy transfer. Bearing this in mind, three TBAPy-based MOFs with markedly different network topologies (ROD-7, NU-901, and NU-1000) were chosen and a small number of TCPP units were incorporated in their backbone. To gain insight into the photophysical properties of mixed-ligand MOFs, we conducted time-resolved and steady-state fluorescence measurements on them. Stern-Volmer analysis was performed on the fluorescence lifetime data of mixed-ligand

MOFs to determine the Stern-Volmer quenching constants (K_{SV}). K_{SV} values for ROD-7, NU-901, NU-1000, and TBAPy solution were found to be 15.03 ± 0.82 M^{-1}, 10.25 ± 0.99 M^{-1}, 8.16 ± 0.41 M^{-1}, and 3.35 ± 0.30 respectively. In addition, the ratio of the fluorescence intensities of TCPP and TBAPy (I_{TCPP}/I_{TBAPy}) was used to calculate the EET efficiencies in each of the three MOFs. EET efficiencies were in the following order: ROD-7 > NU-901 > NU-1000 > TBAPy-solution. Based on the trends observed for K_{SV} and EET efficiencies, two conclusions were drawn: (1) the ligand-to-ligand energy transfer mechanism in MOFs outperforms the diffusion-controlled mechanism in solution phase, (2) energy transfer in MOFs is influenced by their structural parameters and spectral overlap integrals. The enhanced EET efficiency in ROD-7 is attributed to shorter interchromophoric distance, larger orientation factor, and larger spectral overlap integral. Directionality of energy transfer in these MOFs was assessed by calculating excitonic couplings between neighboring TBAPy linkers using the atomic transition charges approach. Rate constants of EET (k_{EET}) along different directions were determined from the excitonic couplings. Based on the k_{EET} values, ROD-7 is expected to demonstrate highly anisotropic EET along the stacking direction.

In order to explore the mechanistic aspects of EET in porphyrin-based MOFs, we studied the energy transfer characteristics of PCN-223, a zirconium-based MOF containing TCPP ligands. After performing structural characterization, the photophysical properties of PCN-223 and free TCPP were investigated using steady state and time-resolved spectroscopy. pH-dependent fluorescence quenching experiments were performed on both the MOF and ligand. Stern-Volmer analysis of quenching data revealed that the quenching rate constants (k_Q) for PCN-223 and TCPP were $8.06 \times 10^{11}\ M^{-1}s^{-1}$ and $2.71 \times 10^{10}\ M^{-1}s^{-1}$ respectively. The quenching rate constant for PCN-223 is, therefore, an order of magnitude larger than that for TCPP. Additionally, PCN-223

demonstrated a substantially higher extent of quenching (Φ_q = 93%) as compared to free TCPP solution (Φ_q = 51%), at similar concentrations of quencher. The higher extent of quenching in MOF is attributed to energy transfer from neutral TCPP linkers to N-protonated TCPP linkers. Using the Förster energy transfer model, the rate constant of EET in PCN-223 was calculated. The magnitude of rate constant was in good agreement with the k_{EET} values reported for other porphyrin-based MOFs. Nanosecond transient absorption measurements on PCN-223 revealed the presence of a long-lived triplet state (extending beyond 200 μs) that exhibits the characteristic features of a TCPP-based triplet state. The lifetime of MOF is shorter than that of free ligand, which may be attributed to triplet-triplet energy transfer in the MOF. Lastly, femtosecond transient absorption spectroscopy was employed to study the ultrafast photophysical processes taking place in TCPP and PCN-223. Kinetic analysis of the femtosecond transient absorption data of TCPP and PCN-223 showed the presence of three distinct time components that correspond to: (a) solvent-induced vibrational reorganization of excitation energy, (b) vibrational cooling, and (c) fluorescence.

Materials that allow control over the directionality of energy transfer are highly desirable. Core-shell nanocomposites have recently emerged as promising candidates for achieving long-distance, directional energy transfer. For our project, we aim to employ UiO-67-on-PCN-222 composites as model systems to explore the possibility of achieving directional energy transfer in MOF-based core-shell structures. The core–shell composites were synthesized by following a previously published procedure. Appropriate amounts of Ruthenium(II) tris(5,5′-dicarboxy-2,2′-bipyridine), RuDCBPY, were doped in the shell layer to produce a series of Ru-UiO-67-on-PCN-222 composites with varying RuDCBPY loadings (**CS-1**, **CS-2**, and **CS-3**). The RuDCBPY-doped core–shell composites were characterized by powder X-ray diffraction (PXRD), scanning electron

microscopy (SEM) imaging, N_2 adsorption-desorption isotherms, and diffuse reflectance spectroscopy. Efforts are currently underway to quantify RuDCBPY loadings in **CS-1**, **CS-2**, and **CS-3**. After completing structural characterization, the photophysical properties of **CS-1**, **CS-2**, and **CS-3** will be investigated with the help of time-resolved and steady-state fluorescence spectroscopy.

Light Harvesting and Energy Transfer in Metal-Organic Frameworks

Shaunak Mehboob Shaikh

General Audience Abstract

The pigment−protein complexes in natural photosynthetic units (also known as light harvesting antennas) efficiently capture solar energy and transfer this energy to reaction centers that carry out water splitting reactions. The collective chromophoric behavior of antennas can be replicated by metal-organic frameworks (MOFs). MOFs are crystalline, self-assembled materials composed of metal clusters connected by organic molecules. In this dissertation, we study the factors that govern the energy transfer and light harvesting capabilities of MOFs. In chapter 2, we examined the role of 3D structure of MOFs in energy transfer. In chapter 3, we investigated the influence of pH and temperature on the photophysical properties of MOFs. In chapter 4, we explored the possibility of energy transfer in novel MOF-on-MOF composites. This work is intended to pave the way for the construction of highly efficient MOF-based materials that can serve as the light harvesting and energy-transfer components in solar energy conversion devices.

Acknowledgements

To begin with, I owe a deep sense of gratitude towards my advisor, Dr. Amanda J. Morris. Thank you for believing in me and for your continued support throughout my time in graduate school. Under your guidance, I was able to grow as an independent researcher and explore ideas that interested me. I would also like to thank you for all that you taught me since the time I started as a graduate student and for guiding me in difficult situations.

I am also very grateful to Dr. James Tanko, Dr. Diego Troya and Dr. Feng Lin for your input as members of my committee and for your insightful feedbacks. I am also very thankful to Dr. Nicholas Mayhall for introducing me to computational chemistry and for being patient with me when I was a new graduate student.

I would like to extend my gratitude towards Dr. Arnab Chakroborty and Dr. Pavel Usov, previous post-docs in Morris groups, for helping me with my experiments and providing valuable guidance. I am also thankful to all the current and previous members of Morris group for helping me in my research efforts and for your friendship. I am also grateful to all the staff and faculty members at the Department of Chemistry, Virginia Tech for their help and support.

There have been many ups and downs during my time as a graduate student. I am forever grateful to my mother Salma Shaikh and my father Mehboob Shaikh for providing unwavering support and encouragement during all times. It would not have been possible without your love and support.

Table of Contents

Attributions

Chapter 2 of this dissertation is adapted from a manuscript that will submitted to the *Journal of Physical Chemistry C*. Shaunak M. Shaikh synthesized and characterized the mixed-ligand MOFs, and performed all the steady-state and time-resolved fluorescence measurements. He also submitted time-dependent density functional theory (TDDFT) calculations for computing excitonic couplings and the rates of energy transfer. He analyzed experimental and computational data, and wrote the manuscript. Xiaozhou Yang performed SEM imaging experiments. Dr. Elena Jakubikova provided the direction and insight necessary to conduct the TDDFT calculations, and provided guidance for the calculation of excitonic couplings. Dr. Amanda J. Morris, principal investigator, supervised the research project, assisting with technical insight and direction during the investigation. She also assisted in writing and editing the manuscript.

The third chapter is adapted from a manuscript published in *Faraday Discussion*s. Shaunak M. Shaikh synthesized and characterized PCN-223 MOF samples, and performed the steady-state and time-resolved fluorescence measurements. Arnab Chakraborty assisted with nanosecond transient absorption measurements and helped with the analysis of fluorescence quenching data. Jamie Alatis assisted with synthesis and fluorescence measurements. Meng Cai performed SEM imaging experiments. Dr. Evgeny Danilov performed femtosecond transient absorption measurements and helped in analyzing the data. Dr. Amanda J. Morris, principal investigator, supervised the research project, assisting with technical insight and direction during the investigation. She also assisted in writing and editing the manuscript.

The fourth chapter is based on a manuscript in preparation. Shaunak M. Shaikh synthesized and characterized the MOF-in-MOF composites. He also performed all the steady-state and time-resolved fluorescence measurements. Stefan Ilic assisted with the synthesis of Ruthenium(II)

tris(5,5′-dicarboxy-2,2′-bipyridine). Xiaozhou Yang performed all the SEM imaging experiments. Bradley Gibbons assisted with nitrogen gas adsorption measurements. Dr. Amanda J. Morris, principal investigator, supervised the research project, assisting with technical insight and direction during the investigation. She also assisted in writing and editing the manuscript.

1. Dependence of Excitation Energy Transfer on Photophysical Properties and Structural Parameters: From Molecular Systems to Metal-Organic Frameworks

1.1 Introduction

Light harvesting antenna complexes (LHC's) in natural photosynthetic systems demonstrate a highly efficient excitation energy transfer (EET) process that delivers absorbed photons to the reaction centers (PSI and PSII) with efficiencies exceeding 95%.[1] The structural arrangement of chlorophyll and carotenoid pigments integrated within the LHC's generates an energy gradient, which ensures directional migration of excitation energy to the reaction centers. Over the last few decades, scientists have dedicated significant research effort towards designing artificial light harvesting systems that can mimic the highly efficient energy transfer machinery in LHC's. In order to mimic LHC's, it is critical to first understand how the chemical composition and structural arrangement of pigment chromophores influence the efficiency and directionality of energy transfer in LHC's. More specifically, there is a need to investigate how the photophysical properties of pigment chromophores and the structural parameters of LHC's (such as the position, separation distance and the relative orientation of pigment chromophores) affect the energy transfer process. This has inspired scientists to design a wide variety of molecular and supramolecular constructs that can serve as model systems for studying energy transfer.[1,2,6,11-22] The aim of this chapter is to highlight some of the prominent artificial systems that have aided the scientific community in understanding the factors that govern energy transfer. Before delving into examples of these systems, it is necessary to gain a good understanding of the mechanistic aspects of energy transfer.

1.2 Mechanistic Aspects of Energy Transfer

Resonance energy transfer (RET) is a non-radiative process where the excited state energy of a donor molecule is transferred to the ground state of an acceptor molecule that lies in close proximity.[2] The transfer of energy leads to the formation of an excited state acceptor and a ground state donor (Figure 1).[3–5] Energy transfer in MOFs can be described using two different models (a) Dexter resonance energy transfer (DRET) and (b) Förster resonance energy transfer (FRET).

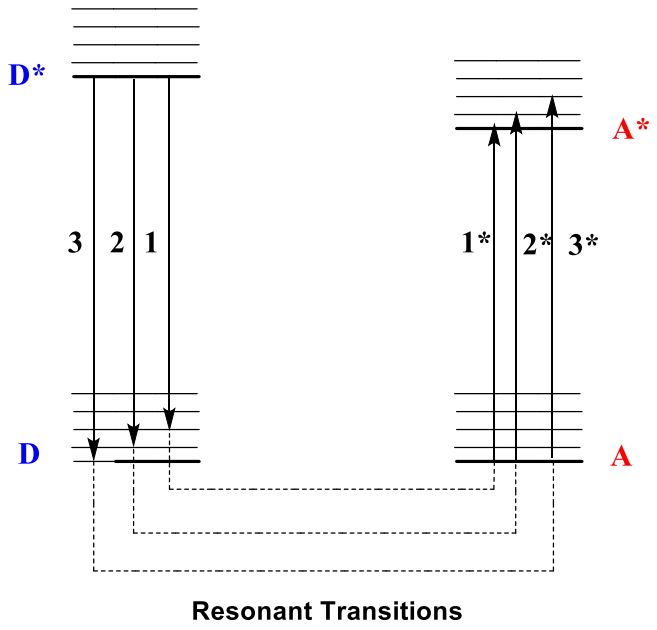

Figure 1. Energy diagram showing coupled transition between an excited state donor, D*, and ground state acceptor, A. Reproduced from reference 2 with permission.

1.2.1 Dexter resonance energy transfer

Dexter resonance energy transfer (DRET) is a process in which the donor and acceptor bilaterally exchange their electrons (Figure 2).[6] Dexter transfer requires significant overlap between the orbitals of donor and acceptor, which means that it can only occur over very short distances (< 10 Å). The rate of DRET has an exponential dependence on the donor-acceptor distance and is given by equation 1,

$$k_{DRET} = k_0 exp\left(\frac{-2\,(r - R_0)}{L}\right) \quad (1)$$

where r is the separation distance between the donor and acceptor, R_0 is the distance between donor and acceptor at which efficiency of resonance energy transfer (RET) is 50%, k_0 is the limiting energy transfer rate constant, and L the Van der Waals contact distance between the donor and acceptor.[6]

1.2.2 Förster resonance energy transfer

Förster resonance energy transfer (FRET) is dictated by the coulombic interactions between the transition dipoles of donor and acceptor (Figure 2).[3,4,6] The coulombic coupling between the two interacting molecules can take place over distances up to 100 Å. The efficiency of Förster transfer is proportional to the extent of coupling between the D*→D and A→A* transition dipoles, which is quantitatively evaluated as the overlap integral between the absorption spectrum of the acceptor and the emission spectrum of donor molecule (*J*). The overlap integral is mathematically presented in equation 2,

$$J = \frac{\int_0^\infty \mathrm{I_D}(\lambda)\varepsilon_\mathrm{A}(\lambda)\lambda^4\,\mathrm{d}\lambda}{\int_0^\infty \mathrm{I_D}\,(\lambda)\,\mathrm{d}\lambda} \quad (2)$$

Where λ is the wavelength, $\varepsilon_A(\lambda)$ is the absorption spectrum of acceptor molecule (in terms of extinction coefficient) and $I_D(\lambda)$ is the emission spectra of the donor molecule. The Förster model predicts that the rate constant of energy transfer is proportional to the inverse of sixth power of the distance between the donor and the acceptor molecule (eq. 3),

$$k_{FRET} = k_D\left(\frac{R_0}{R}\right)^6 = \frac{1}{\tau_D}\left(\frac{R_0}{R}\right)^6 \quad (3)$$

where k_D is the emission rate constant of donor in absence of acceptor, τ_D is the lifetime of donor in absence of acceptor, R is the separation distance between the donor and acceptor, and R_0 is the

distance at which the energy transfer efficiency is 50%. Also known as Förster distance, R_0 is given by eq. 4,

$$R_0 = \left(\frac{9000(\ln 10)\kappa^2 \Phi_D J}{128\pi^5 N_A \eta^4}\right) \quad (4)$$

where Φ_D is the fluorescence quantum yield of the donor in the absence of the acceptor, J is the spectral overlap integral, κ^2 describes the relative orientation of the transition dipole moments between the acceptor and the donor molecule, η is the refractive index of the medium, and N_A is the Avogadro number.

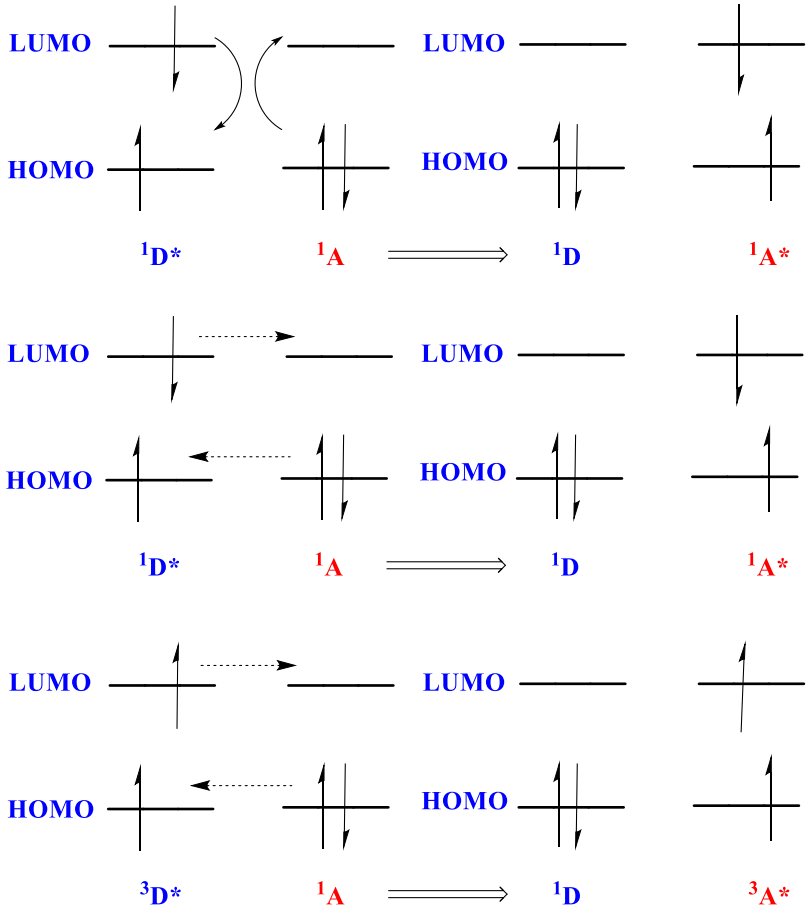

Figure 2. Förster and Dexter energy transfer. (Top) Singlet-singlet Förster energy transfer. (Middle) Singlet-singlet Dexter energy transfer. (Bottom) Singlet-triplet Dexter energy transfer. Reproduced from reference 2 with permission.

1.2.3 Factors affecting resonance energy transfer

Resonance energy transfer in MOFs is governed by several factors:

1. Extent of overlap between the emission spectrum of donor and absorption spectrum of acceptor. Energy transfer is favored in donor-acceptor systems with large spectral overlaps.
2. Separation distance between donor and acceptor molecules.
3. Relative orientation between the transition dipoles of donor and acceptor. The orientation factor, κ^2, gives the quantitative value of interaction between the two dipole moments. κ^2 values can range from 0 (when dipoles are perpendicular to each other) to 4 (when dipoles are collinear).

   The orientation factor can be determined using eq. 5,

   $$\kappa^2 = [\cos\gamma - 3\cos\alpha\cos\beta]^2 \quad (5)$$

   where α and β are the angles made by the transition dipoles of donor and acceptor with the line joining their centers, and γ is the angle between the two transition dipoles.
4. Concentration ratios of donor and acceptor ([Donor]/[Acceptor])
5. Emission lifetime and quantum yield of donor

1.3 Energy Transfer in Rhenium-based Polynuclear Complexes

The McCusker group have done pioneering work on rhenium-based polynuclear assemblies to investigate the effect of overlap integral, donor-acceptor separation distance, and orientation factor on energy transfer.[7–10] In one of their seminal papers, they reported the synthesis, structure, and photophysical properties of a family of covalently linked assemblies containing Re^{I}-bipyridyl donors and Cu^{II}-acetylacetonate acceptors (Figure 3).[7] The general molecular formula of the complexes is $[Cu(pyacac)_2(Re(bpy')(CO)_3)_2](OTf)_2$ (where pyacac = 3-(4-pyridyl)-acetylacetonate and bpy′ = 4,4′-5,5′-tetramethyl-2,2′-bipyridine (tmb, **1**), 4,4′-dimethyl-2,2′-

bipyridine (dmb, **2**), 2,2′-bipyridine (bpy, **3**), 4,4′-dichloro-2,2′-bipyridine (dclb, **4**), and 4,4′-diethylester-2,2′-bipyridine (deeb, **5**)). These complexes are geometrically well-defined systems in which the donor and acceptor transition dipoles, and hence the orientation factor κ^2, can be explicitly determined. Moreover, variations in the emission energy afforded by the different bipyridyl ligands attached to the Re^{I} metal center provide for systematic modulation of the donor-acceptor spectral overlap. A series of structurally analogous "reference" compounds were also prepared by replacing the Cu^{II}-acetylacetonate group with the electronically benign Be^{II}-acetylacetonate group (**6-10,** Figure 3). Energy transfer between the Re^{I}-bipyridyl and Be^{II}-acetylacetonate groups is expected to be negligible (due to the minimal electronic coupling between the two groups).

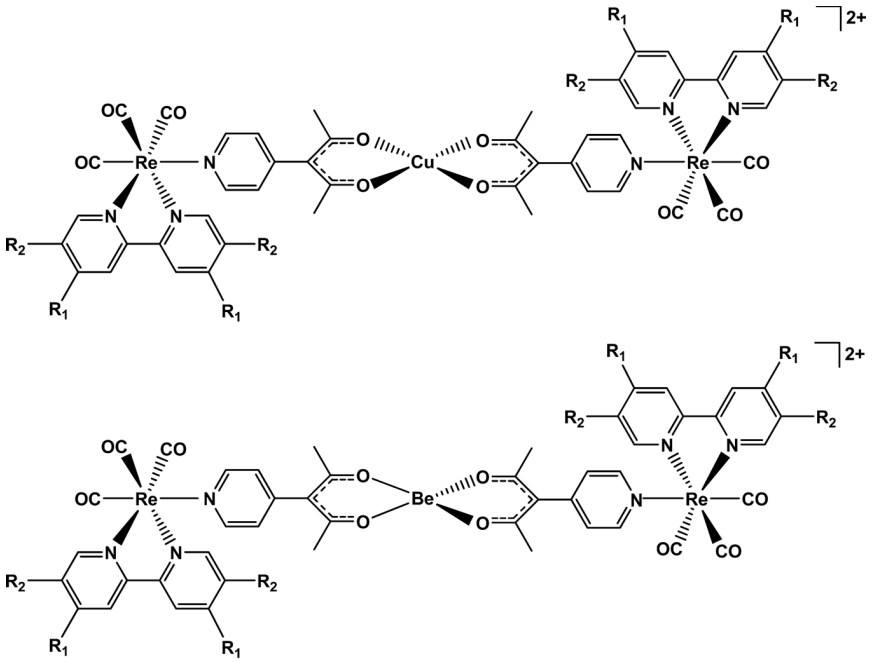

Figure 3. Structures of $CuRe_2$ (1-5) and $BeRe_2$ (6-10) complexes. Reproduced from reference 7 with permission.

Table 1. Calculated energy transfer rate constants (k_{EET}), spectral overlap integrals (J) and orientation factors for complexes **1**−**5.** Adapted from reference 7.

	k_{EET} ($\times 10^8$ s^{-1})	J (10^{-16} M^{-1} cm^3)	Effective κ^2
$[Cu(pyacac)_2(Re(tmb)(CO)_3)_2](OTf)_2$ (**1**)	0.67	4.29	1.00
$[Cu(pyacac)_2(Re(dmb)(CO)_3)_2](OTf)_2$ (**2**)	1.18	5.14	1.18
$[Cu(pyacac)_2(Re(bpy)(CO)_3)_2](OTf)_2$ (**3**)	1.18	5.52	1.32
$[Cu(pyacac)_2(Re(dclb)(CO)_3)_2](OTf)_2$ (**4**)	1.71	6.68	2.04
$[Cu(pyacac)_2(Re(deeb)(CO)_3)_2](OTf)_2$ (**5**)	1.96	7.09	2.04

Time-resolved emission measurements were conducted to determine the excited-state lifetimes (τ_{obs}) of $CuRe_2$ (**1-5**) and $BeRe_2$ (**6-10**) complexes. The energy transfer rate constants (k_{EET}) for **1**−**5** were then calculated using the lifetime data (eq. 6),

$$k_{\mathrm{EET}} = k_{\mathrm{obs}}^{\mathrm{CuRe_2}} - k_{\mathrm{obs}}^{\mathrm{BeRe_2}} = \frac{1}{\tau_{\mathrm{obs}}^{CuRe_2}} - \frac{1}{\tau_{\mathrm{obs}}^{BeRe_2}} \quad (6)$$

The k_{EET} values of **1-5** were found to be sensitive to the spectral overlap integrals and orientation factors (Table 1). Based on the trends observed in Table 1, it was concluded that a substantially large spectral overlap, coupled with favorable alignment of the transition dipoles of donor and acceptor (larger κ^2 value) results in faster energy transfer between Re^I-bipyridyl and Cu^{II}-acetylacetonate moieties.

1.4 Energy Transfer in Covalently-linked Donor-Acceptor Systems

The Förster resonance energy transfer theory postulates that energy transfer is critically dependent on the distance and mutual orientation between the donor and acceptor moieties. Energy-transfer studies performed on judiciously designed, covalently-linked donor-acceptor

systems provide further experimental validation to these theoretical predictions. For example, Albinsson and co-workers investigated how the donor−acceptor edge-to-edge distance, R_{DA}, affects the rate and efficiency of triplet excitation energy transfer (TEET) in a series of donor−bridge−acceptor (D−B−A systems), ZnP−xB−H_2P (x = 2, 3, 4, and 5).[11] In these systems a zinc(II) 5,15-diaryl-2,8,12,18-tetraethyl-3,7,13,17-tetramethylporphyrin (ZnP) acts as the donor and the corresponding free-base porphyrin (H_2P) acts as the acceptor of the triplet excitation energy (Figure 4). The donor and acceptor chromophores are separated by oligo-p-phenyleneethynylene (OPE) bridge units where the number of phenyleneethynylene groups varies between 2 and 5, giving rise to edge-to-edge separations ranging between 12.7 and 33.4 Å. To investigate the distance dependence of the rate and efficiency of TEET in the ZnP−xB−H_2P systems, transient absorption measurements were performed and lifetimes corresponding to ZnP moiety in the D−B−A compounds were determined. The experimental rates and efficiencies of TEET in ZnP−xB−H_2P systems were estimated using eq. 7 and 8 respectively. Table 2 lists the lifetimes of the ZnP moieties in D−B−A systems along with the TEET rates (k_{TEET}) and efficiencies (TEET). k_{TEET} demonstrated an exponential distance dependence, indicating that TEET is governed by either a Dexter or a superexchange mechanism.[12] Figure 5 shows the logarithm of the TEET rate constant versus the donor−acceptor edge-to-edge distance, R_{DA}.

$$k_{TEET} = \frac{1}{\tau_{\mathrm{ZnP-xB-H2P}}} - \frac{1}{\tau_{\mathrm{ZnP}}} \tag{7}$$

$$\mathrm{E_{TEET}} = 1 - \frac{\tau_{\mathrm{ZnP}}}{\tau_{\mathrm{ZnP-xB-H2P}}} \tag{8}$$

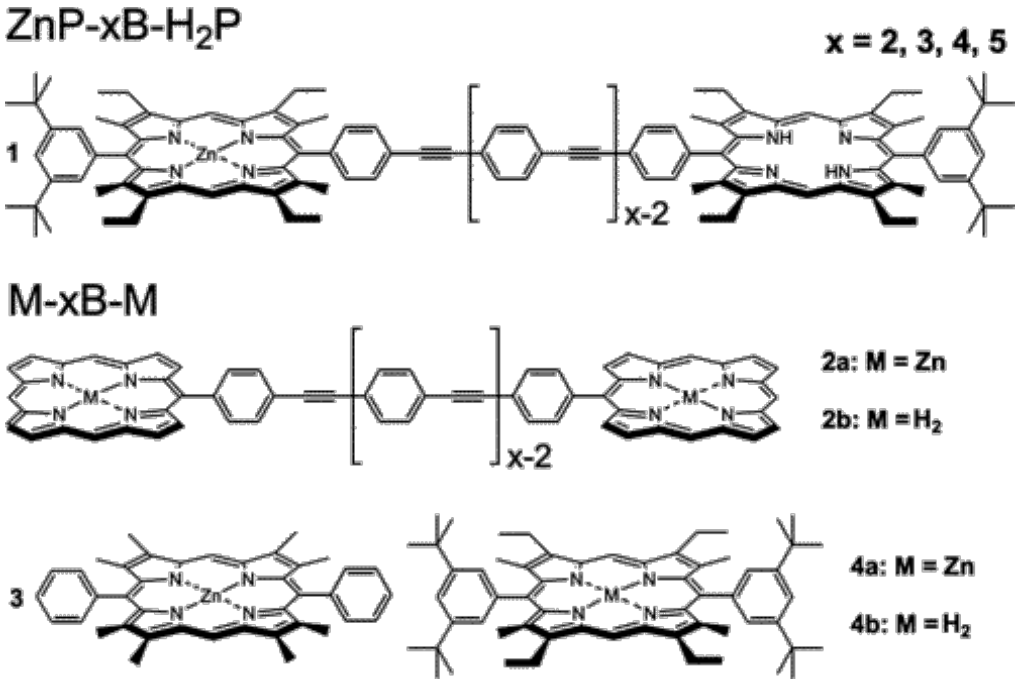

Figure 4. The Donor (ZnP)−Bridge (xB)−Acceptor (H_2P) Systems (1), Model Systems Zn−xB−Zn (2a) and H_2−xB−H_2 (2b), Model Monomer (3), and Real Monomers ZnP (4a) and H_2P (4b). Reproduced from reference 11 with permission.

Table 2. Lifetimes of the ZnP Moiety (τ_{ZnP}), rate constants of Triplet Energy Transfer (k_{TEET}), and Transfer Efficiencies (E_{TEET}) of the Studied Compounds in 2-MTHF at 150 K. Adapted from reference 11.

Sample	τ_{ZnP} (s)	k_{TEET} (s^{-1})	E_{TEET} (%)
ZnP	2.9×10^{-3}	14.2	
Zn-5B	2.9×10^{-3}	13.4	
Zn-2B-H_2P	54×10^{-9}	2.0×10^{7}	99.99
Zn-3B-H_2P	1.4×10^{-6}	7.2×10^{5}	99.95
Zn-4B-H_2P	41×10^{-6}	2.4×10^{4}	98.59
Zn-5B-H_2P	0.55×10^{-3}	1.5×10^{3}	80.97

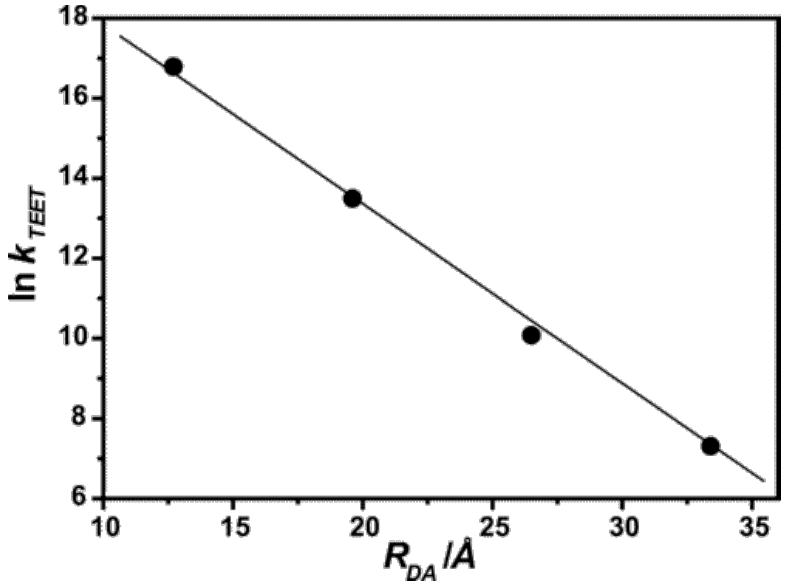

Figure 5. The logarithm of the experimentally determined triplet energy transfer rate, k_{TEET}, in the ZnP−xB−H_2P series of compounds and a linear fit to the data plotted against the donor−acceptor edge-to-edge distance, R_{DA}. Reproduced from reference 11 with permission.

To demonstrate orientation dependence of energy transfer in covalently-linked chromophoric assemblies, Maiya and co-workers chose a porphyrin-based Donor-Acceptor (D-A) system where the donor and the acceptor components are positioned at two distinctly different orientations. The D-A system **3** consists of donor anthracene moieties that are linked both at the "axial" and "peripheral" sites of a tin(IV) porphyrin scaffold (Figure 6).[13] Two "reference" compounds **1** (where the anthracene moiety occupies only the peripheral position) and **2** (where the anthracene moieties occupy only the axial sites) were also synthesized. The fluorescence quantum yields of **1, 2,** and **3** were measured after excitation at 250nm (absorption maximum of anthracene). The quantum yields of **3** (Φ = 0.21±0.01) and **1** (Φ < 0.001) were quenched in comparison to the anthracene moiety (Φ = 0.32±0.02). Interestingly, under similar experimental conditions, fluorescence originating from the anthracene subunits of **2** remained largely unaltered (Φ = 0.29±0.02).

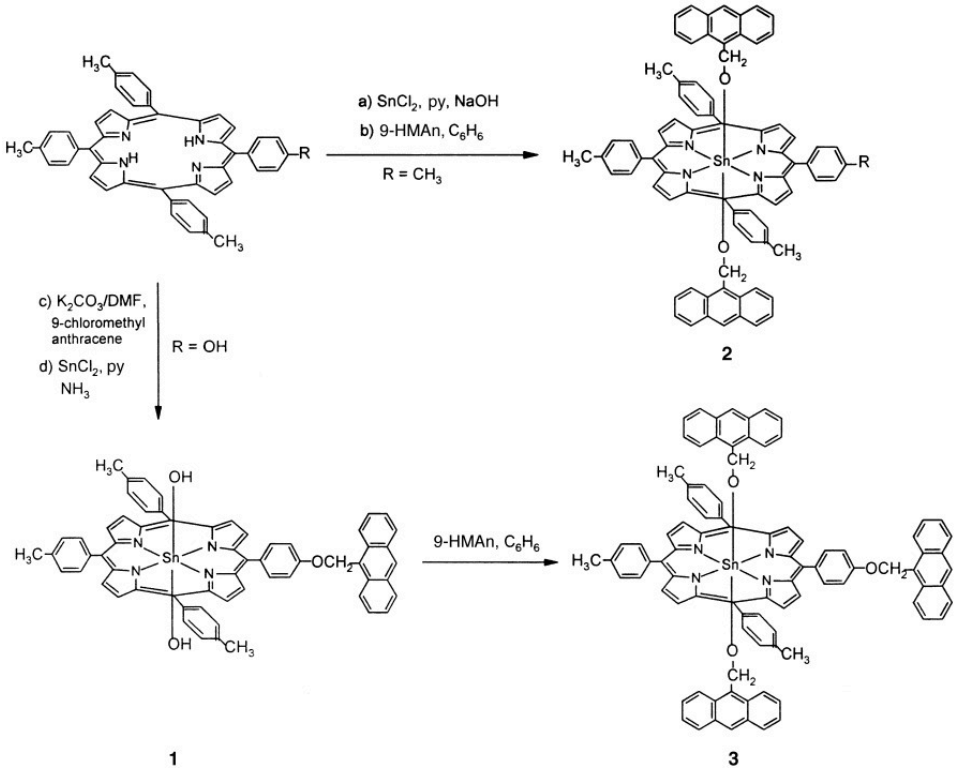

Figure 6. Synthesis of D-A systems studied by Maiya and co-workers (**1**, **2**, **3**); py = pyridine. Reproduced from reference 13 with permission.

Fluorescence lifetimes of the anthracene moieties (λ_{ex}=250 nm, λ_{em}=400 nm) in the D–A systems were: 0.16 ns (~100 %) for **1**; 2.14 ns (100 %) for **2**; and 0.62 ns (31 %) and 2.28 ns (69 %) for **3**. The relative amplitudes obtained while fitting the lifetime data to single/bi-exponential decay functions are provided in the parenthesis. Based on the lifetimes of **1** and **2**, the biexponential fluorescence decay observed for **3** can be interpreted in terms of the presence of two different ground-state D–A orientations (unquenched axial and quenched peripheral) in this system. Excitation of both **3** and **1** at 250 nm resulted in the appearance of the characteristic porphyrin emission bands in the 600–700 nm region; which was not the case for **2**. In addition, overlap of the excitation spectra (emission collected at the porphyrin emission maximum, 665 nm) with the corresponding absorption spectra revealed that fluorescence quenching in **1** and **3** is entirely a result of the energy transfer in these two D–A systems (Figure 7). The energy transfer efficiencies

(%E) for **1, 2,** and **3** were found to be 99 ± 7, 25 ± 3, and 5 ± 2 respectively. Thus, energy transfer is very inefficient in **2** (where the donor subunits are exclusively at the axial positions), almost quantitative in **1** (where the donor subunit is exclusively at the peripheral site), and is approximately 30 % in **3** (where the two donor subunits are at the axial site and one at the peripheral position). Clearly, energy transfer to the porphyrin is strongly favored (~100 %) from the peripheral anthracene and is quite inefficient (~0 %) from the axial anthracene in these D–A systems. It should be noted that the peripheral anthracene subunit of **3** absorbs only one third of the incident light at the excitation wavelength. Thus, a near 30 % quenching observed for this system amounts, effectively, to %E of ~100 from the peripheral anthracene to the porphyrin.

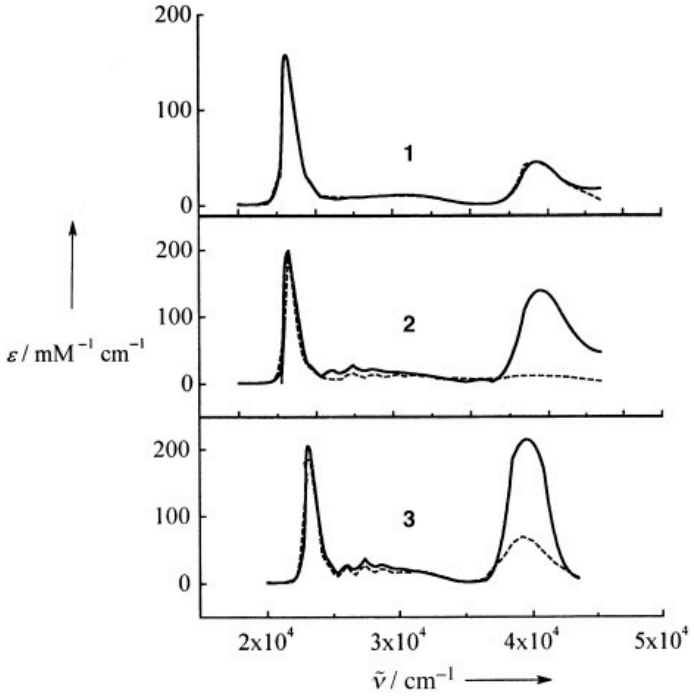

Figure 7. Overlay of the excitation (dashed line) and absorption (solid line) spectra of 1-3 in CH_2Cl_2 (λ_{em}=665 nm). Reproduced from reference 13 with permission.

Having demonstrated the orientation dependence of energy transfer in these D–A systems, the authors explored the origin of this novel effect. The orientation factor (κ^2) is given by eq. 5 (see Section 1.2.3 of this chapter). In eq. 5, α and β are the angles made by the transition dipoles of

anthracene (axial/peripheral) and porphyrin with the line joining their centers, and γ is the angle between the two transition dipoles. While the transition dipole of the emitting S_1 state (first excited state) of anthracene lies on the short axis of the molecule, that of porphyrin lies along a line joining the two opposing pyrrole nitrogens. Thus, the donor and acceptor transition dipoles when the anthracenes occupy the axial sites are nearly perpendicular ($\kappa^2 \approx 0$) and are nearly coplanar ($1 < \kappa^2 < 4$) when the anthracene is linked at the peripheral site. Thus, the energy transfer behavior of compound **3** is dictated by the orientations of anthracene donors relative to the porphyrin acceptor.

1.5 Energy Transfer in Pyrene- and Porphyrin-based Dendrimers

Dendrimers consisting of molecular units repeatedly branching out from a central core designed to act as an excitation trap have received significant attention recently.[14–20] Successive branching of terminal groups leads to a series of structures, each with an increased number of peripheral antenna chromophores. By judicious choice of central core and terminal groups, and by tuning the structural parameters of dendrimers, an energy gradient can be established that facilitates funneling of excitation energy from terminal groups to the central core. Frechet-type dendrimers constructed using pyrene (terminal groups) and porphyrin (central core) derivatives are classic examples of this type of arrangement.[14]

Pyrene as a chromophore has outstanding optical properties, like high quantum yield, long fluorescence lifetime, and excimer emission.[21] Pyrene has also been also incorporated into various macromolecules with the aim of developing novel photoactive materials. Given that there is substantial overlap between the emission spectrum of the pyrene and the Soret absorption band of porphyrins, we can expect a very efficient FRET process in structures labelled with these two chromophores.[21] Keeping this in mind, Rivera and co-workers synthesized a series of constructs containing a porphyrin core connected to a first generation Fréchet-type dendron (Py_2G_1).[22] A

second series of constructs consisting of a porphyrin core connected to a second generation dendron (Py_4G_2) was also prepared (Figure 8). FRET occurred efficiently within the dendrimers as determined from the extremely weak fluorescence of pyrene. The number of pyrene groups present in the constructs was varied from two to eight, but was found to have little effect on the rate and efficiency of FRET. The parameter that was found to affect FRET the most was the distance separating pyrene from porphyrin within the constructs. This effect was probed successfully by fitting the pyrene and porphyrin fluorescence decays according to the model free analysis (MFA), which yielded the average rate constant k_{EET} for FRET.[16] k_{EET} increased continuously as the distance between the porphyrin and pyrene moieties was decreased (Table 3).

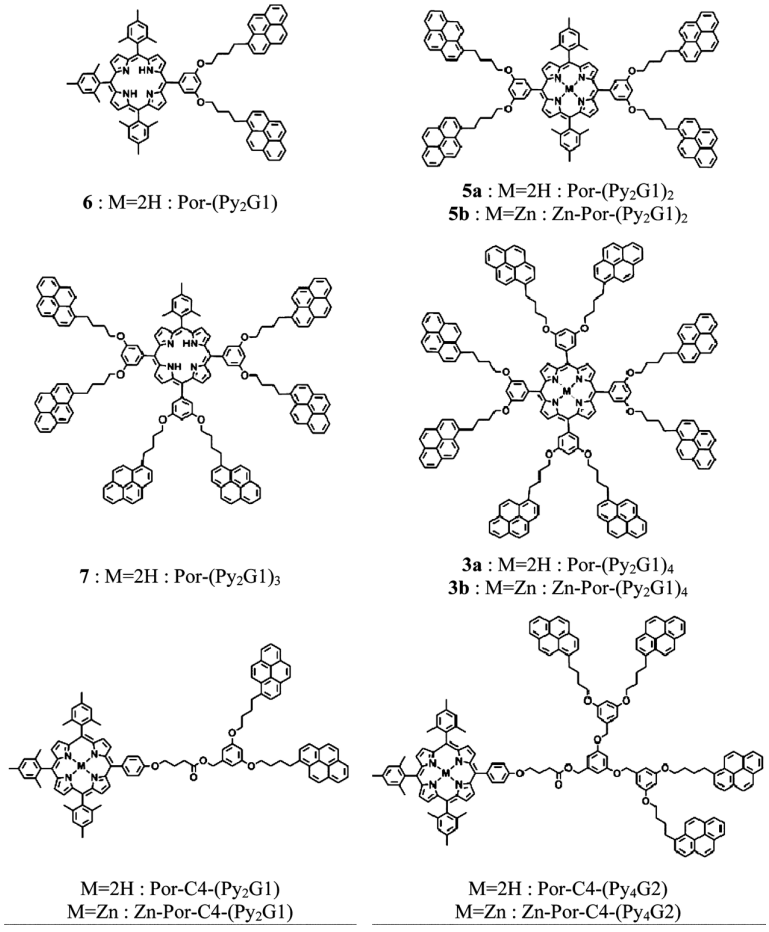

Figure 8. Dendrimer structures studied by Rivera and co-workers. Reproduced from reference 22 with permission.

Table 3. Average Rate Constants (k_{EET}) and separation distances between porphyrin and pyrene ($d_{Por–Py}$) in the dendritic constructs. Adapted from reference 22.

Sample	k_{EET} ($\times 10^9$ s^{-1})	d_{Por-Py} (Å)
Por-$(Py_2G1)_4$	12.2	14.2
Por-$(Py_2G1)_3$	17.2	13.4
Por-$(Py_2G1)_2$	17.7	13.4
Por-$(Py_2G1)_1$	10.6	14.6
Por-C_4-(Py_2G1)	2.2	18.9
Por-C_4-(Py_4G2)	1.9	19.4

1.6 Energy Transfer in Conjugated Polymer-based Systems

The chemical composition and structural order in thin films of conjugated polymers significantly influence the performance of polymer-based optoelectronic devices that involve excitation energy transfer.[23–25] An understanding of the dependence of EET on the relative internal geometries of donor and acceptor species is therefore important. Haugland and co-workers reported an experimental study of the dependence of energy transfer on donor-acceptor distance.[26] Oligomers of poly-L-proline were used as spacers of defined length to separate an energy donor and acceptor by distances ranging from 12 to 46 Å (Figure 9). The energy donor was an α-naphthyl group at the carboxyl end of the polypeptide, while the energy acceptor was a dansyl group at the imino end. The efficiency of energy transfer was determined from the excitation spectrum of the energy acceptor (Figure 10a). At a given wavelength, the intensity of the excitation spectrum of acceptor (I) is related to the transfer efficiency (E), the extinction coefficient of the donor (ε_D), and the extinction coefficient of acceptor (ε_A), by the expression $I = \varepsilon_A + E\varepsilon_D$. The intensity of the

excitation peak at 295 mμ provided the most sensitive index of the efficiency of energy transfer. The transfer efficiency was found to decrease from 100 percent at a distance of 12 Å to 16 percent at 46 Å (Figure 10b). Energy transfer was 50 percent efficient at 34.6 Å. The dependence of the transfer efficiency on distance was in excellent agreement with the R^{-6} dependence predicted by the Förster mechanism for weak dipole-dipole coupling.

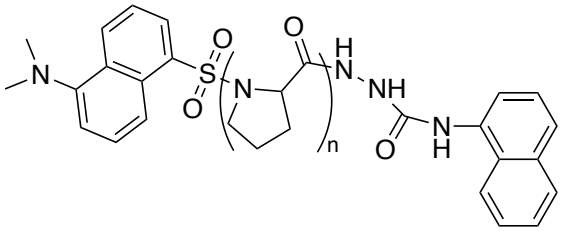

Figure 9. Structure of oligomers of poly-L-proline (n = 1 to 12). Adapted from reference 26.

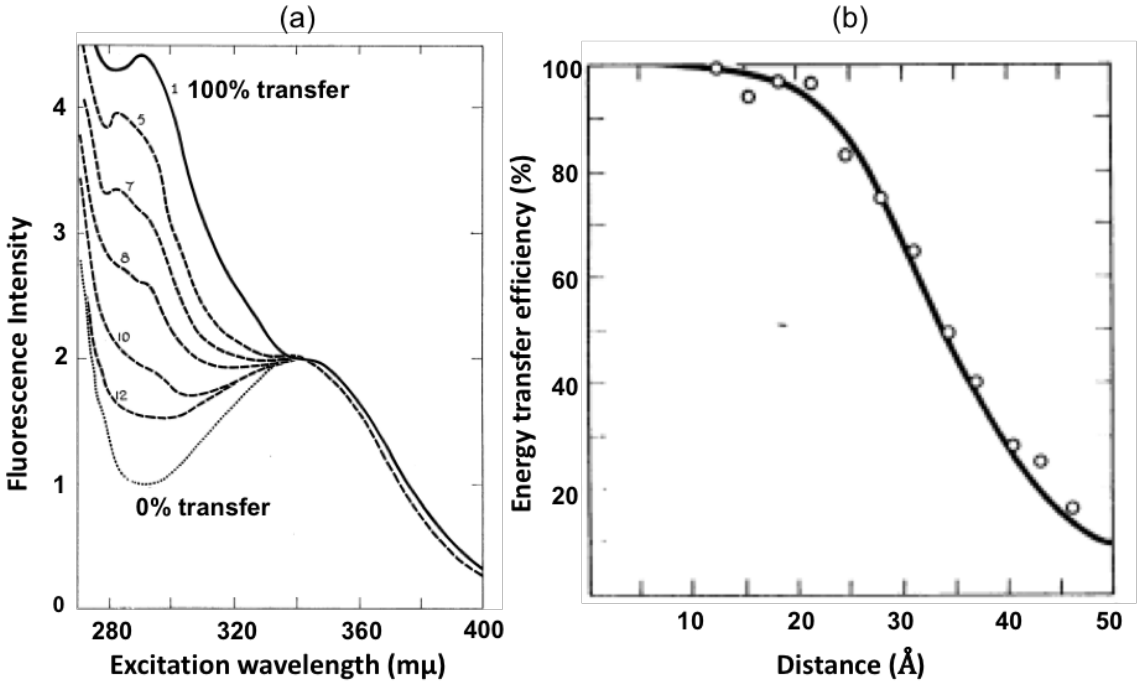

Figure 10. (a) Excitation spectrum of dansyl-L-prolyl-hydrazide (0% transfer), dansyl-L-prolyl-α-naphthyl (100% transfer), and dansyl-$(L\text{-prolyl})_n$-α-naphthyl (n = 5, 7, 8, 10, 12) in ethanol. Adapted from reference 26.

In order to develop artificial systems that are as efficient as photosynthetic antennas, it is necessary to devise strategies that afford control over the direction of energy transfer. To attain this objective, Schwartz and co-workers designed a composite material consisting of semiconducting polymer chromophores that have been aligned on the nanometer scale and encapsulated into the hexagonally arrayed pores of mesoporous silica glass. The semiconducting polymer poly[2-methoxy-5-(2'-ethyl-hexyloxy)-1,4-phenylene vinylene] (MEH- PPV) was chosen as the chromophore.[25] The design of the system forces energy to flow unidirectionally from aggregated, randomly oriented polymer segments outside the pores to isolated, aligned polymer chains within the pores. The driving force for this energy flow arises solely from changes in polymer conformation: the aggregated polymer segments outside the silica framework have a higher excited state energy than the aligned polymer segments encapsulated within the pores, which gives rise to an energy cascade. Thus, nanometer-scale positional control achieved through host-guest chemistry and the sensitive optical properties of semiconducting polymers can be combined to control energy flow. Time-resolved and steady-state emission studies on conjugated polymers established that the dominant interchain energy transfer (energy transfer between the randomly oriented chains outside the pores) mechanism is Förster resonance energy transfer. Since the interchain migration rate depends on the relative internal geometries of the donor and acceptor chromophores, an understanding of distance and orientation dependence of energy transfer is important for achieving directional energy transfer in polymer-based opto-electronic devices.

1.7 Ligand-to-Ligand Energy transfer in Metal-Organic Frameworks

Photoactive metal-organic frameworks (MOFs) composed of metal centers or metal oxide clusters connected through organic ligands have recently emerged as a new class of materials that can be used for fabricating artificial light harvesting devices.[27–32] Compared to other artificial light

harvesting assemblies discussed in this chapter, MOFs demonstrate a higher degree of structural flexibility that affords an opportunity to coordinatively attach different types of chromophores as linkers. The modular nature of MOFs enables control over their topologies, porosities, functionalities, and surface properties.[33] Furthermore, the crystalline nature of MOFs allows for precise control of distances and orientations between chromophores by judicious choice of ligands and metal nodes.[6] MOFs, thus, provide a unique platform for systematically studying energy transfer as a function of their 3D structure. The extended solid-state structure of MOFs also offers the possibility of achieving sequential, long-distance energy transfer over several hundred angstroms.[2,6,27,34–40] Lastly, the high stability and processability of MOFs means that they are feasible for practical applications, and can compete with the current generation of dendritic and polymer-based light harvesting systems. All these qualities make MOFs excellent candidates for studying light harvesting and energy transfer processes. In the last few years, there have been numerous reports of MOFs with ligand-based luminescence (e.g., porphyrin- and ruthenium-based MOFs) demonstrating efficient ligand-to-ligand energy transfer.[1,2,6,27,36,38,41–45] The following subsections will focus on light harvesting and energy transfer processes observed in MOF-based systems.

1.7.1 Energy transfer in porphyrin-based MOFs

In natural photosynthesis, energy transfer primarily occurs in highly ordered porphyrin-based pigments (chlorophylls). Drawing inspiration from nature, Hupp and co-workers designed two Zn-porphyrin-based MOFs (DA-MOF and F-MOF) (Figure 11).[39] Energy migration was studied with the help of fluorescence quenching experiments. The excitation energy was found to migrate over a net distance of ~3 porphyrin struts for F-MOF and ~45 porphyrin struts for DA-MOF. The authors inferred that the two additional acetylene groups in the DA-H_2P ligand enhance its π-

conjugation, resulting in a red-shifted Q-band (absorption band in the 500-650 nm range, Figure 12). Consequently, DA-MOF exhibits a larger spectral overlap as compared to F-MOF. The larger spectral overlap facilitates rapid energy transfer between adjacent DA-H_2P ligand, resulting in efficient, long-distance energy transport.

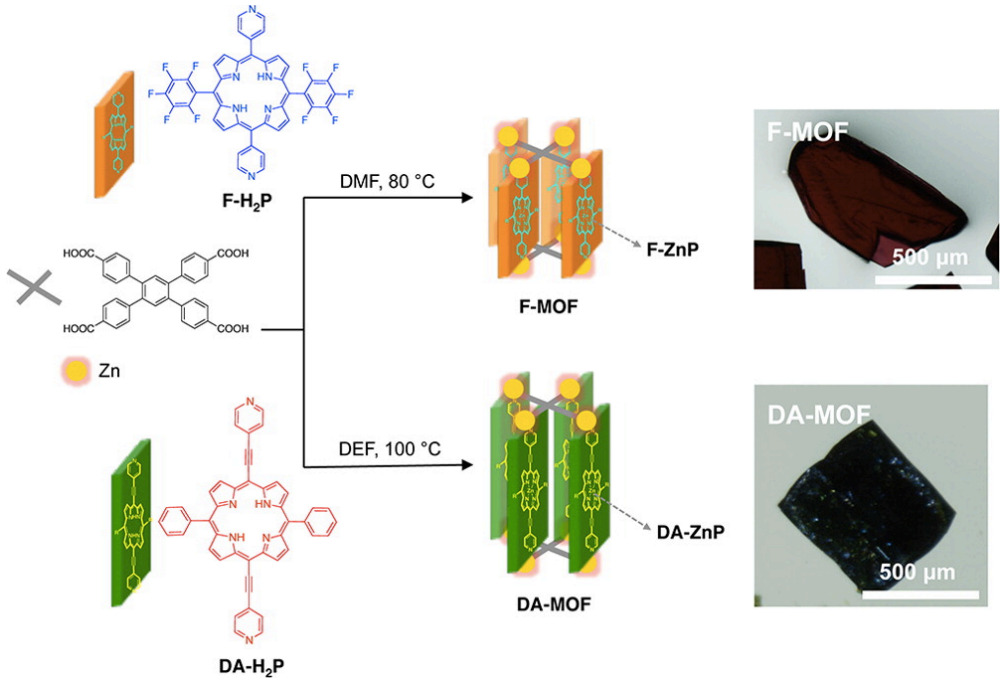

Figure 11. Synthesis of DA-MOF and F-MOF. Reproduced from reference 39 with permission.

The authors investigated energy migration by incorporating quenching moieties (pyridyl-ferrocene, FcPy) directly inside the MOF structures. It was proposed that upon excitation at 446 nm, the MOFs generate an exciton that migrates by ligand-to-ligand hopping within the MOF structure until it decays (via fluorescence) or is quenched by FcPy. The efficiency of energy migration was evaluated by measuring the extent of fluorescence quenching with different levels of FcPy incorporation (Figure 13). At similar loadings of Fc-Py, DA-MOF demonstrated substantially greater quenching than F-MOF. DA-MOF provided the first example of long range, directional energy transport in MOFs, and offered useful information for the design of efficient light-harvesting and energy-transfer materials.

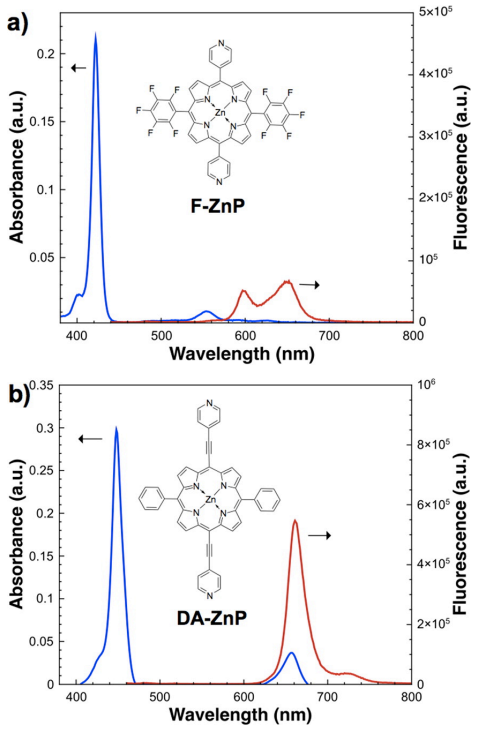

Figure 12. UV-Vis absorption (blue) and emission spectra (red) of (a) F-ZnP and (b) DA-ZnP measured in DMF. Reproduced from reference 39 with permission.

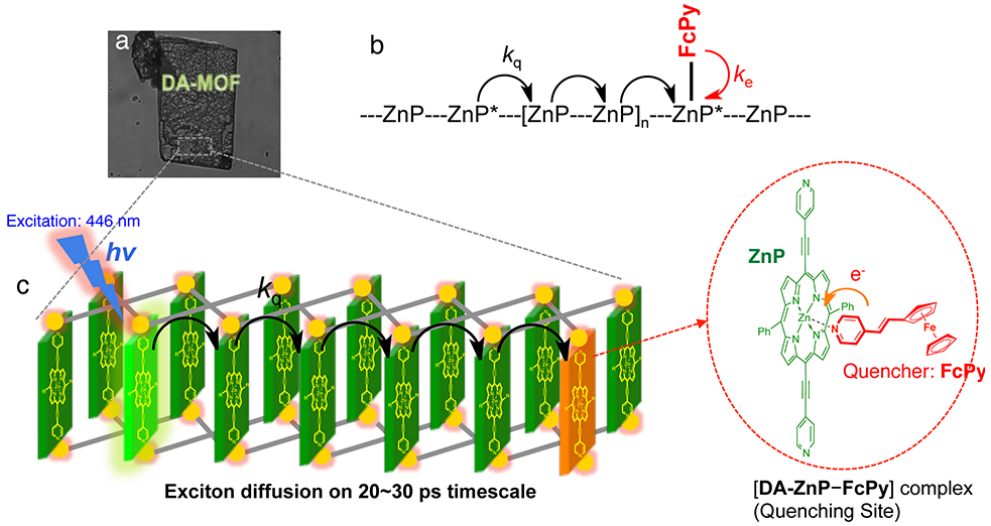

Figure 13. (a) Photograph of a DA-MOF particle from which fluorescence is recorded based on laser excitation at 446 nm. Luminescence quenching measurements are conducted to probe the energy (exciton) migration dynamics. (b,c) Schematic representation of the exciton migration and quenching processes. Reproduced from reference 39 with permission.

Bodipy (boron dipyrromethene) is a well-known molecular chromophore with several favorable properties, such as high emission quantum yield, low intersystem crossing rate, large extinction coefficient, long excited-state lifetime, and good photostability. Owing to the large overlap between the emission spectrum of Bodipy and the absorption spectrum of porphyrin, the co-assembly of these two ligands in a MOF should enable facile energy transfer. Taking this into consideration, Hupp and co-workers synthesized a pillared-paddlewheel type BOP MOF having bodipy- and porphyrin-based struts.[37] Bodipy was incorporated into the framework to serve as the light harvesting antenna chromophore for the excitation of porphyrin struts via resonance energy transfer. Hupp and co-workers also synthesized BOB MOF, a control material based on bodipy and a non-chromophoric dibrominated strut. The synthetic scheme for BOP MOF and BOB MOF is presented in Figure 14.

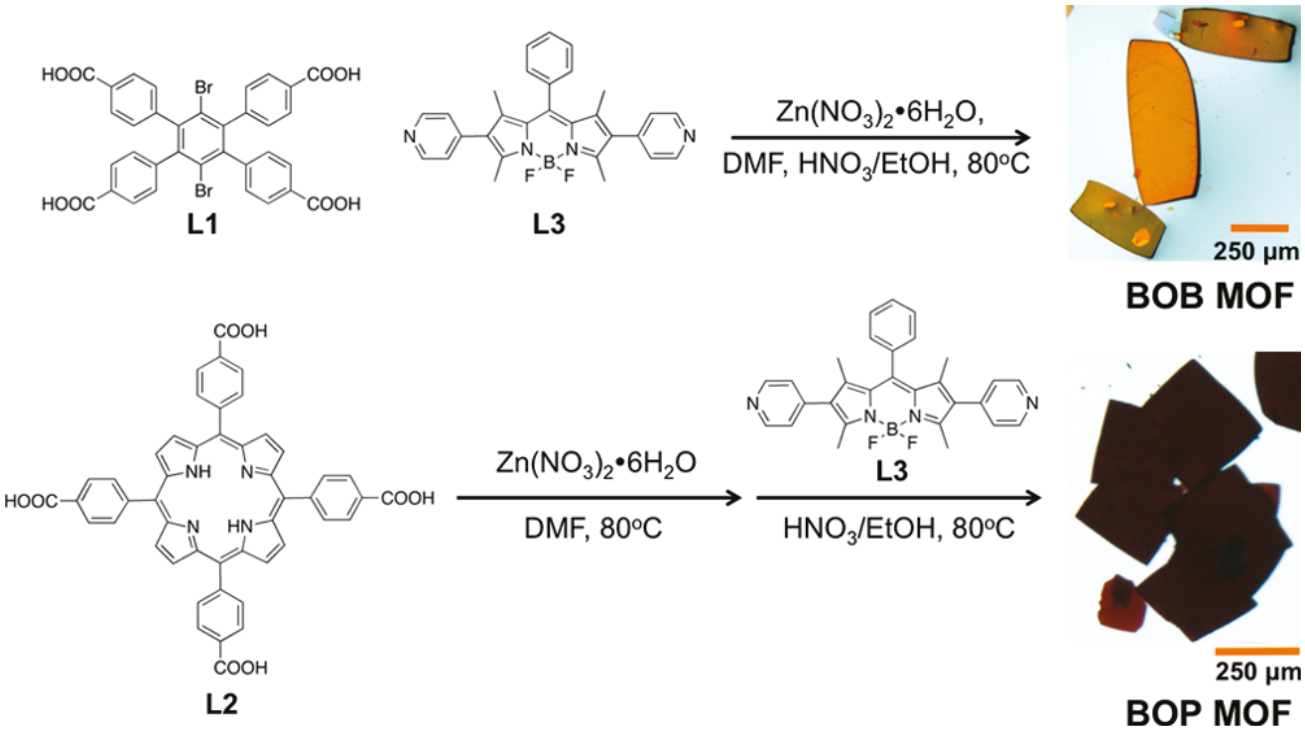

Figure 14. Synthesis of BOP and BOB MOFs. Reproduced from reference 37 with permission.

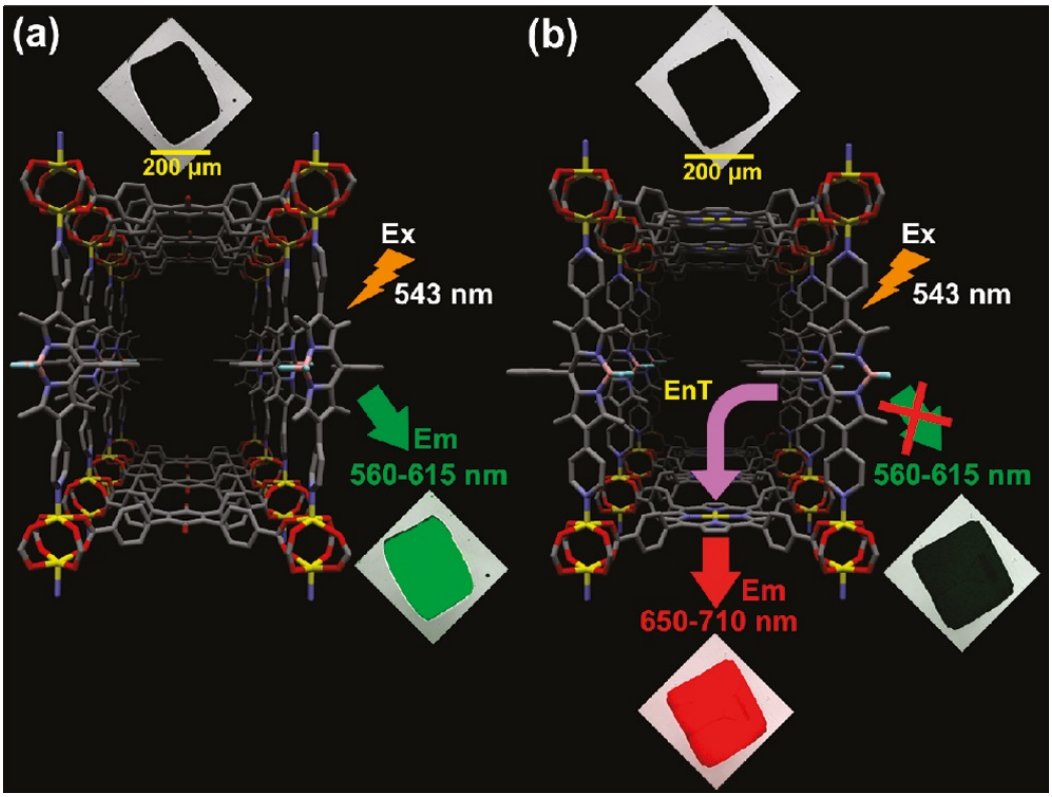

Figure 15. Confocal laser scanning microscopy images of (**a**) BOB MOF and (**b**) BOP MOF. Reproduced from reference 37 with permission.

The light harvesting properties of BOB MOF and BOP MOF were investigated with the help of confocal laser scanning microscopy (CLSM). Excitation of bodipy linkers in BOB MOF (control material) at 543 nm resulted in typical bodipy fluorescence behavior with the emission maxima at 596 nm (Figure 15). On the contrary, excitation of bodipy linkers in BOP MOF resulted in emission in the 650-710 nm range. Given that porphyrins emit in the 650-710 nm range, this result confirms the presence of energy transfer from bodipy strut to porphyrin strut. Through their investigations on DA-MOF, F-MOF, BOB MOF, and BOP MOF, Hupp and co-workers successfully highlighted the importance of spectral overlap in MOF-based energy transfer processes.

Revisiting the bioinspired nature of porphyrin-based light harvesters, Shustova and co-workers explored the possibility of using a MOF to mimic the highly efficient energy transfer process observed between green fluorescent proteins and heme-binding cytochromes.[46] Two approaches were explored to construct the MOF-mimic (1) direct incorporation of the donor and acceptor species in the backbone of a 3D MOF and (2) the encapsulation of donor species in the pores of a MOF built using acceptor species. In approach 1, methyl-2-(4-(2,5-di(pyridin-4-yl)benzylidene)-2-methyl-5-oxo-4,5-dihydro-1H-imidazol-1-yl)acetate (DPB-BI, donor) and tetrakis(4-carboxyphenyl)-porphyrin (TCPP, acceptor) were incorporated in the backbone of two MOFs. Molecular formulae of the two MOFs are: $Zn_2(ZnTCPP)(DPB\text{-}BI)_{0.86}(DMF)_{1.14}]\cdot(DMF)_{8.86}(H_2O)_{20}$ **(1)** and $[Zn_2(ZnTCPP)(DPB\text{-}BI)_{0.64}\ (DMF)_{0.36}]\cdot(DMF)_{6.94}(H_2O)_{12.55}$ **(1')**. Approach 2 was implemented by encapsulating 4-hydroxybenzylideneimidazolinone (donor) in the pores of a porphyrin-based MOF (**2**). The resulting host-guest system was termed as **BI@2** by the authors. Time resolved photoluminescence measurements confirmed the presence of efficient ligand-to-ligand energy transfer in **(1)**, **(1′)**, and **BI@2**. The photophysical and energy transfer parameters of **(1)**, **(1′)**, and **BI@2** are summarized in Figure 16. **BI@2** demonstrated the highest energy transfer efficiencies among the three structures (72%). Considering the dimensions of the 1D channels in **2** and the size of the incorporated BI molecules, the estimated guest–host distances in **BI@2** should be smaller than the donor-acceptor distances in **(1)** and **(1′)**. This explains the enhanced energy transfer performance in **BI@2**. The differences between the photophysical behaviors of **(1)** and **(1′)** were attributed to the fact that **(1)** and **(1′)** have different topologies (Figure 16). The difference in stacking of 2D layers causes the donor-acceptor distances in **(1)** and **(1′)** to be slightly different, which results in different photophysical behavior. The findings of this

investigation clearly show that the energy transfer properties of MOFs are strongly sensitive to the donor-acceptor distances.

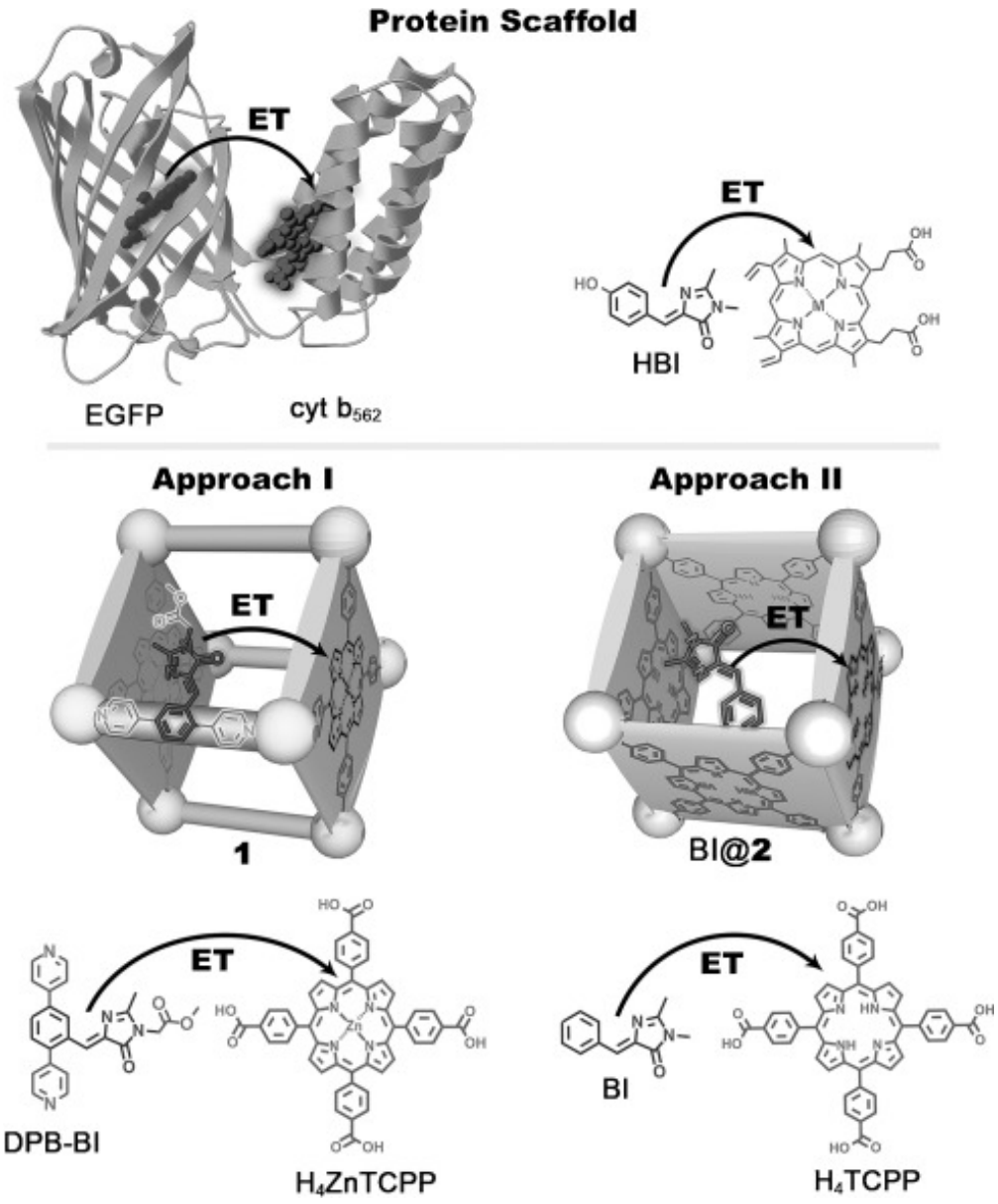

Figure 16. (Top) Depiction of ET between EGFP and the electron transfer protein, cytb562. (Bottom) Approach I focused on coordinative immobilization of two chromophores in crystalline scaffold 1 and 1'. Approach II is based on inclusion of the BI donor in the porphyrin-based framework 2. Reproduced from reference 46 with permission.

	DPB-BI	DPB-BI-**1**	DPB-BI-**1′**	BI	BI@**2**
$\langle\tau_{av}\rangle$ [ns][a]	1.09	0.38	0.51	1.89	0.53
k_{ET} [$\times 10^{10}$ s^{-1}]	–	1.71	1.04	–	1.36
R_o [Å]	–	23	23	–	21
Φ_{ET} [%]	–	65	53	–	72
J [$\times 10^{-14}$ cm^3 M^{-1}]	–	6.25	6.25	–	4.57

Figure 17. The average lifetimes (τ_{av}), energy transfer rate constants (k_{ET}), Föster distance (R_0), energy transfer efficiency (Φ_{ET}), and spectral overlap integrals (J) for **(1)**, **(1')**, and **BI@2** samples. Reproduced from reference 46 with permission.

1.7.2 Porphyrin based MOFs materials as thin films

After achieving considerable success in mimicking the natural process of light harvesting by using porphyrin-based MOFs, the next big challenge is to find a way of integrating these MOFs into solar energy conversion devices. Fabricating MOFs in thin-film form (on suitable substrates) is a promising approach to address this issue.[47–51] In order to make MOF thin films feasible for practical applications, research efforts need to be directed towards,

1. Developing synthetic strategies that afford precise control over the thickness of films
2. Identifying MOFs that demonstrate directional, efficient energy transfer
3. Ensuring that the energy migration distance is equal or greater than the MOF film thickness, in order to move the excitation energy towards either an underlying electrode or external redox phase.

Hupp and co-workers converted a pillared paddlewheel porphyrin-containing 3D MOF thin film to a 2D framework by solvent-assisted linker exchange (SALE).[52] As shown in Figure 18, the pillar ligand 4,4'-bipyridine was replaced by pyridine (non-bridging ligand), leading to the collapse of the 3D MOF structure into a layered 2D coordination polymer. The inter-layer distance between

the chromophores significantly decreased due to the structural change. Pd-TCPP (P2) was used as an efficient, nonfluorescent energy acceptor (quencher) by depositing it on the surface of the films. Steady-state and time-resolved emission spectroscopy indicated that in 2D films, excitons can travel up to 11 porphyrin layers. On the other hand, in 3D films excitons can propagate only up to 8 porphyrin layers. Considering the effective elimination of void space between porphyrin layers by SALE, the improved energy transfer performance in 2D films was attributed to the decrease in donor-acceptor separation distance.

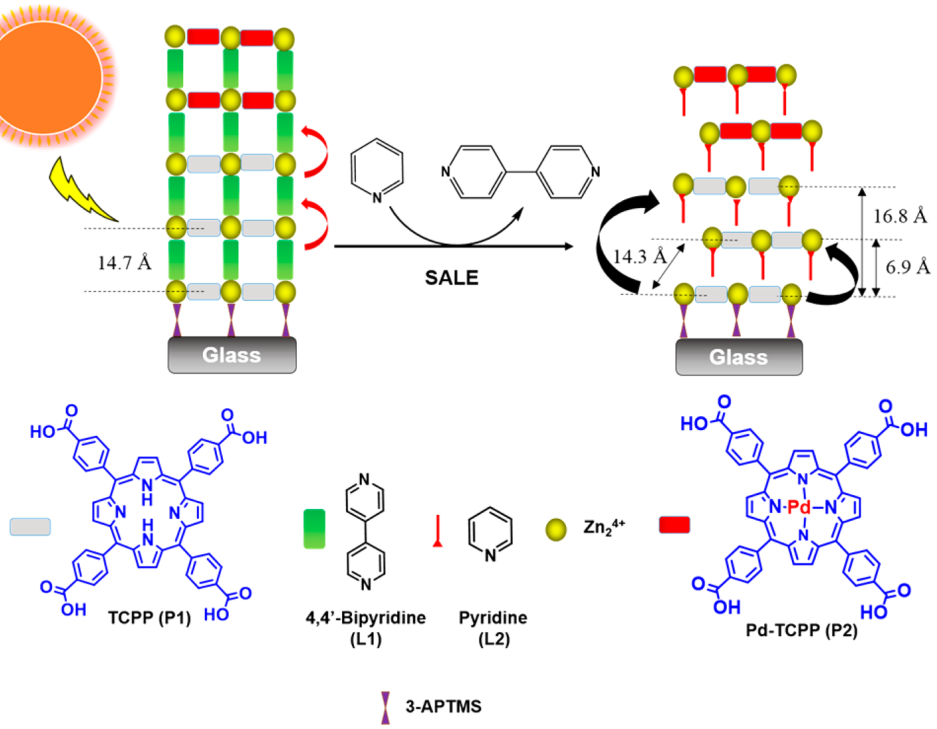

Figure 18. Free-base porphyrin P1 and linker L1 were used to fabricate N (number of cycles) cycles of MOF thin films followed by N + 1 and N + 2 cycles by palladium porphyrin P2 and linker L1. Reproduced from reference 52 with permission.

1.7.3 Energy transfer in Ru/Os based MOF

Use of coordination complexes such as $Ru(bpy)_3^{2+}$ and $Os(bpy)_3^{2+}$ (bpy = bipyridine) as building blocks for metal-organic frameworks has gained popularity in the last few years. Due to their long-lived excited states and high redox activity, these photoactive compounds have been of

particular interest for applications in light harvesting and energy transfer.[27,36,43,53–55] These complexes absorb strongly in the visible region to form a singlet metal-to-ligand charge transfer excited state (^{1}MLCT).[56] This is followed by an efficient intersystem crossing to the triplet state (^{3}MLCT) due to the large spin-orbit coupling of the Ru(II) and Os(II) centers (heavy atom effect). The long-lived ^{3}MLCT excited can either deactivate via phosphorescence or participate in triplet-triplet energy transfer events. Energy flow from MLCT excited states of $Ru(bpy)_3^{2+}$ to $Os(bpy)_3^{2+}$ has been explored in various systems like polymers, supramolecular assemblies, ligand-bridged complexes, crystalline molecular solids, and semiconductor interfaces.[57–60]

Lin, Meyer and coworkers were the first to study the classic $Ru(bpy)_3^{2+}$-to- $Os(bpy)_3^{2+}$ energy transfer process in MOFs.[36] They used derivatives of $Ru(bpy)_3^{2+}$/$Os(bpy)_3^{2+}$ as the linkers and Zn clusters as metal centers to construct a 2-dimensional framework. Figure 19 shows the synthesis scheme for phosphorescent **MOF-1,** based on the photoactive Ru(II)(bpy)(4,4'-dcbpy)$_2$ ($L_{\mathbf{1\text{-}Ru}}$) ligand, where 4,4'-dcbpy = 2,2'-bipyridine-4,4'-dicarboxylic acid). $L_{\mathbf{1\text{-}Ru}}$ absorbs strongly in the visible region and can serve as the light harvesting antenna chromophore. Os(II) (bpy)(4,4'-dcbpy)$_2$ ($L_{\mathbf{1\text{-}Os}}$) was doped into the framework structure to produce mixed-metal MOF-1 samples with 0.3, 0.6, 1.4 and 2.6 mol % Os loading.

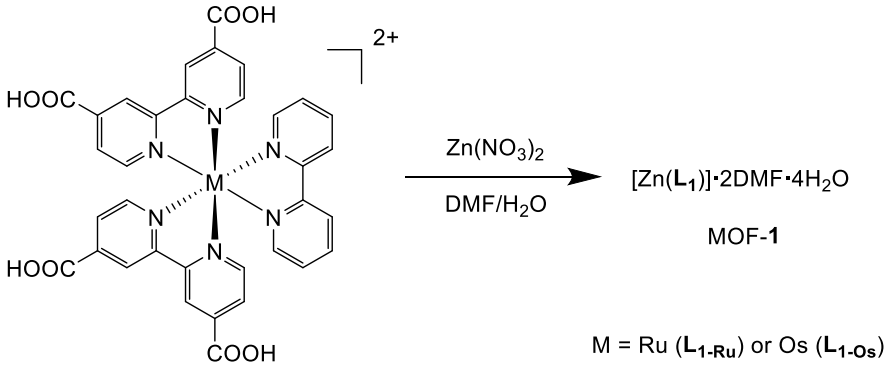

Figure 19. Synthesis procedure of MOF-1. Reproduced from reference 36 with permission.

Time-resolved emission measurements performed with a two-photon excitation at 850 nm revealed the presence of long-range energy migration in the mixed-metal MOFs. The excited state lifetime of $L_{1\text{-}Ru}$ linkers was found to decrease progressively as the doping concentration of $L_{1\text{-}Os}$ linkers increased from 0.3 to 2.6 mol %. The authors proposed that sensitization of $L_{1\text{-}Os}$ occurs via $Ru(bpy)_3^{2+}$-to- $Ru(bpy)_3^{2+}$ energy hopping events followed by $Ru(bpy)_3^{2+}$-to- $Os(bpy)_3^{2+}$ energy cascade (Figure 20). Due to the lower energy of its ^{3}MLCT state, $L_{1\text{-}Os}$ acts as a trap site and quenches the excitation. Furthermore, based on an analysis of the crystal structure parameters, it was estimated that a $L_{1\text{-}Os}$ trap site should have a quenching radius of ~40 Å.

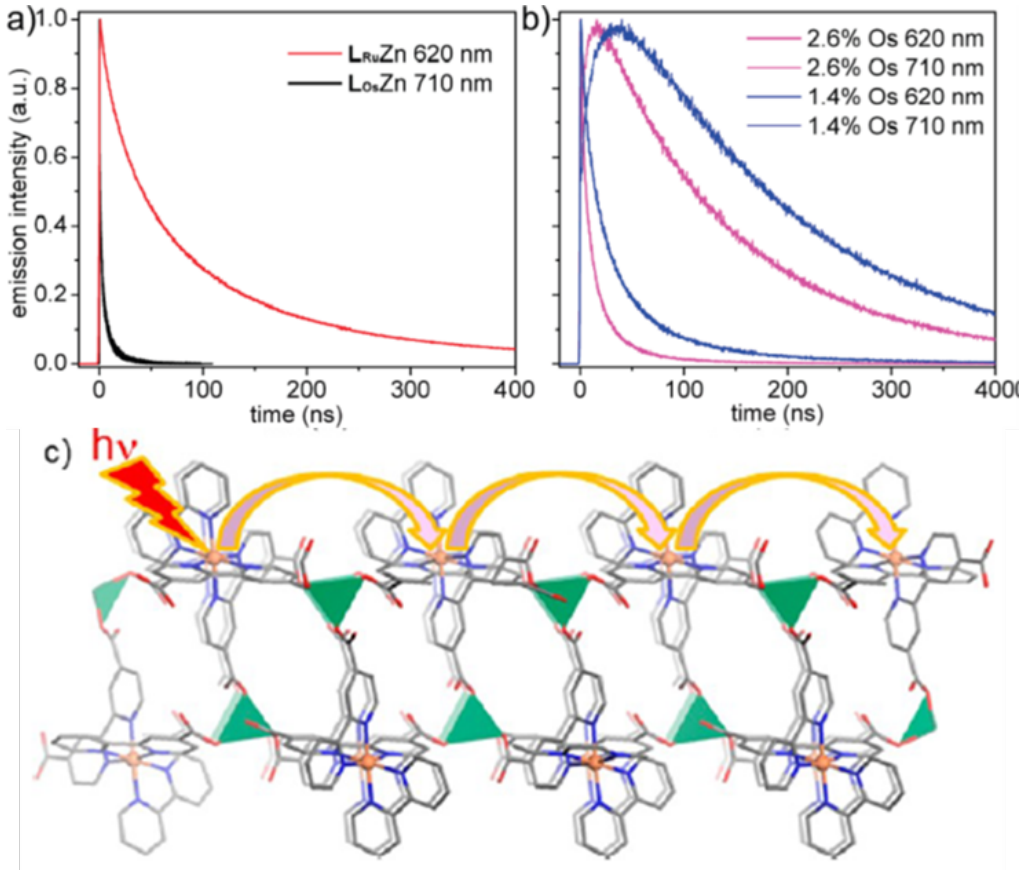

Figure 20. (Top, **a**) Time-resolved emission decay for L_{Ru} and L_{Os} MOF-1 monitored at 620 and 710 nm, following two photon excitation at 850 nm. (Top, **b**) Emission kinetics for 1.4 to 2.6mol% Os doped MOF-1 at 620 nm and 710 nm by Os(II)*. (Bottom) Schematic representation of hopping of Ru(II)*-bpy excited states in MOF-1. Reproduced from reference 36 with permission.

Due to the high porosity and aperture size tunability demonstrated by MOFs, photoactive Ru/Os polypyridyl complexes can also be encapsulated into their pores as guest molecules to probe energy transfer. The Meyer group synthesized a zinc-based MOF with caged $Ru(bpy)_3^{2+}$/$Os(bpy)_3^{2+}$ chromophores, $[M(bpy)_3^{2+}]@[Zn_2(C_2O_4)_3]$ (MOF-**4**).[52] A long-lived ^{3}MLCT excited state with a lifetime of 760 ns was observed in Ru-MOF-**4**, under anaerobic conditions. In the presence of trace amount of oxygen, the lifetime was significantly shortened to 92 ns due to energy transfer from $Ru(bpy)_3^{2+}$ to O_2 . Similar to MOF-**1**, $Os(bpy)_3^{2+}$ can act as the energy trap sites (at doping levels of 0.2 to 1.0%). Kinetic studies showed that the entrapped chromophores in **MOF-4** provide a network for rapid energy transfer among $Ru(bpy)_3^{2+}$ units, ultimately, finding an $Os(bpy)_3^{2+}$ trap site.

The experimental results for MOF-**1** and MOF-**4** were complemented with a theoretical study of energy transfer in these MOFs.[45] The study revealed that energy transfer in MOF-**1** and MOF-**4** is dominated by the Dexter exchange mechanism. It was also found that energy migration in MOF-**1** is primarily 1-dimensional, whereas in MOF-**4** it occurs through the 3D network. The dominance of Dexter exchange mechanism in MOF-**1** and MOF-**4** indicates energy transfer should be highly sensitive to donor-acceptor distances. One possible approach to improve the efficiency of energy transfer is to enhance the Dexter coupling interactions. This can be achieved by constructing MOFs with shorter intermetallic distances.

1.7.4 Energy transfer in $Ru(bpy)_3^{2+}$ doped zirconium(IV) MOFs

UiO-67 is a water-stable zirconium-based MOF containing 4,4'-biphenyldicarboxylate struts and having a molecular formula of $Zr_6(\mu_3\text{-}O)_4(\mu_3\text{-}OH)_4(BPDC)_6$ (BPDC = biphenyldicarboxylic acid). It comprises of pores with two distinct geometrical environments: an octahedral pore with a diameter of 23Å, and a tetrahedral pore with a diameter of 11.5Å (Figure 21). Lin and coworkers were the first to dope photoactive chromophores, such as $[Ru(dcbpy)(bpy)_2]^{2+}$ (RuDCBPY), in the

UiO-67 framework.[28] The photophysical properties of doped MOFs (RuDCBPY-UiO-67) were studied as a function of RUDCBPY loading within the framework by the Morris group.[43,54] The diffuse reflectance spectrum of RuDCBPY-UiO-67 MOFs showed an absorption band centered at 455 nm, which is ascribed to the transition from the ground state to the singlet metal-to-ligand charge transfer (^{1}MLCT) state. The breadth of this band was found to increase upon increasing the RUDCBPY loading, while the absorption maximum remained the same for all doping concentrations. The excited state lifetimes and emission maxima were observed to be highly sensitive to the concentration of RuDCBPY present within the framework. At relatively low doping concentrations (< 16.4 millimolal), the excited state properties of RuDCBPY in the MOF were quite similar to those observed in DMF. The emission spectrum of RuDCBPY in the MOF was centered at 630 nm, which is slightly red shifted as compared to RUDCBPY solution in DMF (625 nm). The emission decay of RuDCBPY in the MOF was modelled using a single exponential decay function and the excited state lifetime was found to be 1.4 μs. The lifetime of RuDCBPY in MOF is longer than that of RuDCBPY in DMF (890 ns). The increased lifetime in MOF is attributed to the fact that the vibrational decay pathways are impeded when the chromophore is incorporated into a rigid matrix. Notably, as the doping concentrations were increased, a progressive red shift in the emission spectra was observed. Furthermore, biphasic emission decays were observed at high doping concentrations, with a concentration dependent long-lived component ($\tau \sim$165-210 ns) and a concentration independent, short-lived component ($\sim$24 ns).

In order to explain the biphasic nature of the decay at higher doping concentrations, a two-state model was proposed (Figure 22).[54] At low doping concentrations, RuDCBPY preferentially occupies the larger octahedral cages of the MOF by incorporation into the backbone of the cage. Due to the presence of residual reaction solvent (DMF) in the pores, this population of RuDCBPY

is exposed to a DMF-like solvation environment. At higher doping concentrations, in addition to getting incorporated into the backbone of MOF, a small population of RuDCBPY is found to be encapsulated in the some of the octahedral cavities. The authors proposed that encapsulation of RuDCBPY limits the occupancy of DMF in the octahedral cavities, and the μ-O and μ-OH bridges of the zirconium-nodes impose a water-like dielectric on RuDCBPY. As a result, RuDCBPY experiences water-like solvation environment and its photophysical behavior replicates that of RuDCBPY solution in water.

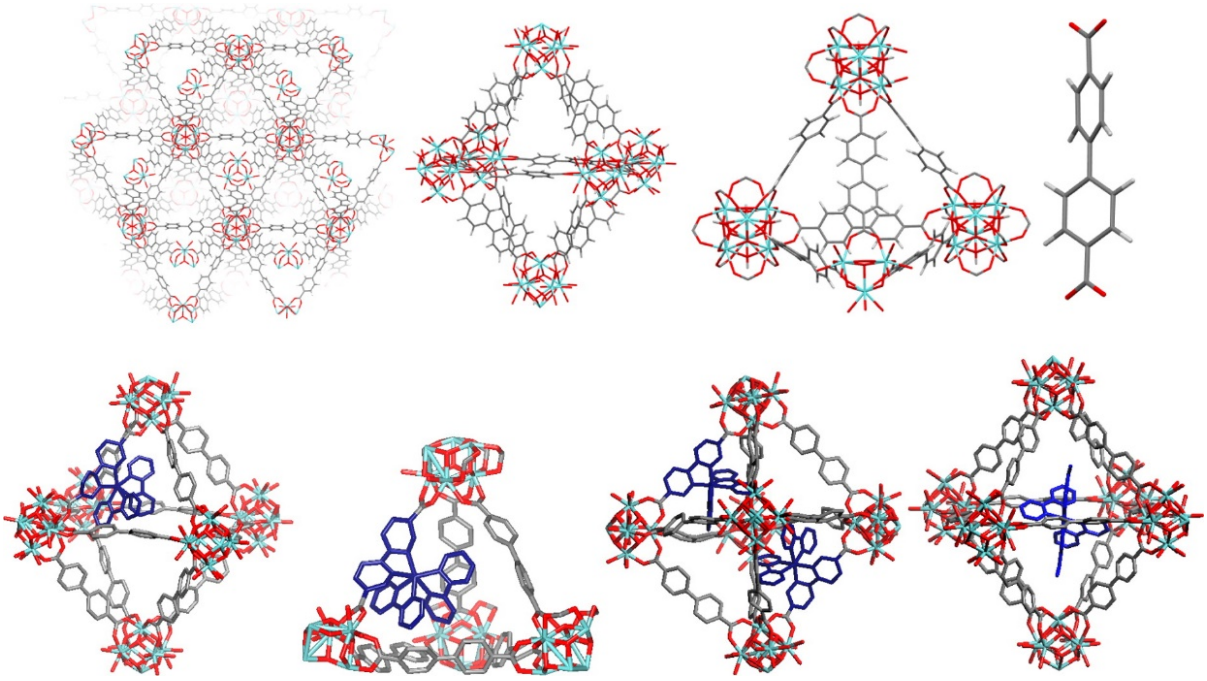

Figure 21. Crystal structure of UiO-67 MOF showing the presence of octahedral and tetrahedral pores with RUDCBPY incorporated as well as encapsulated within the pores. Reproduced from reference 54 with permission.

The concentration dependence of the long-lived component observed in RuDCBPY-doped UiO-67 MOFs is ascribed to ligand-to-ligand energy transfer between RuDCBPY chromophores. To explore the mechanistic aspects of energy transfer in RuDCBPY-doped UiO-67 MOFs, the

emission lifetime data was fit to the Inokuti-Hirayama model. The fitting results indicated $1/r^4$ distance dependence for the energy transfer rate, where r is the interchromophoric distance. Based on the fitting results, a dipole-dipole resonance energy transfer process lying between the Perrin weak coupling and Förster very weak coupling regimes was proposed.

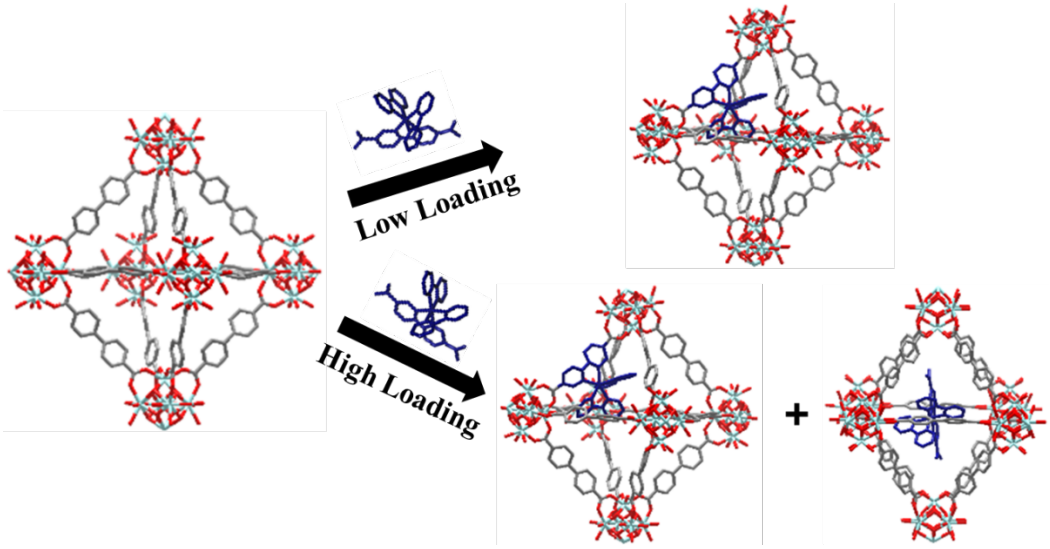

Figure 22. Two-state model showing doping of RuDCBPY within the UiO-67 framework as a function of concentration. Reproduced from reference 54 with permission.

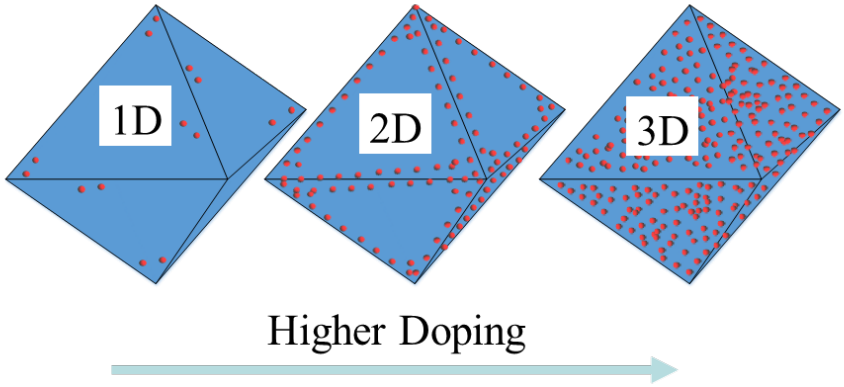

Figure 23. A schematic representation of FRET in RuDCBPY doped UiO-67 as a function of chromophore loading. Reproduced from reference 2 with permission.

In a subsequent study, the dimensionality of energy transfer in RuDCBPY-doped UiO-67 MOFs was also found to be dependent on the doping concentration (Figure 23).[43] Confocal fluorescence microscopy was used to examine the overall distribution of RuDCBPY chromophores within MOF crystallites. The results indicated that at low loadings (<10 m*m*) energy transfer is predominantly one-dimensional, for concentrations ranging from ~10 to ~50 millimolal energy transfer is predominantly two-dimensional, and at high concentrations energy transfer should be three-dimensional.

1.8 Conclusions

Taking inspiration from nature's photosynthetic machinery, scientists have developed a wide-variety of molecular and supramolecular constructs that can serve as model systems for investigating energy transfer. Energy transfer studies on rhenium-based molecular assemblies, porphyrin-based Donor−Bridge−Acceptor systems, pyrene- and porphyrin-based dendrimers, and conjugated polymers have provided useful information about the effect of (a) photophysical properties of chromophores, (b) interchromophoric distances, and (c) relative orientation of chromophores on energy transfer. Metal-organic frameworks (MOF) have attracted great interest from the scientific community due to their unique structural features and diverse set of applications. In the last two decades, a vast amount of research has been dedicated towards exploring the application of MOFs in light-harvesting and energy transfer. Pioneering studies conducted by the Hupp group, Lin group, Meyer group and Morris group have shown that MOFs are capable of demonstrating long-range, directional energy transfer. Furthermore, there is plenty of scope for further improving the energy transfer performance of MOFs. Energy transfer investigations on porphyrin- and RuDCBPY-based MOFs have shown that energy transfer is an intricate process, dependent on factors such as the spectral overlap integral, chromophore

concentrations and solvation environments of chromophores. In order to get a deeper understanding of energy transfer processes in MOFs, the influence of structural parameters (such as interchromophoric distance and relative orientation of chromophores) on the efficiency and directionality of energy transfer needs to be investigated in more detail. Processing of MOFs as thin films is a domain that is still in its nascent stage of development but bears a huge potential for light harvesting and energy transfer applications in the future. Keeping this in mind, more research efforts should be directed towards facile fabrication of high-quality thin films that are robust and crystalline. Exploring novel ideas and concepts such as building MOF-on-MOF heterostructures for studying electron- and energy-transfer processes should be encouraged as they can lead to the discovery of previously unknown structure-property relationships.[33,61] Addressing these challenges can pave the way for a new generation of light harvesting and energy conversion materials.

1.9 References

(1) So, M. C.; Wiederrecht, G. P.; Mondloch, J. E.; Hupp, J. T.; Farha, O. K. Metal-Organic Framework Materials for Light-Harvesting and Energy Transfer. *Chem. Commun.* **2015**, *51* (17), 3501–3510. https://doi.org/10.1039/C4CC09596K.

(2) Zhu, J.; Maza, W. A.; Morris, A. J. Light-Harvesting and Energy Transfer in Ruthenium(II)-Polypyridyl Doped Zirconium(IV) Metal-Organic Frameworks: A Look toward Solar Cell Applications. *J. Photochem. Photobiol. A Chem.* **2017**, *344*, 64–77. https://doi.org/https://doi.org/10.1016/j.jphotochem.2017.04.025.

(3) Förster, T. Zwischenmolekulare Energiewanderung Und Fluoreszenz. *Ann. Phys.* **1948**, *437* (1–2), 55–75. https://doi.org/https://doi.org/10.1002/andp.19484370105.

(4) Förster, T. Transfer Mechanisms of Electronic Excitation Energy. *Radiat. Res. Suppl.*

1960, *2*, 326–339. https://doi.org/10.2307/3583604.

(5) Jameson, D. M.; Croney, J. C.; Moens, P. D. J. B. T.-M. in E. [1] Fluorescence: Basic Concepts, Practical Aspects, and Some Anecdotes. In *Biophotonics, Part A*; Academic Press, 2003; Vol. 360, pp 1–43. https://doi.org/https://doi.org/10.1016/S0076-6879(03)60105-9.

(6) Zhu, J.; Shaikh, S.; Mayhall, N. J.; Morris, A. J. Energy Transfer in Metal-Organic Frameworks. In *Elaboration and Applications of Metal-Organic Frameworks*; Series on Chemistry, Energy and the Environment; WORLD SCIENTIFIC, 2017; Vol. Volume 2, pp 581–654. https://doi.org/doi:10.1142/9789813226739_0014.

(7) Knight, T. E.; McCusker, J. K. Orbital-Specific Energy Transfer. *J. Am. Chem. Soc.* **2010**, *132* (7), 2208–2221. https://doi.org/10.1021/ja907303t.

(8) Knight, T. E.; Guo, D.; Claude, J. P.; McCusker, J. K. Energy Transfer Dynamics in ReI−Based Polynuclear Assemblies: A Quantitative Application of Förster Theory. *Inorg. Chem.* **2008**, *47* (16), 7249–7261. https://doi.org/10.1021/ic800670b.

(9) Soler, M.; McCusker, J. K. Distinguishing between Dexter and Rapid Sequential Electron Transfer in Covalently Linked Donor−Acceptor Assemblies. *J. Am. Chem. Soc.* **2008**, *130* (14), 4708–4724. https://doi.org/10.1021/ja077096i.

(10) Guo, D.; Knight, T. E.; McCusker, J. K. Angular Momentum Conservation in Dipolar Energy Transfer. *Science (80-.).* **2011**, *334* (6063), 1684 LP – 1687. https://doi.org/10.1126/science.1211459.

(11) Eng, M. P.; Ljungdahl, T.; Mårtensson, J.; Albinsson, B. Triplet Excitation Energy Transfer in Porphyrin-Based Donor−Bridge−Acceptor Systems with Conjugated Bridges of Varying Length: An Experimental and DFT Study. *J. Phys. Chem. B* **2006**, *110* (13),

6483–6491. https://doi.org/10.1021/jp056536u.

(12) Albinsson, B.; Eng, M. P.; Pettersson, K.; Winters, M. U. Electron and Energy Transfer in Donor–Acceptor Systems with Conjugated Molecular Bridges. *Phys. Chem. Chem. Phys.* **2007**, *9* (44), 5847–5864. https://doi.org/10.1039/B706122F.

(13) Giribabu, L.; Ashok Kumar, A.; Neeraja, V.; Maiya, B. G. Orientation Dependence of Energy Transfer in an Anthracene–Porphyrin Donor–Acceptor System. *Angew. Chemie Int. Ed.* **2001**, *40* (19), 3621–3624. https://doi.org/https://doi.org/10.1002/1521-3773(20011001)40:19<3621::AID-ANIE3621>3.0.CO;2-D.

(14) Porcu, P.; Vonlanthen, M.; Ruiu, A.; González-Méndez, I.; Rivera, E. Energy Transfer in Dendritic Systems Having Pyrene Peripheral Groups as Donors and Different Acceptor Groups. *Polymers* . 2018. https://doi.org/10.3390/polym10101062.

(15) Rojas-Montoya, S. M.; Vonlanthen, M.; Porcu, P.; Flores-Rojas, G.; Ruiu, A.; Morales-Morales, D.; Rivera, E. Synthesis and Photophysical Properties of Novel Pyrene–Metalloporphyrin Dendritic Systems. *Dalt. Trans.* **2019**, *48* (28), 10435–10447. https://doi.org/10.1039/C9DT00855A.

(16) Zaragoza-Galán, G.; Fowler, M. A.; Duhamel, J.; Rein, R.; Solladié, N.; Rivera, E. Synthesis and Characterization of Novel Pyrene-Dendronized Porphyrins Exhibiting Efficient Fluorescence Resonance Energy Transfer: Optical and Photophysical Properties. *Langmuir* **2012**, *28* (30), 11195–11205. https://doi.org/10.1021/la301284v.

(17) Martínez-Klimov, M. E.; Organista-Mateos, U.; Borja-Miranda, A.; Rivera, M.; Amelines-Sarria, O.; Martínez-García, M. Electrical Properties of Multi-Pyrene/Porphyrin-Dendrimers. *Molecules* . 2015. https://doi.org/10.3390/molecules200917533.

(18) Vonlanthen, M.; Cevallos-Vallejo, A.; Aguilar-Ortíz, E.; Ruiu, A.; Porcu, P.; Rivera, E. Synthesis, Characterization and Photophysical Studies of Novel Pyrene Labeled Ruthenium (II) Trisbipyridine Complex Cored Dendrimers. *Polymer (Guildf).* **2016**, *99*, 13–20. https://doi.org/https://doi.org/10.1016/j.polymer.2016.06.061.

(19) Balzani, V.; Ceroni, P.; Maestri, M.; Saudan, C.; Vicinelli, V. Luminescent Dendrimers. Recent Advances BT - Dendrimers V: Functional and Hyperbranched Building Blocks, Photophysical Properties, Applications in Materials and Life Sciences; Schalley, C. A., Vögtle, F., Eds.; Springer Berlin Heidelberg: Berlin, Heidelberg, 2003; pp 159–191. https://doi.org/10.1007/b11010.

(20) Abd-El-Aziz, A. S.; Abdelghani, A. A.; Wagner, B. D.; Bissessur, R. Advances in Light-Emitting Dendrimers. *Macromol. Rapid Commun.* **2019**, *40* (1), 1800711. https://doi.org/https://doi.org/10.1002/marc.201800711.

(21) Winnik, F. M. Photophysics of Preassociated Pyrenes in Aqueous Polymer Solutions and in Other Organized Media. *Chem. Rev.* **1993**, *93* (2), 587–614. https://doi.org/10.1021/cr00018a001.

(22) Zaragoza-Galán, G.; Fowler, M.; Rein, R.; Solladié, N.; Duhamel, J.; Rivera, E. Fluorescence Resonance Energy Transfer in Partially and Fully Labeled Pyrene Dendronized Porphyrins Studied with Model Free Analysis. *J. Phys. Chem. C* **2014**, *118* (16), 8280–8294. https://doi.org/10.1021/jp501445n.

(23) Schwartz, B. J. Conjugated Polymers as Molecular Materials: How Chain Conformation and Film Morphology Influence Energy Transfer and Interchain Interactions. *Annu. Rev. Phys. Chem.* **2003**, *54* (1), 141–172. https://doi.org/10.1146/annurev.physchem.54.011002.103811.

(24) Beljonne, D.; Pourtois, G.; Silva, C.; Hennebicq, E.; Herz, L. M.; Friend, R. H.; Scholes, G. D.; Setayesh, S.; Müllen, K.; Brédas, J. L. Interchain vs. Intrachain Energy Transfer in Acceptor-Capped Conjugated Polymers. *Proc. Natl. Acad. Sci.* **2002**, *99* (17), 10982 LP – 10987. https://doi.org/10.1073/pnas.172390999.

(25) Nguyen, T.-Q.; Wu, J.; Doan, V.; Schwartz, B. J.; Tolbert, S. H. Control of Energy Transfer in Oriented Conjugated Polymer-Mesoporous Silica Composites. *Science (80-.).* **2000**, *288* (5466), 652 LP – 656. https://doi.org/10.1126/science.288.5466.652.

(26) Stryer, L.; Haugland, R. P. Energy Transfer: A Spectroscopic Ruler. *Proc. Natl. Acad. Sci.* **1967**, *58* (2), 719 LP – 726. https://doi.org/10.1073/pnas.58.2.719.

(27) Kent, C. A.; Liu, D.; Ma, L.; Papanikolas, J. M.; Meyer, T. J.; Lin, W. Light Harvesting in Microscale Metal–Organic Frameworks by Energy Migration and Interfacial Electron Transfer Quenching. *J. Am. Chem. Soc.* **2011**, *133* (33), 12940–12943. https://doi.org/10.1021/ja204214t.

(28) Wang, C.; Xie, Z.; deKrafft, K. E.; Lin, W. Doping Metal–Organic Frameworks for Water Oxidation, Carbon Dioxide Reduction, and Organic Photocatalysis. *J. Am. Chem. Soc.* **2011**, *133* (34), 13445–13454. https://doi.org/10.1021/ja203564w.

(29) Chen, B.; Wang, L.; Xiao, Y.; Fronczek, F. R.; Xue, M.; Cui, Y.; Qian, G. A Luminescent Metal–Organic Framework with Lewis Basic Pyridyl Sites for the Sensing of Metal Ions. *Angew. Chemie Int. Ed.* **2009**, *48* (3), 500–503. https://doi.org/https://doi.org/10.1002/anie.200805101.

(30) Allendorf, M. D.; Bauer, C. A.; Bhakta, R. K.; Houk, R. J. T. Luminescent Metal–Organic Frameworks. *Chem. Soc. Rev.* **2009**, *38* (5), 1330–1352. https://doi.org/10.1039/B802352M.

(31) Férey, G. Hybrid Porous Solids: Past, Present, Future. *Chem. Soc. Rev.* **2008**, *37* (1), 191–214. https://doi.org/10.1039/B618320B.

(32) Flügel, E. A.; Ranft, A.; Haase, F.; Lotsch, B. V. Synthetic Routes toward MOF Nanomorphologies. *J. Mater. Chem.* **2012**, *22* (20), 10119–10133. https://doi.org/10.1039/C2JM15675J.

(33) Furukawa, H.; Cordova, K. E.; O'Keeffe, M.; Yaghi, O. M. The Chemistry and Applications of Metal-Organic Frameworks. *Science (80-.).* **2013**, *341* (August), 974. https://doi.org/10.1126/science.1230444.

(34) Fleming, C. N.; Maxwell, K. A.; DeSimone, J. M.; Meyer, T. J.; Papanikolas, J. M. Ultrafast Excited-State Energy Migration Dynamics in an Efficient Light-Harvesting Antenna Polymer Based on Ru(II) and Os(II) Polypyridyl Complexes. *J. Am. Chem. Soc.* **2001**, *123* (42), 10336–10347. https://doi.org/10.1021/ja016304i.

(35) Shaikh, S.; Chakraborty, A.; Alatis, J.; Cai, M.; Danilov, E. O.; Morris, A. J. Light Harvesting and Energy Transfer in a Porphyrin-Based Metal Organic Framework. *Faraday Discuss.* **2018**. https://doi.org/10.1039/C8FD00194D.

(36) Kent, C. A.; Mehl, B. P.; Ma, L.; Papanikolas, J. M.; Meyer, T. J.; Lin, W. Energy Transfer Dynamics in Metal-Organic Frameworks. *J. Am. Chem. Soc.* **2010**, *132* (37), 12767–12769. https://doi.org/10.1021/ja102804s.

(37) Lee, C. Y.; Farha, O. K.; Hong, B. J.; Sarjeant, A. a; Nguyen, S. T.; Hupp, J.; Hupp, J. T. Strut-to-Strut Energy Transfer in Bodipy and Porphyrin-Based MOFs Light-Harvesting Metal-Organic Frameworks (MOFs): Effi- Cient Strut-to-Strut Energy Transfer in Bodipy and Porphyrin- Based MOFs. *Synthesis (Stuttg).* **2011**, 15858–15861.

(38) Lee, C. Y.; Farha, O. K.; Hong, B. J.; Sarjeant, A. A.; Nguyen, S. T.; Hupp, J. T. Light-

Harvesting Metal–Organic Frameworks (MOFs): Efficient Strut-to-Strut Energy Transfer in Bodipy and Porphyrin-Based MOFs. *J. Am. Chem. Soc.* **2011**, *133* (40), 15858–15861. https://doi.org/10.1021/ja206029a.

(39) Son, H. J.; Jin, S.; Patwardhan, S.; Wezenberg, S. J.; Jeong, N. C.; So, M.; Wilmer, C. E.; Sarjeant, A. A.; Schatz, G. C.; Snurr, R. Q.; et al. Light-Harvesting and Ultrafast Energy Migration in Porphyrin-Based Metal-Organic Frameworks. *J. Am. Chem. Soc.* **2013**, *135* (2), 862–869. https://doi.org/10.1021/ja310596a.

(40) Zhang, Q.; Zhang, C.; Cao, L.; Wang, Z.; An, B.; Lin, Z.; Huang, R.; Zhang, Z.; Wang, C.; Lin, W. FöRster Energy Transport in Metal-Organic Frameworks Is beyond Step-by-Step Hopping. *J. Am. Chem. Soc.* **2016**, *138* (16), 5308–5315. https://doi.org/10.1021/jacs.6b01345.

(41) Son, H.-J.; Jin, S.; Patwardhan, S.; Wezenberg, S. J.; Jeong, N. C.; So, M.; Wilmer, C. E.; Sarjeant, A. A.; Schatz, G. C.; Snurr, R. Q.; et al. Light-Harvesting and Ultrafast Energy Migration in Porphyrin-Based Metal–Organic Frameworks. *J. Am. Chem. Soc.* **2013**, *135* (2), 862–869. https://doi.org/10.1021/ja310596a.

(42) Patwardhan, S.; Jin, S.; Son, H.-J.; Schatz, G. C. Ultrafast Energy Migration in Porphyrin-Based Metal Organic Frameworks (MOFs). *Mater. Res. Soc. Symp. Proc.* **2013**, *1539*, 22–27. https://doi.org/10.1557/opl.2013.987.

(43) Maza, W. A.; Padilla, R.; Morris, A. J. Concentration Dependent Dimensionality of Resonance Energy Transfer in a Postsynthetically Doped Morphologically Homologous Analogue of UiO-67 MOF with a Ruthenium(II) Polypyridyl Complex. *J. Am. Chem. Soc.* **2015**, *137* (25), 8161–8168. https://doi.org/10.1021/jacs.5b03071.

(44) Shaikh, S. M.; Chakraborty, A.; Alatis, J.; Cai, M.; Danilov, E.; Morris, A. J. Light

Harvesting and Energy Transfer in a Porphyrin-Based Metal Organic Framework. *Faraday Discuss.* **2019**, *216* (0), 174–190. https://doi.org/10.1039/C8FD00194D.

(45) Lin, J.; Hu, X.; Zhang, P.; Van Rynbach, A.; Beratan, D. N.; Kent, C. A.; Mehl, B. P.; Papanikolas, J. M.; Meyer, T. J.; Lin, W.; et al. Triplet Excitation Energy Dynamics in Metal-Organic Frameworks. *J. Phys. Chem. C* **2013**, *117* (43), 22250–22259. https://doi.org/10.1021/jp401515r.

(46) Dolgopolova, E. A.; Williams, D. E.; Greytak, A. B.; Rice, A. M.; Smith, M. D.; Krause, J. A.; Shustova, N. B. A Bio-Inspired Approach for Chromophore Communication: Ligand-to-Ligand and Host-to-Guest Energy Transfer in Hybrid Crystalline Scaffolds. *Angew. Chemie Int. Ed.* **2015**, *54* (46), 13639–13643. https://doi.org/https://doi.org/10.1002/anie.201507400.

(47) Otsubo, K.; Haraguchi, T.; Sakata, O.; Fujiwara, A.; Kitagawa, H. Step-by-Step Fabrication of a Highly Oriented Crystalline Three-Dimensional Pillared-Layer-Type Metal–Organic Framework Thin Film Confirmed by Synchrotron X-Ray Diffraction. *J. Am. Chem. Soc.* **2012**, *134* (23), 9605–9608. https://doi.org/10.1021/ja304361v.

(48) Shekhah, O.; Liu, J.; Fischer, R. A.; Wöll, C. MOF Thin Films: Existing and Future Applications. *Chem. Soc. Rev.* **2011**, *40* (2), 1081–1106. https://doi.org/10.1039/C0CS00147C.

(49) Zacher, D.; Shekhah, O.; Wöll, C.; Fischer, R. A. Thin Films of Metal–Organic Frameworks. *Chem. Soc. Rev.* **2009**, *38* (5), 1418–1429. https://doi.org/10.1039/B805038B.

(50) Shekhah, O. Layer-by-Layer Method for the Synthesis and Growth of Surface Mounted Metal-Organic Frameworks (SURMOFs). *Materials* . 2010.

https://doi.org/10.3390/ma3021302.

(51) Araki, K.; Wagner, M. J.; Wrighton, M. S. Layer-by-Layer Growth of Electrostatically Assembled Multilayer Porphyrin Films. *Langmuir* **1996**, *12* (22), 5393–5398. https://doi.org/10.1021/la960024c.

(52) Goswami, S.; Ma, L.; Martinson, A. B. F.; Wasielewski, M. R.; Farha, O. K.; Hupp, J. T. Toward Metal–Organic Framework-Based Solar Cells: Enhancing Directional Exciton Transport by Collapsing Three-Dimensional Film Structures. *ACS Appl. Mater. Interfaces* **2016**, *8* (45), 30863–30870. https://doi.org/10.1021/acsami.6b08552.

(53) Maza, W. A.; Haring, A. J.; Ahrenholtz, S. R.; Epley, C. C.; Lin, S. Y.; Morris, A. J. Ruthenium(Ii)-Polypyridyl Zirconium(Iv) Metal–Organic Frameworks as a New Class of Sensitized Solar Cells. *Chem. Sci.* **2016**, *7* (1), 719–727. https://doi.org/10.1039/C5SC01565K.

(54) Maza, W. A.; Morris, A. J. Photophysical Characterization of a Ruthenium(II) Tris(2,2′-Bipyridine)-Doped Zirconium UiO-67 Metal–Organic Framework. *J. Phys. Chem. C* **2014**, *118* (17), 8803–8817. https://doi.org/10.1021/jp501140r.

(55) Maza, W. A.; Haring, A. J.; Ahrenholtz, S. R.; Epley, C. C.; Lin, S. Y.; Morris, A. J. Ruthenium(II)-Polypyridyl Zirconium(IV) Metal-Organic Frameworks as a New Class of Sensitized Solar Cells. *Chem. Sci.* **2015**, *1* (5), 567. https://doi.org/10.1039/C5SC01565K.

(56) Meyer, T. J. Photochemistry of Metal Coordination Complexes: Metal to Ligand Charge Transfer Excited States. *Pure Appl. Chem.* **1986**, *58* (9), 1193–1206. https://doi.org/doi:10.1351/pac198658091193.

(57) Fleming, C. N.; Maxwell, K. A.; DeSimone, J. M.; Meyer, T. J.; Papanikolas, J. M. Ultrafast Excited-State Energy Migration Dynamics in an Efficient Light-Harvesting

Antenna Polymer Based on Ru(II) and Os(II) Polypyridyl Complexes. *J. Am. Chem. Soc.* **2001**, *123* (42), 10336–10347. https://doi.org/10.1021/ja016304i.

(58) Ward, M. D.; Barigelletti, F. Control of Photoinduced Energy Transfer between Metal-Polypyridyl Luminophores across Rigid Covalent, Flexible Covalent, or Hydrogen-Bonded Bridges. *Coord. Chem. Rev.* **2001**, *216–217*, 127–154. https://doi.org/https://doi.org/10.1016/S0010-8545(00)00409-4.

(59) Tsushima, M.; Ikeda, N.; Nozaki, K.; Ohno, T. Fast Energy Transfer of Charge−Transfer Triplet Excited State (3CT) of [Ru(Bpy)3](PF6)2 to Os2+ at Short Distances in the Crystal. *J. Phys. Chem. A* **2000**, *104* (22), 5176–5180. https://doi.org/10.1021/jp993620z.

(60) Yersin, H.; Kratzer, C. Energy Transfer and Harvesting in [Ru1−xOsx(Bpy)3](PF6)2 and {Λ-[Ru(Bpy)3]Δ-[Os(Bpy)3]}(PF6)4. *Coord. Chem. Rev.* **2002**, *229* (1), 75–93. https://doi.org/https://doi.org/10.1016/S0010-8545(02)00106-6.

(61) Yang, X.; Yuan, S.; Zou, L.; Drake, H.; Zhang, Y.; Qin, J.; Alsalme, A.; Zhou, H.-C. One-Step Synthesis of Hybrid Core–Shell Metal–Organic Frameworks. *Angew. Chemie Int. Ed.* **2018**, *57* (15), 3927–3932. https://doi.org/10.1002/anie.201710019.

2. Role of 3D Structure in Energy Transfer in Mixed-Ligand Metal-Organic Frameworks

2.1 Introduction

Natural photosynthetic units employ membrane-bound pigment-protein assemblies (also known as light-harvesting antenna complexes, LHC's) for capturing solar energy and then funneling it towards the reaction centers of photosystem I (PSI) and photosystem II (PSII) via rapid excitation energy transfer (EET).[1,2] The reaction centers capture this energy and convert it into a usable form of chemical energy. The composition and structural organization of pigment chromophores in LHC's generate an energy gradient, enabling directed energy transfer to the reaction centers. In the last few decades, considerable research effort has been focused on developing artificial light-harvesting model systems that can mimic natural LHC's. A key step towards realizing an artificial light-harvesting system is to design chromophoric arrangements that improve the EET efficiency by (a) enhancing interchromophoric interactions, (b) providing fast and effective energy migration pathways that minimize energy losses and (c) facilitating anisotropic energy transfer.[3] Among all the artificial model systems, metal organic frameworks (MOFs) stand out because of their uniqueness. Comprised of inorganic metal ions/clusters linked through organic ligands, MOFs offer extensive synthetic tunability in terms of component diversity and structural hierarchy.[4–6] The MOF scaffolds can accommodate a high density of chromophores that can absorb sunlight simultaneously and amplify the rate of photon absorption.[7,8] Additionally, the modular nature of MOFs offers access to a wide variety of network topologies and allows precise control over structural parameters such as the position, mutual distance and relative orientation of linkers.[9–12] MOFs are, therefore, ideal candidates to study EET as a function of structural parameters and identify chromophoric arrangements that are conducive to energy

transfer. In this report, we specifically investigate the effect of spatial arrangement of chromophores on EET efficiency and anisotropy in mixed-linker MOFs.

Artificial light harvesting model systems consist of chromophores that can play the role of antenna complexes (initial light absorbers, energy conduits) and reaction centers (energy traps).[1] The choice of initial absorbers, conduits and traps depends on the optical and electronic properties of chromophores. For instance, pyrenes have high molar absorption coefficient, high fluorescence quantum yield, and are known to exhibit efficient homo-FRET (energy transfer between identical chromophores).[13,14] These qualities make pyrenes suitable for the role of initial absorbers and energy conduits. Porphyrins have been extensively utilized as energy acceptors in pyrene-based oligomeric and dendritic systems.[15–17] Due to the substantial overlap between the absorption spectrum of porphyrin and emission spectrum of pyrene, porphyrins are an excellent choice for energy traps. Considering the synthetic maneuverability offered by MOFs and the efficacy of the pyrene-porphyrin donor-acceptor system, pyrene- and porphyrin-based mixed-ligand MOFs can serve as potentially attractive artificial light-harvesting model systems. 1,3,6,8-tetrakis(p-benzoic acid)pyrene (TBAPy) and meso-tetrakis(4-carboxyphenyl)porphyrin (TCPP) are promising candidates for the construction of pyrene- and porphyrin-based mixed-ligand MOFs. These two ligands are of similar size, and have identical symmetry and connectivity. The co-assembly of TBAPy and TCPP in a single MOF has previously been confirmed.[18]

Herein, we present a joint experimental and theoretical investigation to assess the influence of structural parameters of MOFs on strut-to-strut EET. We chose three TBAPy-based MOFs with distinctly different network topologies: ROD-7 ($In_2(OH)_2$TBAPy, frz), NU-901 ($Zr_6(\mu_3\text{-}O)_4(\mu_3\text{-}OH)_4(\text{-}OH)_4(\text{-}OH_2)_4$(TBAPy)$_2$, scu) and NU-1000 ($Zr_6(\mu_3\text{-}O)_4(\mu_3\text{-}OH)_4(\text{-}OH)_4(\text{-}OH_2)_4$(TBAPy)$_2$, csq) to probe the impact of spatial arrangement of TBAPy linkers on the EET efficiency.[19–21] The

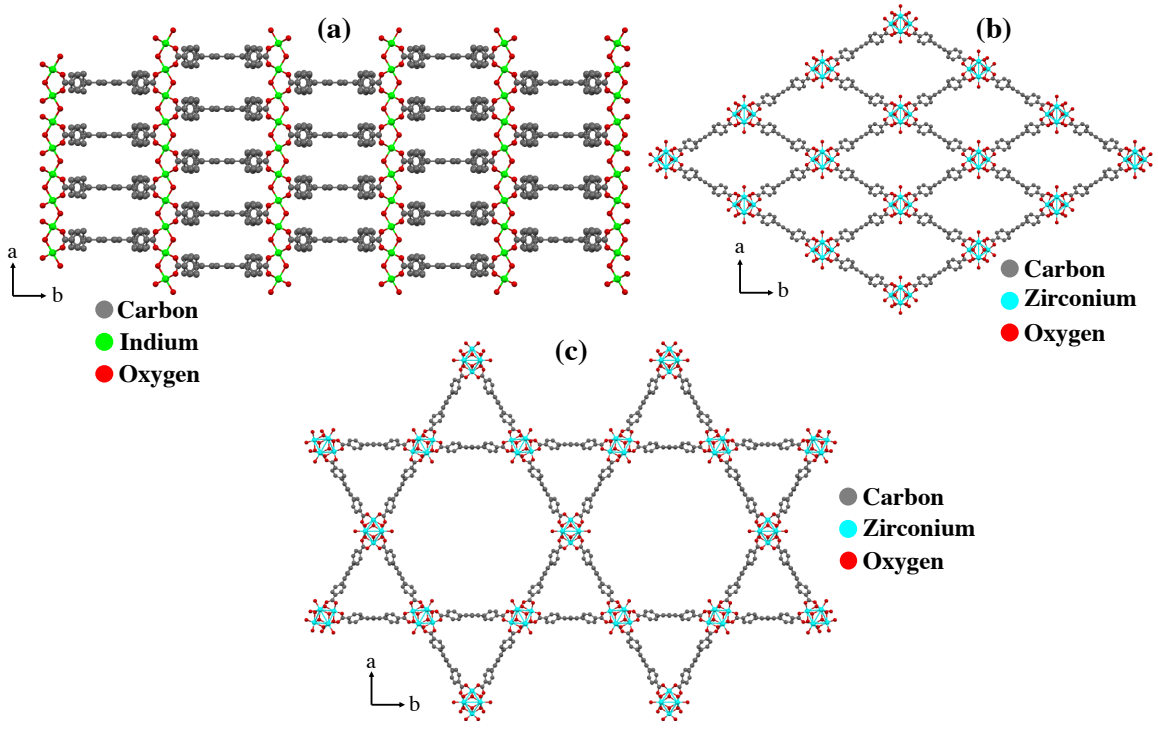

Figure 1. Structures of MOFs viewed along the c-axis: (a) ROD-7, (b) NU-901 and (c) NU-1000

molecular structures of ROD-7, NU-901 and NU-1000 are shown in Figure 1. EET was monitored by incorporating a small number of TCPP units in the MOF backbone (via one-pot solvothermal synthesis) and using them as energy traps. Energy transfer in the MOF crystal occurs via energy exchange between TBAPy linkers until they find a TCPP unit, resulting in quenching of TBAPy fluorescence and amplification of TCPP fluorescence. We hypothesize that the efficiency and directionality of EET in the mixed-ligand MOFs should be influenced by the proximity and orientation of TBAPy linkers in the MOFs. To confirm this hypothesis, we employed steady state and time resolved fluorescence spectroscopy. The efficiency of EET was evaluated using two different approaches. In the first approach, modified Stern-Volmer (S-V) analysis was used to relate the concentration of TCPP in the MOF to the extent of TBAPy quenching. The second approach involved the ratio of the integrated emission intensities of TCPP and TBAPy

(I_{TCPP}/I_{TBAPy}) to calculate the energy transfer efficiency. Both the approaches revealed that EET is most efficient in ROD-7 followed by NU-901 and NU-1000. The energy transfer anisotropy in the three MOFs was assessed through theoretical calculations. Based on excitonic coupling values, the EET rate constants were calculated along different directions. The calculated rate constants suggest that EET in ROD-7 should be significantly more anisotropic than NU-901 and NU-1000.

2.2 Materials and Methods

Materials

1,3,6,8-tetrakis(p-benzoic acid)pyrene was synthesized according to a previously published procedure (Supplementary Information, Section 1). Meso-tetrakis(4-carboxyphenyl)porphyrin (>97%) was purchased from Frontier Scientific and was used without further purification. Indium chloride, 1,4-Dioxane and 4-Aminobencoic acid were purchased from Sigma Aldrich. Zirconyl chloride octahydrate ($ZrOCl_2.8H_2O$) was purchased from Acros organics. Zirconium acetyl acetonate ($Zr(acac)_4$) was purchased from TCI chemicals. Dimethylformamide (DMF, spectrophotometric grade, ≥99.9%), hydrochloric acid (HCl) and sulfuric acid (H_2SO4) were purchased from Fisher chemical. Benzoic acid was purchased from Alfa Aesar and trifluoroacetic acid was purchased from Oakwood chemicals. Deuterated DMSO (DMSO-d_6, 99.9%) was purchased from Cambridge Isotope Laboratories, Inc.

Synthesis of mixed-ligand ROD-7 series

Mixed-ligand ROD-7 samples (ROD-7-TCPP-x, x=1-5) were prepared according to the following procedure. First, $InCl_3$ (3.8×10^{-2} mmol) was added to 75 μL of H_2O and ultrasonically dissolved in 1-dram vials. Then, TBAPy (1.43×10^{-2} mmol for ROD-7-TCPP-1; 1.39×10^{-2} mmol for ROD-7-TCPP-2; 1.35×10^{-2} mmol for ROD-7-TCPP-3; 1.31×10^{-2} mmol for ROD-7-TCPP-4; and 1.27×10^{-2} mmol for ROD-7-TCPP-5) and TCPP (3.16×10^{-4} mmol for ROD-7-TCPP-1;

6.32×10^{-4} mmol for ROD-7-TCPP-2; 9.48×10^{-4} mmol for ROD-7-TCPP-3; 1.26×10^{-3} mmol for ROD-7-TCPP-4; and 1.58×10^{-3} mmol for ROD-7-TCPP-5) of TCPP were added to the reaction mixture. 0.8 ml of DMF was then added to the vials, which were further sonicated for 15 min to get a homogeneous reaction mixture. The vials were placed in an oven set at 120 ^{o}C for 3h. After cooling to room temperature, the resulting mixed-ligand MOF samples were collected using centrifugation. They were washed 5 times with DMF and then soaked in DMF for two days (with fresh DMF replacement every day) to remove any free TBAPy that might have recrystallized. The MOFs were then soaked in acetone, dried at room temperature and then activated by heating at 80 ^{o}C under vacuum.

Synthesis of mixed-ligand NU-901 series

Mixed-ligand NU-901 samples (NU-901-TCPP-x, x=1-5) were prepared according to the following procedure. $Zr(acac)_4$ (0.2 mmol) and 4-aminobenzoic acid (22 mmol) were added to 8 ml of DMF and ultrasonically dissolved in 6-dram vials. The vials were then placed in an oven set at 80 ^{o}C for 1 h. After allowing them to cool down to room temperature, TBAPy (5.77×10^{-2} mmol for NU-901-TCPP-1; 5.69×10^{-2} mmol for NU-901-TCPP-2; 5.61×10^{-2} mmol for NU-901-TCPP-3; 5.53×10^{-2} mmol for NU-901-TCPP-4; and 5.45×10^{-2} mmol for NU-901-TCPP-5) and TCPP (8.22×10^{-4} mmol for NU-901-TCPP-1; 1.64×10^{-3} mmol for NU-901-TCPP-2; 2.46×10^{-3} mmol for NU-901-TCPP-3; 3.29×10^{-3} mmol for NU-901-TCPP-4; and 4.11×10^{-3} mmol for NU-901-TCPP-5) were added to the reaction mixture. The vials were sonicated for 15 min to get a homogeneous reaction mixture and then placed in an oven set at 100^{o} C for 18 h. After cooling to room temperature, the resultant mixed-ligand MOF samples were collected using centrifugation. They were washed 5 times with DMF and then suspended in a vial containing 10 ml of DMF. 0.5 ml of concentrated HCl was added to this suspension and the vials were heated overnight in an

oven set at 100 °C. The purpose of this HCl washing step is to remove the modulators coordinated to the zirconium nodes. Subsequently, the MOF powders were collected using centrifugation, washed 5 times with DMF and then soaked in DMF for two days (with fresh DMF replacement every day) to remove any free TBAPy that might have recrystallized. The MOFs were later soaked in acetone, dried at room temperature and then activated by heating at 80 °C under vacuum.

Synthesis of mixed-ligand NU-1000 series

Mixed-ligand NU-1000 samples (NU-1000-TCPP-x, x=1-5) were prepared according to the following procedure. $ZrOCl_2.8H_2O$ (0.30 mmol) and benzoic acid (16.38 mmol) were added to 8 ml of DMF and ultrasonically dissolved in 6-dram vials. The vials were then placed in an oven set at 100 °C for 1 h. After allowing them to cool down to room temperature, TBAPy (5.77×10^{-2} mmol for NU-1000-TCPP-1; 5.69×10^{-2} mmol for NU-1000-TCPP-2; 5.61×10^{-2} mmol for NU-1000-TCPP-3; 5.53×10^{-2} mmol for NU-1000-TCPP-4; and 5.45×10^{-2} mmol for NU-1000-TCPP-5) and TCPP (8.22×10^{-4} mmol for NU-1000-TCPP-1; 1.64×10^{-3} mmol for NU-1000-TCPP-2; 2.46×10^{-3} mmol for NU-1000-TCPP-3; 3.29×10^{-3} mmol for NU-1000-TCPP-4; and 4.11×10^{-3} mmol for NU-1000-TCPP-5) were added to the reaction mixture. 10 μL TFA (0.13 mmol) was then added to the vials, which were further sonicated for 15 min to get a homogeneous reaction mixture. The vials were then placed in an oven set at 100 °C for 18 h. After cooling to room temperature, the resultant mixed-ligand MOF samples were collected using centrifugation. They were washed 5 times with DMF and then suspended in a vial containing 10 ml of DMF. 0.5 ml of concentrated HCl was added to this suspension and the vials were heated overnight in an oven set at 100 °C. After completely the HCl activation step, the MOF powders were collected using centrifugation, washed 5 times with DMF and then soaked in DMF for two days (with fresh DMF replacement every day) to remove any free TBAPy that might have recrystallized. The MOFs

were later soaked in acetone, dried at room temperature and then activated by heating at 80 ^{o}C under vacuum.

Powder X-ray Diffraction (PXRD)

A 600 W Rigaku MiniFlex powder diffractometer with a CuKα (0.15418 nm) radiation source was used, with a sweeping range of 2–25° in continuous scanning mode. PXRD traces were collected in 0.05° increments at a scanning rate of 0.5°/min.

Scanning Electron Microscopy (SEM)

SEM samples were prepared by suspending MOF powders in ethanol with sonication. The resulting suspensions were drop-casted on precut glass slides. After drying, the glass slides were mounted on SEM sample pegs with the help of double-sided copper tape. The sides of the glass slides and the platform of sample peg were coated with conductive carbon paint purchased from Electron Microscopy Sciences. A LEO (Zeiss) 1550 field-emission scanning electron microscope, equipped with an in-lens detector, operating at 5.0 kV was used to obtain high-resolution images of the MOF particles.

Steady state absorption spectroscopy

The TCPP:TBAPy loading ratios were quantified by digesting the mixed ligand MOFs in ~1M NaOH solution (see Supplementary Information, Section 3). UV-Vis measurements were performed on the digested samples using an Agilent Technologies 8453 UV–Vis diode array spectrophotometer (1 nm resolution). The spectra were recorded with samples prepared in a 1-cm quartz cuvette. The TCPP:TBAPy loading ratio in MOFs range from ~0.01 to 0.5.

Steady-state emission spectroscopy and time-resolved emission lifetimes

Steady-state and time resolved emission measurements were performed on MOF suspensions in DMF (absorbance ~ 0.05). The steady-state emission spectra and quantum yields were obtained

using a QuantaMaster Model QM-200-4E emission spectrophotometer from Photon Technology, Inc. (PTI). The excitation light source was a 75 W Xe arc lamp (Newport). The detector was a thermoelectrically cooled Hamamatsu 1527 photomultiplier tube (PMT). In order to determine the absolute quantum yields, the sample compartment was replaced with an integrating sphere (PTI).

Time-resolved fluorescence lifetimes were obtained via the time-correlated single photon counting technique (TCSPC) with the same QuantaMaster Model QM-200-4E emission spectrophotometer from Photon Technology, Inc. (PTI) equipped with a 340 nm LED and a Becker & Hickl GmbH PMH-100 PMT detector with time resolution of < 220 ps FWHM. Florescence lifetime decays were analyzed with the help of Origin 9.0.

2.3 Computational Methods

2.3.1 Structure optimizations and Excited State Calculations

We first truncated the extended solid-state MOF structures into representative cluster models (Figure 2). We assigned linker "A" as the donor chromophore that can potentially transfer energy to all other TBAPy linkers in the model. Each model consists of several donor-acceptor (D-A) pairs oriented along different directions (e.g., A-B, A-C, A-D, etc). All the zirconium-oxo nodes in the model were removed and protons were added to the carboxylate groups (−COO) for balancing the charge. The structures of the supramolecular D-A pairs were then constrained-optimized at the B3LYP level of theory in vacuum, utilizing cc-pVDZ basis set, such that the carboxylate groups of donor and acceptor were fixed at their corresponding crystallographic coordinates.[23–25] This was done to ensure that the relative orientation of the donor and acceptor does not change during optimization. TDDFT calculations were performed on the optimized structures of donor and acceptor to evaluate their excited state properties at the B3LYP/cc-pVDZ level of theory.[26–28]

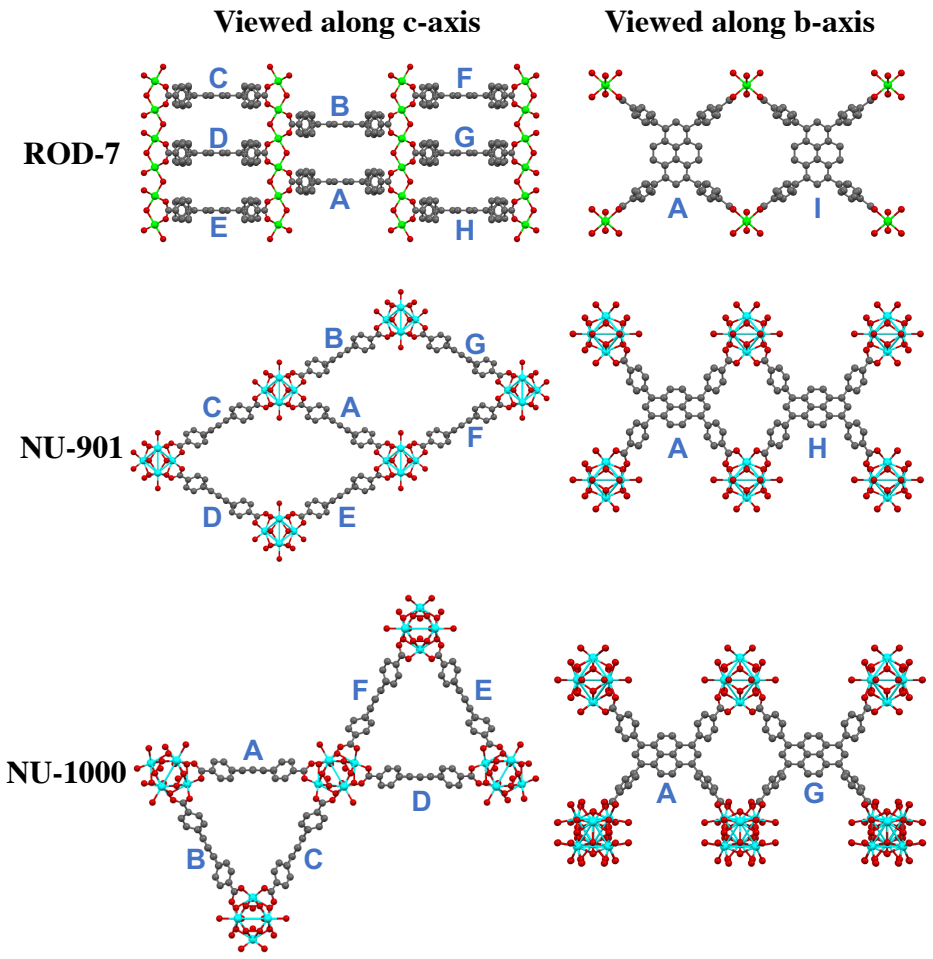

Figure 2. Representative cluster models of ROD-7, NU-901 and (c) NU-1000 viewed along c-axis and b-axis. TBAPy linkers are labelled with letters, "A" being the donor chromophore and other neighboring linkers act as acceptor units.

The choice of the exchange-correlation functional is based on the results of a benchmarking study, where we analyzed the performance of different functionals in computing the energies and electronic configurations of 1st and 2nd excited states of TBAPy monomer. Details regarding the benchmarking study, the software used to calculate excitonic couplings, and oscillator strength calculation are provided in Section 6 of Supplementary Information. All DFT and TDDFT calculations were performed using the Gaussian 09 software package (with the help of WebMO interface).[29,30]

2.3.2 Excitation Energy Transfer Modelling

The rate of EET between two chromophores is heavily dependent on the interactions between their electronic states.[31] Stronger electronic interactions result in faster energy transfer rates. The Coulombic excitonic coupling is a measure of the strength of these intermolecular electronic interactions. Accurate computation of excitonic couplings is therefore of great utility in EET studies. A fairly accurate and computationally cheap approach to calculate excitonic coupling is to decompose the transition density of the individual chromophores into point charges that are localized on atoms.[32–34] These point charges (also known as atomic transition charges, ATC's) can be derived from Mulliken population analysis and used to compute excitonic couplings (eq. 1),

$$J_{ml} = \frac{1}{4\pi\epsilon}\sum_{i}^{N_m}\sum_{j}^{N_l}\frac{q_i\, q_j}{\left(R_i^m - R_j^l\right)} \qquad (1)$$

where q_i and q_j are ATC's on chromophore *m* and chromophore *l* respectively; R_i is the position of atom *i* on chromophore *m* and R_j is the position of atom *j* on chromophore *l*; N_m is the total no. of atoms on chromophore *m* and N_l is the total no. of atoms on chromophore *l*.

The rate constant of EET between adjacent TBAPy chromophores can be calculated using the excitonic couplings (eq. 2),

$$k_{EET} = \frac{2\pi}{\hbar}J^2\mathrm{OI} \qquad (2)$$

where J is the excitonic coupling associated with the S_0-to-S_1 transitions (ground-state to first-excited state transition) and OI is the overlap integral between the experimental absorption and fluorescence spectra of monomeric TBAPy solution.[11,35] The overlap integral was found to be 0.04 eV^{-1}.

In order to compute excitonic couplings, the ATC's associated with the S_1 transition were calculated for each monomer unit from Mulliken population analysis and their values scaled such

that $\Sigma(q_i r_i)^2 = f$, where r_i is the position of atom i and f is the experimental oscillator strength.[34,35] The experimental oscillator strength was determined using eq. 3,

$$f = 1.44 \times 10^{-19} \int \varepsilon(\nu)\, d\nu \quad (3)$$

where $\varepsilon(\nu)$ is the extinction coefficient (in L mol^{-1} cm^{-1}) and ν is the frequency (in Hertz).[34,35] The scaled ATC's were then used for calculating the excitonic couplings between the constituent monomers. Based on eq. 2, the rate constants of EET (k_{EET}) were calculated along different directions.

2.4 Results and Discussion

2.4.1 Synthesis and Structural Characterization

Mixed ligand MOFs of ROD-7, NU-901 and NU-1000 were synthesized as described in Scheme 1. The amounts of TBAPy and TCPP in the reaction mixture were systematically varied to obtain a series of MOFs with different TCPP:TBAPy loading ratios. Son et al. have previously shown that a small amount of quencher can cause amplified fluorescence quenching in MOFs.[25] The amounts of TBAPy and TCPP were therefore chosen such that the TCPP:TBAPy ratios in the resulting MOFs are fairly low (in the range of 1-5%). Details of the synthetic procedures are provided in the Experimental Section. PXRD traces of the resulting mixed-ligand MOF samples were compared to the simulated traces of their respective parent frameworks. The experimental traces of the mixed-ligand MOF samples match with the simulated traces indicating high phase purity (Figure 3). The morphology of mixed-ligand MOF particles was examined with the help of SEM imaging (see Supplementary Information, Section 2). SEM images revealed that the sizes and shapes of mixed-ligand MOF particles match those of the parent frameworks, further confirming that the mixed-ligand MOFs retain the crystalline properties of their parent frameworks.

Scheme 1. Synthesis of mixed-ligand ROD-7, NU-901 and NU-1000 MOFs. Atoms corresponding to TCPP linkers are shown in magenta.

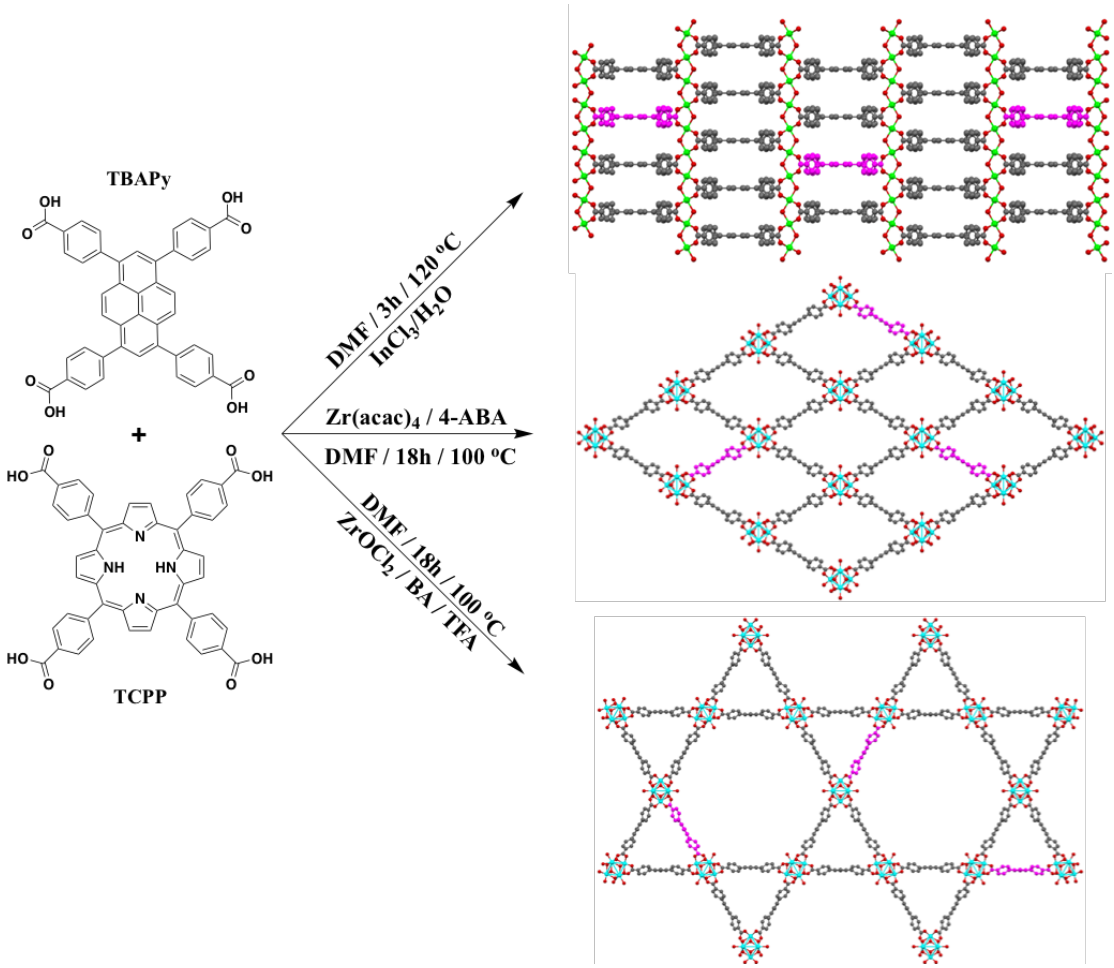

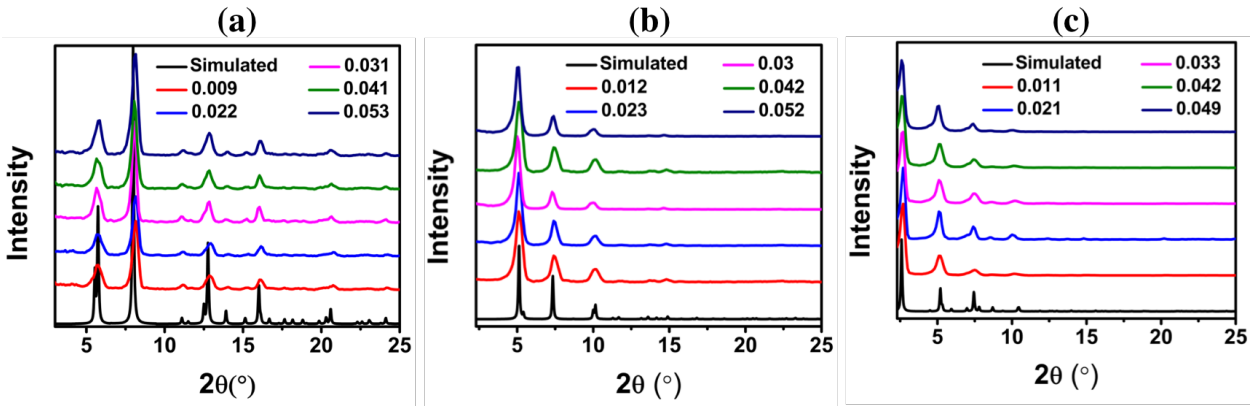

Figure 3. PXRD patterns of mixed-ligand (a)ROD-7, (b) NU-901 and (c) NU-1000 MOFs. The values in the legend indicate the [TCPP]/[TBAPy] loading ratios in MOF sample.

Incorporation of TCPP in the backbone of mixed-ligand MOFs was confirmed with the help of time resolved fluorescence measurements. Immobilization of TCPP in a MOF affects its structural conformation and macrocyclic ring planarity, which in turn affects its fluorescence lifetime. Lifetime of TCPP units in mixed-ligand MOFs is therefore expected to differ from that of free TCPP in solution (see Supplementary Information, Section 7). Furthermore, the lifetime of TCPP units in mixed-ligand MOFs was compared to the lifetime of isostructural TCPP-based MOFs. The lifetimes are quite similar, indicating that TCPP units are part of the backbone of mixed-ligand MOFs. The ratio of TCPP and TBAPy in the mixed-ligand MOFs was quantified by performing electronic absorption measurements on their digested samples (see Supplementary Information, Section 3). MOF samples were weighed and then digested in 1M NaOH solution. The results confirmed that the ratios of TBAPy and TCPP in each of the three series are in the 1-5% range. We prepared a total of nine mixed-ligand MOF series, three for each of the MOFs.

2.4.2 Time resolved fluorescence measurements and Stern-Volmer analysis

To explore the effect of MOF topology on energy transfer dynamics of mixed-ligand MOFs, we performed time resolved fluorescence measurements. MOF samples were excited at 340nm and the emission was monitored at 475 nm. It should be noted that upon excitation at 340 nm, TBAPy emits in the 400-600 nm region and TCPP emits in the 600-750 nm region (see Supplementary Information, Section 4). Given that TCPP emission at 475 nm is negligible, the fluorescence signal from the mixed-ligand MOFs should be exclusively due to TBAPy. The fluorescence decay curves for the ROD-7 series, NU-901 series and NU-1000 series are shown in Figure 4. The decay curves were best fit to a bi-exponential decay model (eq. 4),

$$I(t) = A_1 e^{-t/\tau_1} + A_2 e^{-t/\tau_2} \quad (4)$$

where τ_1 and τ_2 represent the lifetime components (shorter and longer respectively), and A_1 and

A_2 represent their respective relative contributions. Lifetime data extracted from the bi-exponential model revealed that the shorter lifetime (τ_1) is comparable to the lifetime of free TBAPy ligand in solution (see Supplementary Information, Section 4). Thus, τ_1 is attributed to TBAPy linkers in the MOF that exhibit monomeric behavior. The longer lifetime (τ_2) can be attributed to excimer species formed in the MOFs upon excitation. Previous photophysical investigations on ROD-7, NU-901 and NU-1000 have reported that the high number density and close proximity of TBAPy linkers in these MOFs leads to very fast excimer formation dynamics.[35–37]

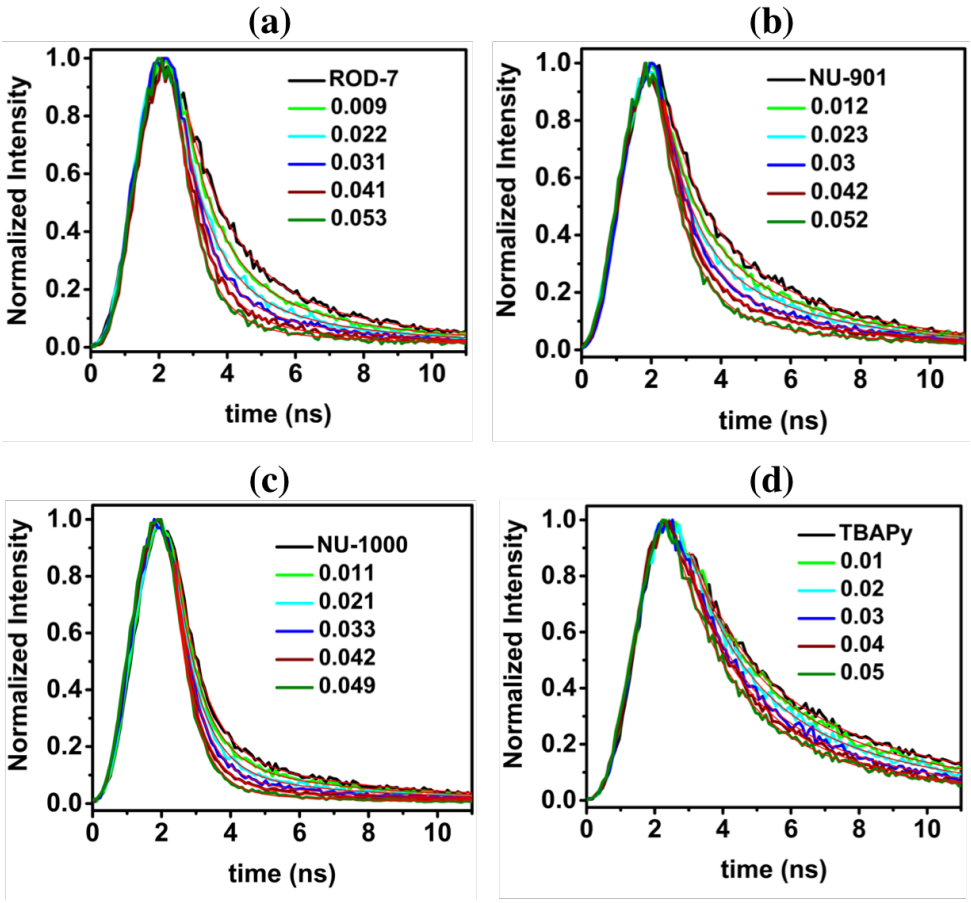

Figure 4. Time resolved emission decay profiles of (a) mixed-ligand ROD-7 samples, (b) mixed-ligand NU-901 samples, (c) mixed-ligand NU-1000 samples, and (d) TBAPy solution. The values in the legend indicate the [TCPP]/[TBAPy] loading ratios in MOF samples and TBAPy solution (λ_{exc} = 340 nm, λ_{em} = 475 nm). The biexponential decay fits (shown in red) are overlaid onto the data curves.

The fluorescence lifetime of a donor chromophore is given by eq. 5,

$$\tau_{donor} = \frac{1}{k_r + k_{nr}} \tag{5}$$

where k_r and k_{nr} are the rates of radiative and non-radiative processes that can depopulate the excited state.[3] EET to an acceptor acts as an additional depopulation pathway causing the lifetime of donor to decrease (eq. 6).

$$\tau_{donor} = \frac{1}{k_r + k_{nr} + k_{EET}} \tag{6}$$

The monomer lifetime (τ_1) in mixed-ligand MOFs was observed to be sensitive to TCPP loading concentration. τ_1 was found to decrease on increasing TCPP loading as shown in Table S1, S2 and S3 (see Supplementary Information, Section 4). This is ascribed to quenching of TBAPy fluorescence via energy transfer to TCPP. A modified Stern-Volmer relationship was employed to relate the extent of TBAPy quenching to the ratio of TCPP and TBAPy concentration in MOF (eq. 7),

$$\frac{\tau_1'}{\tau_1} = 1 + K_{SV}\frac{[\text{TCPP}]}{[\text{TBAPy}]} \tag{7}$$

where τ_1' is the monomer lifetime in the absence of TCPP, τ_1 is the monomer lifetime at a particular loading concentration of TCPP, and K_{SV} is the Stern-Volmer constant. K_{SV} values are the slopes of the linear regression fits of Stern-Volmer plots (Figure 5). The magnitude of K_{SV} can be used for qualitative comparisons of EET efficiency in MOFs, a higher K_{SV} indicating a higher EET efficiency. Average K_{SV} values and the corresponding standard deviations for the three MOFs and TBAPy solution are shown in Table 1.

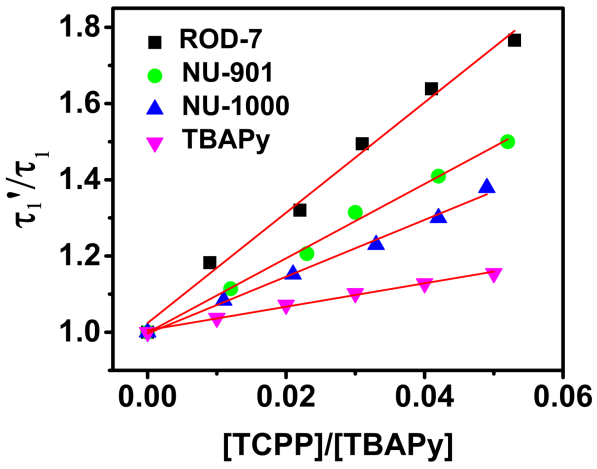

Figure 5. Stern-Volmer plots for ROD-7, NU-901, NU-1000 and TBAPy solution. Linear fits of the data are overlaid onto the data points.

Table 1. Stern-Volmer constants for ROD-7, NU-901, NU-1000 and TBAPy solution

	K_{SV} (M^{-1})	κ^2	R (Å)	J ($nm^4\ M^{-1}cm^{-1}$)	% Φ_D
ROD-7	15.03 ± 0.82	1	7.12	5.41×10^{14}	7.3 ± 1.4
NU-901	10.25 ± 0.99	0.37	9.57	3.79×10^{14}	11.7 ± 1.9
NU-1000	8.16 ± 0.41	0.28	10.62	2.57×10^{14}	16.2 ± 2.2
TBAPy	3.35 ± 0.30	-	-	1.15×10^{14}	58.4 ± 4.9

Comparison of the Stern-Volmer constants revealed two interesting trends. First, K_{SV} value for the TBAPy solution was lower than that of the MOFs suggesting that the strut-to-strut energy transfer mechanism in MOFs outperforms the diffusion-controlled mechanism in solution phase. Facilitated by favorable alignment of chromophores, MOFs are able to demonstrate efficient, long-range energy transfer.[9,12,38] Second, among the three MOFs, EET efficiency is highest in ROD-7, followed by NU-901 and NU-1000. In order to understand this trend, we analyzed interchromophoric distances (R) and orientation factors (κ^2) of TBAPy linkers that are most closely positioned in space. Deria et al. have previously shown that interchromophoric interactions in these MOFs predominantly originate from the two most closely spaced linkers.[37] They simulated

the absorption and emission spectrum of dimeric models of the two most closely positioned TBAPy linkers in space and found them to be in good agreement with the corresponding experimental spectra of MOFs. It was thus concluded that structural features of dimeric models can serve as a reasonable representation of the frameworks. Among the three dimeric models in Figure 6, TBAPy chromophores in ROD-7 model are held in closest proximity. Since the TBAPy chromophores in ROD-7 model are arranged in a cofacial manner, it has a higher κ^2 as well. According to the Förster theory for energy transfer, the efficiency of energy transfer between the two TBAPy chromophores is given by eq. 8,

$$E = \frac{1}{1 + \left(\frac{R}{R_0}\right)^6} \tag{8}$$

where R is the donor-acceptor distance and R_0 is the Forster distance,

$$R_0 = \left(\frac{9000(\ln 10)\kappa^2 \Phi_D J}{128\pi^5 N_A n^4}\right)^{\frac{1}{6}} \tag{9}$$

where κ^2 is the orientation factor, J is the spectral overlap integral, Φ_D is the fluorescence quantum yield of donor in the absence of acceptor, and n is the refractive index of the surrounding media.[3,39]

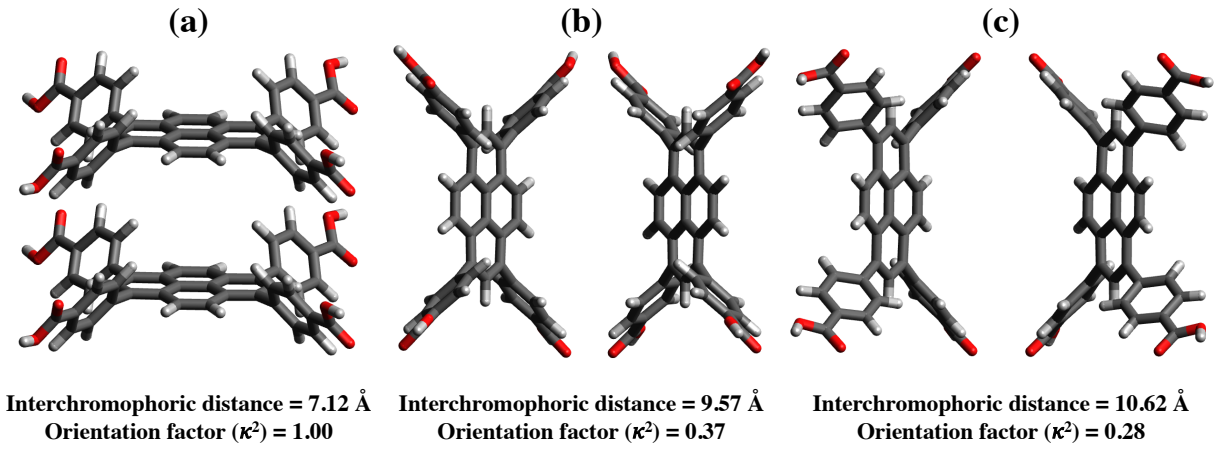

Figure 6. Dimeric models of the most closely positioned TBAPy linkers in (a) ROD-7, (b) NU-901 and (c) NU-1000

Based on eq. 8 and 9, it can be inferred that the higher EET efficiency in ROD-7 is a result of shorter R and larger κ^2 value. The shorter the interchromophoric distance, the stronger is the electronic coupling between the excited states of donor and acceptor chromophores. Similarly, a larger κ^2 value means that the transition dipole moments of chromophores are favourably oriented to undergo rapid energy transfer. Between NU-901 and NU-1000, R and κ^2 values favor NU-901, which is reflected in its higher K_{SV} value.

According to equations 8 and 9, the spectral overlap integral (*J*) and quantum yield of donor (Φ_D) also influence the energy transfer efficiency. To probe the impact of spectral overlap integral, we calculated the *J* values for the three MOFs and TBAPy solution (see Supplementary Information, Section 2.6.8). Table 1 indicates that the spectral overlap integrals also influence the energy transfer efficiency in ROD-7, NU-901 and NU-1000. Larger magnitudes of *J* result in higher K_{SV} values and, therefore, higher EET efficiencies. It is expected that MOFs with larger quantum yields should demonstrate higher energy transfer efficiencies. However, we see an opposite trend in Table 1. For instance, ROD-7 has the smallest quantum yield but demonstrates the largest K_{SV} value. Thus, we concluded that quantum yields have little to no impact on energy transfer efficiencies.

2.4.3 EET efficiency of mixed-ligand MOFs

Steady state fluorescence measurements were performed to calculate the EET efficiencies in the mixed-ligand MOFs (Figure 7). The MOFs were excited at 340nm and the fluorescence intensity was monitored in the 400-750 nm range. Emission peaks corresponding to TBAPy (λ_{max} = 450 nm) and TCPP (λ_{max} = 650 nm) were observed in the spectra. The intensity of these peaks is influenced by energy transfer events taking place between TBAPy and TCPP. It should be noted that some of the TBAPy and TCPP units in the MOF assembly do not participate in energy transfer

and emit directly after excitation. The peak intensities should therefore have contribution from (a) direct emission and (b) emission arising from EET events. The fluorescence intensity corresponding to the TCPP population in the MOF is given by eq. 10,

$$\mathrm{I_{TCPP}} = (k \times \mathrm{C_{TCPP}} \times \Phi_{\mathrm{TCPP}} \times \varepsilon_{\mathrm{TCPP}}) + \left(k \times \mathrm{C_{TBAPy}} \times \Phi_{\mathrm{TCPP}} \times \varepsilon_{\mathrm{TBAPy}} \times \mathrm{E}\right) \quad (10)$$

where k is a proportionality constant that accounts for instrumental response, C_{TBAPy} and C_{TCPP} are the respective loading concentrations of TBAPy and TCPP in the mixed-ligand MOF samples, Φ_{TBAPy} and Φ_{TCPP} are emission quantum yields of TBAPy and TCPP respectively, ε_{TBAPy} and ε_{TCPP} are the molar absorption coefficients of TBAPy and TCPP respectively, and E is the EET efficiency.[40] The first term in eq. 7 represents fluorescence due to direct emission and the second term represents fluorescence contribution from EET.

Similarly, the fluorescence intensity corresponding to the TBAPy population is given by eq. 11,

$$\mathrm{I_{TBAPy}} = \left(k \times \mathrm{C_{TBAPy}} \times \Phi_{\mathrm{TBAPy}} \times \varepsilon_{\mathrm{TBAPy}}\right) - \left(k \times \mathrm{C_{TBAPy}} \times \Phi_{\mathrm{TCPP}} \times \varepsilon_{\mathrm{TBAPy}} \times \mathrm{E}\right) \quad (11)$$

Equation 10 and 11 were employed to derive the expression for EET efficiency (eq. 12, see Section 5 of Supplementary Information for complete derivation),

$$\mathrm{E} = \frac{\left(\mathrm{I'} \times \Phi_{\mathrm{TBAPy}} \times \varepsilon_{\mathrm{TBAPy}}\right) - \left(\eta \times \Phi_{\mathrm{TCPP}} \times \varepsilon_{\mathrm{TCPP}}\right)}{\left(\mathrm{I'} \times \Phi_{\mathrm{TCPP}} \times \varepsilon_{\mathrm{TBAPy}}\right) + \left(\Phi_{\mathrm{TCPP}} \times \varepsilon_{\mathrm{TBAPy}}\right)} \quad (12)$$

where I′ is the ratio of the integrated emission intensities of TCPP and TBAPy (I_{TCPP}/I_{TBAPy}) and was obtained using steady state fluorescence measurements. η is the ratio of the loading concentrations of TCPP and TBAPy (C_{TCPP}/C_{TBAPy}).

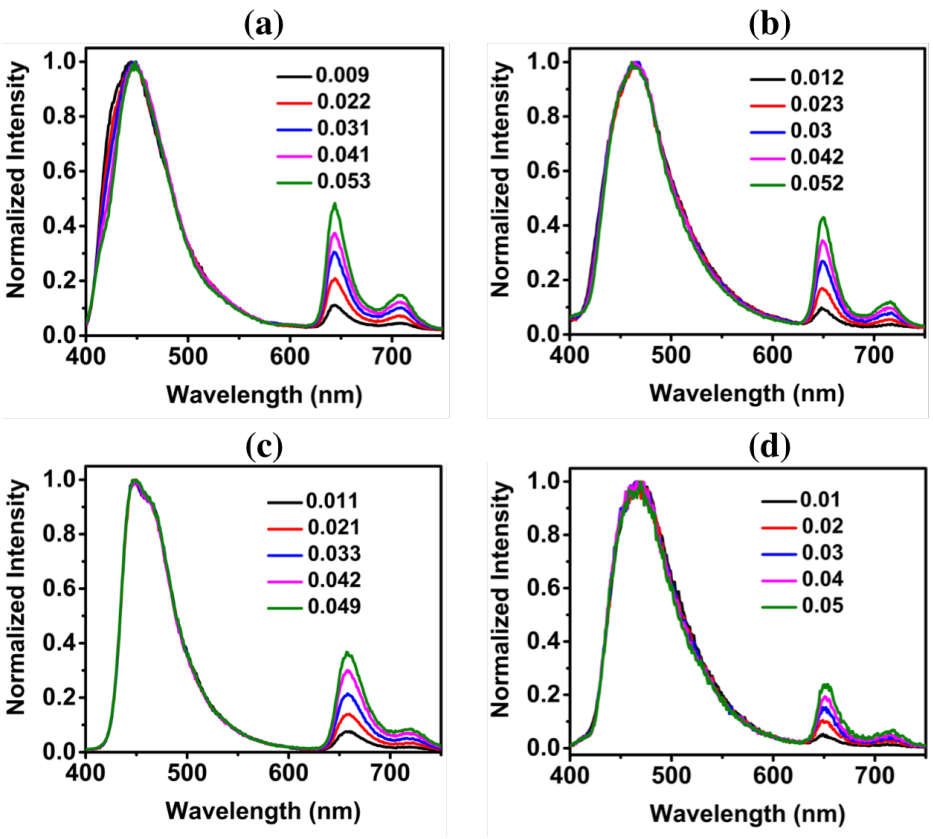

Figure 7. Normalized steady state fluorescence spectra of (a) mixed-ligand ROD-7 samples, (b) mixed-ligand NU-901 samples, (c) mixed-ligand NU-1000 samples, and (d) TBAPy solution. The values in the legend indicate the [TCPP]/[TBAPy] loading ratios in MOF samples and TBAPy solution (λ_{exc} = 340 nm).

The calculated EET efficiencies for mixed-ligand MOFs and for TBAPy solution are reported in Table S4, S5, S6 (See Supplementary Information, Section 6). In order to better understand the dependence of EET efficiency on MOF structure, the efficiencies were plotted against η and fit to a linear regression model (Figure 8). Using the trendline equations, the EET efficiencies corresponding to η = 0.02 were calculated for the MOFs and the solution (Table 3). The efficiencies are in the following order: ROD-7 > NU-901 > NU-1000 > TBAPy-solution. The results of this experiment agree with the findings of time resolved fluorescence measurements (Section 3.2), further confirming that structural parameters of a MOF such as interchromophoric distance and κ^2 dictate its EET efficiency.

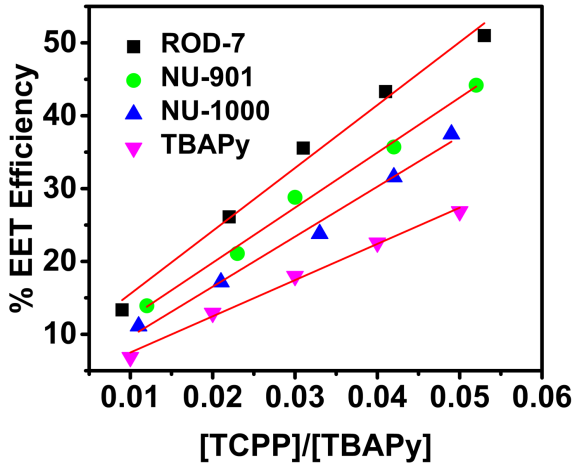

Figure 8. %EET efficiencies plotted against the [TCPP]/[TBAPy] loading ratios of ROD-7, NU-901, NU-1000 and TBAPy solution. Linear fits of the data are overlaid onto the data points.

Table 3. %EET efficiencies (corresponding to $\eta = 0.02$) for the MOFs and TBAPy solution

	%EET efficiency @ $\eta = 0.02$
ROD-7	25.48 ± 1.41
NU-901	19.81 ± 1.13
NU-1000	16.73 ± 0.98
TBAPy	11.44 ± 0.76

2.4.4 Excitonic couplings and EET anisotropy in MOFs

Excitonic couplings and energy transfer rate constants (k_{EET}) calculated based on atomic transition charges are shown in Table 4. In ROD-7, the energy transfer rate constant is largest along the A-B direction (stacking direction), almost an order of magnitude larger than each of the other directions. However, in NU-901 and NU-1000, the rate constants along different directions are quite similar in magnitude. Previous studies on EET dynamics in MOFs have shown that the direction with the largest k_{EET} is the preferred energy transfer direction.[34] Energy transfer in ROD-7 is therefore predicted to be significantly anisotropic, and primarily directed along the A-B direction (Figure 9). On the other hand, energy transfer in NU-901 and NU-1000 is expected to be

more isotropic than in ROD-7, spread-out along five (A-B, A-E, A-C, A-F, A-H) and three (A-B, A-C, A-G) different directions respectively. Directional energy transfer is less likely to be achieved in NU-901 and NU-1000.

Table 4. Calculated excitonic couplings and energy transfer rate constants (k_{EET}) along different directions in ROD-7, NU-901 and NU-1000

ROD-7	**Excitonic coupling (eV)**	$\boldsymbol{k_{EET}}$ **(s^{-1})**
A-B	0.006	7.12×10^9
A-D, A-E, A-G, A-H, A-I	0.002	7.91×10^8
A-C, A-F	0.001	1.98×10^8
NU-901		
A-B, A-E	0.004	3.16×10^9
A-C, A-F, A-H	0.003	1.78×10^9
A-D, A-G	0.001	1.98×10^8
NU-1000		
A-B, A-C	0.004	3.16×10^9
A-G	0.003	1.78×10^9
A-D, A-E, A-F	0.001	1.98×10^8

The underlying network topologies of NU-901 and NU-1000 have higher connectivity and are more intricate than the topology of ROD-7. Consequently, the number of TBAPy linkers in a given volume of space is greater for NU-901 and NU-1000. With more competing energy transfer pathways, EET anisotropy in NU-901 and NU-1000 is diminished relative to ROD-7.

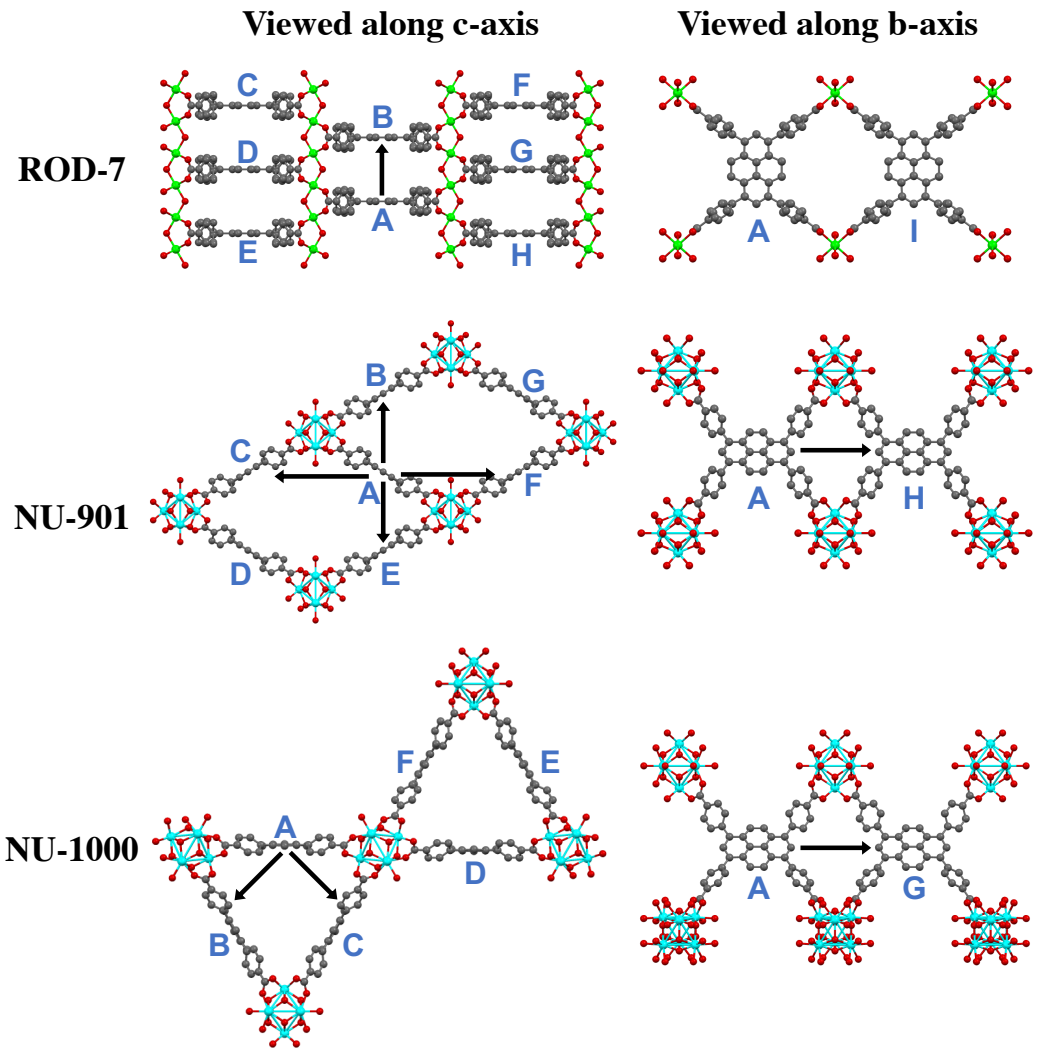

Figure 9. Preferred energy transfer directions in the representative cluster models of ROD-7, NU-901 and (c) NU-1000 (shown by arrows in black).

2.5 Conclusions

A series of mixed-ligand ROD-7 (ROD-7-TCPP-1 to ROD-7-TCPP); NU-901 (NU-901-TCPP-1 to NU-901-TCPP-5); and NU-1000 (NU-1000-TCPP-1 to NU-1000-TCPP-5) samples were prepared solvothermally by adding appropriate ratios of 1,3,6,8-tetrakis(p-benzoic acid)pyrene (TBAPy) and meso-tetrakis(4-carboxy-phenyl)porphyrin (TCPP) in the synthesis. Phase-purity of these samples was confirmed using PXRD and SEM imaging. Time resolved and steady state fluorescence spectroscopy were employed to study the photophysical properties of

mixed-ligand MOFs. Stern-Volmer plots (constructed using lifetime data) and EET efficiency calculations revealed that energy transfer is sensitive to the 3D structure of MOFs. The magnitudes of Stern-Volmer quenching constants (K_{SV}) for ROD-7, NU-901 and NU-1000 were found to be 15.03 ± 0.82 M^{-1}, 10.25 ± 0.99 M^{-1} and 8.16 ± 0.41 M^{-1} respectively, indicating that TBAPy fluorescence is quenched to a greater extent in ROD-7 as compared to NU-901 and NU-1000. EET efficiencies calculated with the help of steady-state fluorescence data further supported the trend observed in K_{SV} values. To understand this trend, we analyzed the interchromophoric distances (R) and orientation factors (κ^2) of dimeric models of ROD-7, NU-901 and NU-1000. Interchromophoric distance and κ^2 influence the strength of electronic communication between TBAPy chromophores, which in turn influences the EET efficiency. A correlation between the spectral overlap integrals (*J*) and EET efficiency was also observed. Larger the magnitude of *J*, higher is the K_{SV} and %EET efficiency. The superior EET performance of ROD-7 is therefore attributed to shorter interchromophoric distance, larger κ^2 value, and larger *J* value. Moreover, a control experiment was performed to assess how EET efficiency in MOFs compares to that in solution phase. Efficiency in solution was inferior to MOFs, signalling that the ligand-to-ligand energy transfer mechanism in MOFs is more effective than the diffusion-controlled solution mechanism. Finally, EET anisotropy in these MOFs was evaluated by calculating excitonic couplings between adjacent TBAPy linkers using the atomic transition charges approach. The couplings were used to calculate the rate constants of EET along different directions. Energy migration in ROD-7 is estimated to be highly anisotropic along the stacking direction. The highly efficient, directional energy transfer in ROD-7 suggests that it can potentially serve as the light harvesting and energy-transfer component in artificial light harvesting devices.

2.6 Supplementary Information

2.6.1 Synthesis of 1,3,6,8-tetrakis(p-benzoic acid)pyrene

TBAPy was synthesized according to a previously published procedure.[20] A mixture of (4-(methoxycarbonyl)phenyl)boronic acid (1.040 g, 5.80 mmol), 1,3,6,8- tetrabromopyrene (0.500 g, 0.97 mmol), tetrakis(triphenylphosphine) palladium(0) (0.030 g 0.026 mmol), and potassium tribasic phosphate (1.100 g, 5.30 mmol) in dry dioxane (20 mL) was loaded into a 50 mL round bottom flask. This mixture was stirred under argon for 72 h at 130°C in an oil bath. The reaction mixture was evaporated to dryness and the solid residue was washed with water to remove inorganic salts. The insoluble material was extracted with chloroform (three times by 50 mL), the extract was dried over magnesium sulfate, and the solvent volume was reduced under vacuum. The residue was boiled in tetrahydrofuran for 2h and filtered; the resulting filtrate contained mainly impurities. This procedure gave 0.34 g of 1,3,6,8-tetrakis(4- (methoxycarbonyl)phenyl)pyrene.

To a 250 mL round bottom flask containing 0.34 g of solid 1,3,6,8-tetrakis(4-(methoxycarbonyl)phenyl)pyrene, a solution containing 1.2 g NaOH in 80 mL of a THF/water (ratio 1:1) mixture was added and the resultant suspension was vigorously stirred under reflux overnight. The solvents were removed under vacuum and water was added to the residue which formed a clear yellow solution. The clear yellow solution was stirred at room temperature for 2 h and the pH value was adjusted to 1 using concentrated HCl. The resulting yellow solid was collected by filtration, and washed with water several times. The crude product was recrystallized from DMF, filtered, washed with chloroform and dried under vacuum. This gave 0.24 g of the pure product TBAPy.

^{1}H NMR (400 MHz, DMSO-d_6): δ 8.20 (s, 4H), 8.16 (d, 8H), 8.08 (s, 2H), 13.1 (s, 4H), 7.86 (d, 8H)

2.6.2 Scanning electron microscopy images

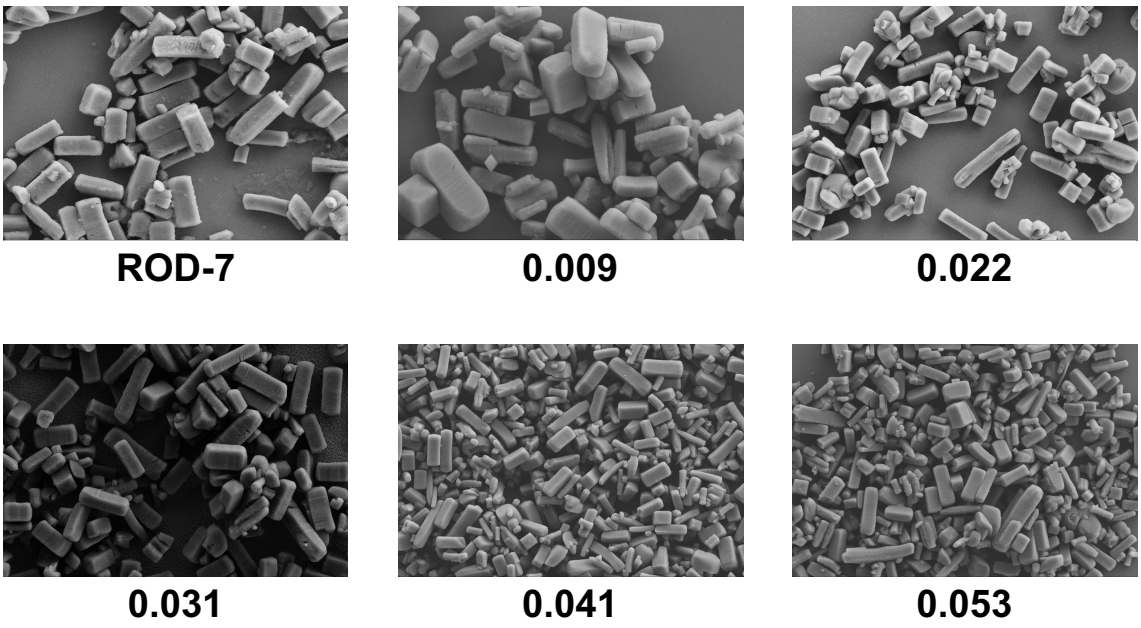

Figure S1. SEM-images of mixed-ligand ROD-7 MOFs. The values below the images indicate the [TCPP]/[TBAPy] loading ratios in MOF samples.

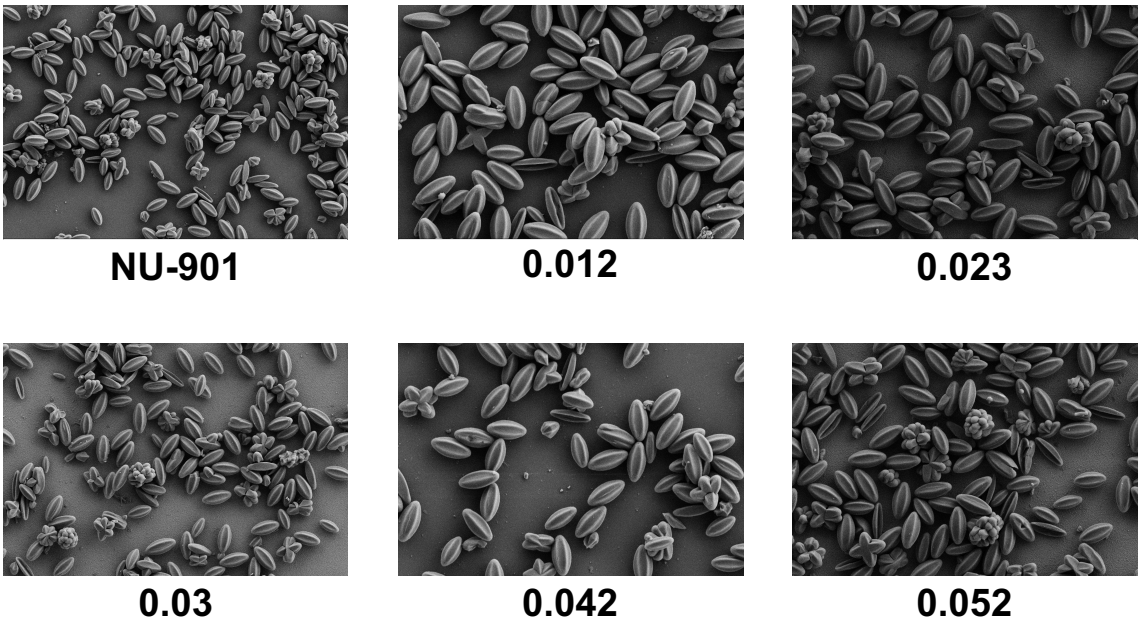

Figure S2. SEM-images of mixed-ligand NU-901 MOFs. The values below the images indicate the [TCPP]/[TBAPy] loading ratios in MOF samples.

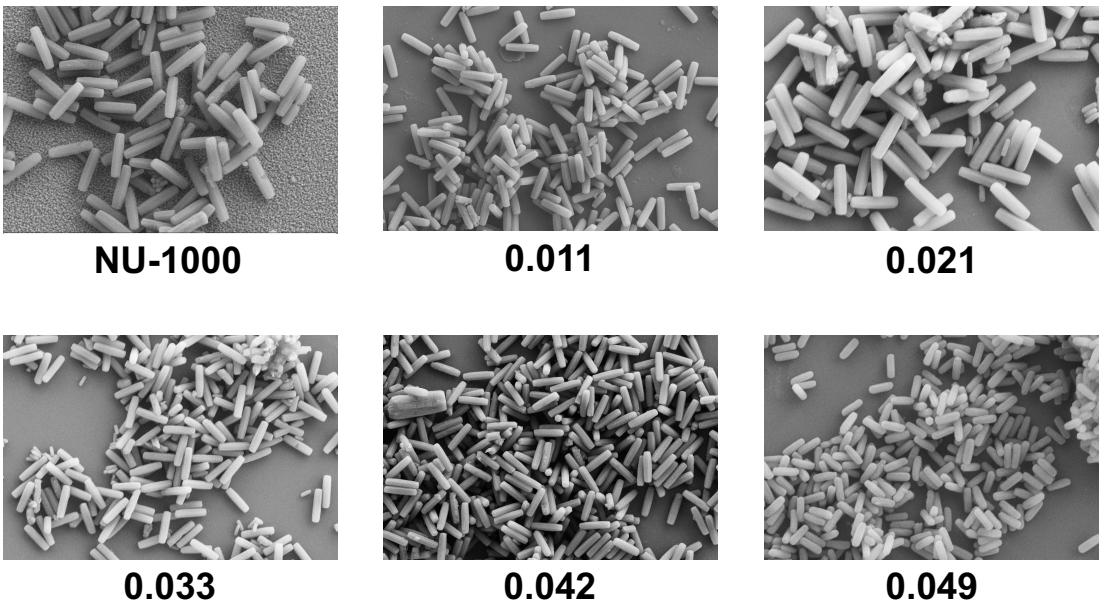

Figure S3. SEM-images of mixed-ligand NU-1000 MOFs. The values below the images indicate the [TCPP]/[TBAPy] loading ratios in MOF samples.

2.6.3 Electronic absorption (UV-Vis) measurements on digested MOF samples

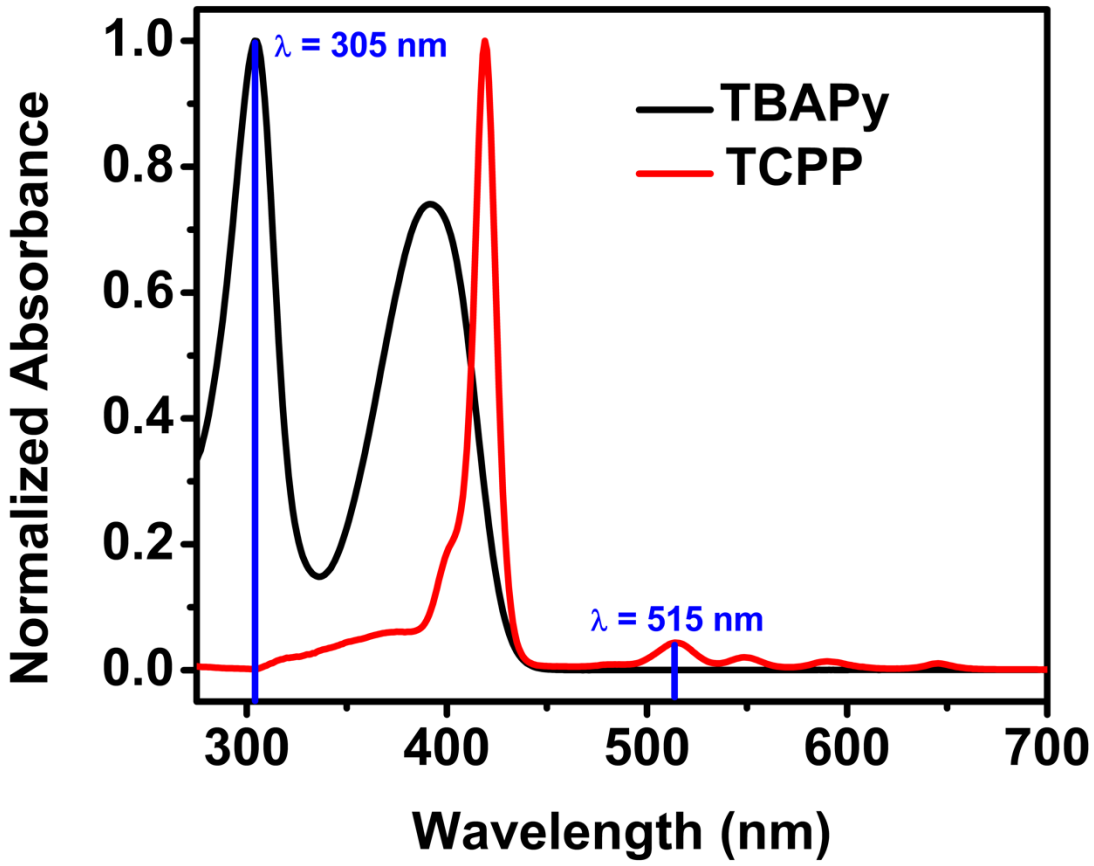

Figure S4. Electronic asorption spectrum of TBAPy and TCPP in 1 M NaOH solution

λ = 305 nm → Only TBAPy absorbs at this wavelength

λ = 515 nm → Only TCPP absorbs at this wavelength

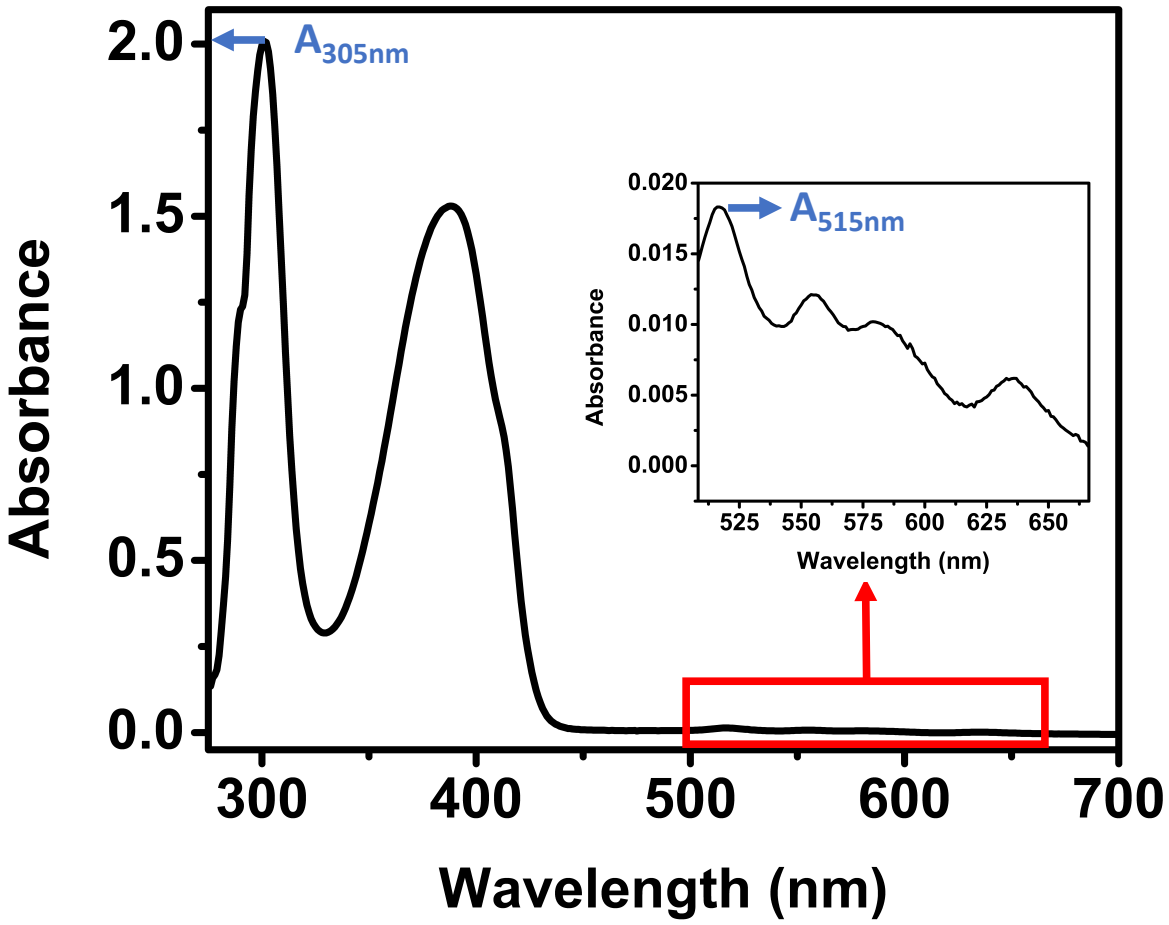

Figure S5. Electronic absorption spectrum of a mixed-ligand ROD-7 MOF digested in a 1 M NaOH solution

$$\frac{A_{305nm}}{A_{515nm}} = \frac{\varepsilon(TBAPy)_{305nm} \times l \times C_{TBAPy}}{\varepsilon(TCPP)_{515nm} \times l \times C_{TCPP}}$$

$$\frac{C_{TCPP}}{C_{TBAPy}} = \frac{\varepsilon(TBAPy)_{305nm} \times l \times A_{515nm}}{\varepsilon(TCPP)_{515nm} \times l \times A_{305nm}}$$

$$\frac{C_{TCPP}}{C_{TBAPy}} = \frac{(47383\ M^{-1}cm^{-1}) \times (1\ cm) \times (0.018)}{(19007\ M^{-1}cm^{-1}) \times (1\ cm) \times (2.01)}$$

$$\frac{C_{TCPP}}{C_{TBAPy}} = 0.022$$

2.6.4 Time resolved fluorescence measurements

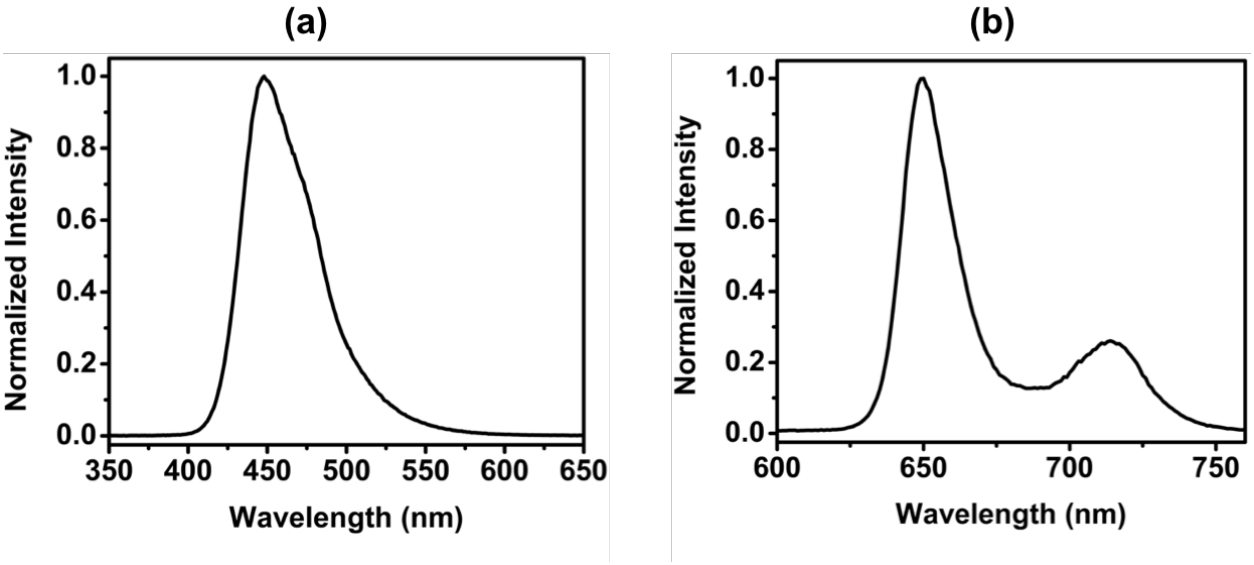

Figure S6. Fluorescence spectrum of (a) TBAPy (10^{-6} M, DMF) and (b) TCPP (10^{-6} M, DMF)

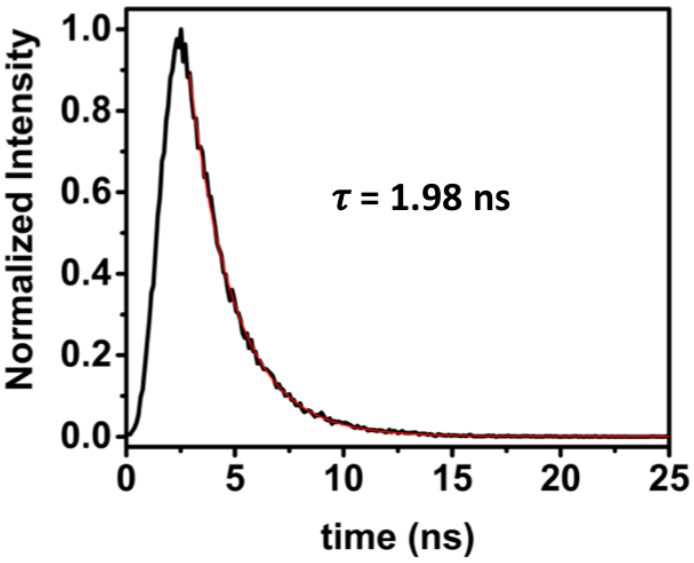

Figure S7. Time resolved emission decay profile of monomeric TBAPy (10^{-6} M, DMF). The mono-exponential decay fit (shown in red) is overlaid onto the data curve.

Series-1

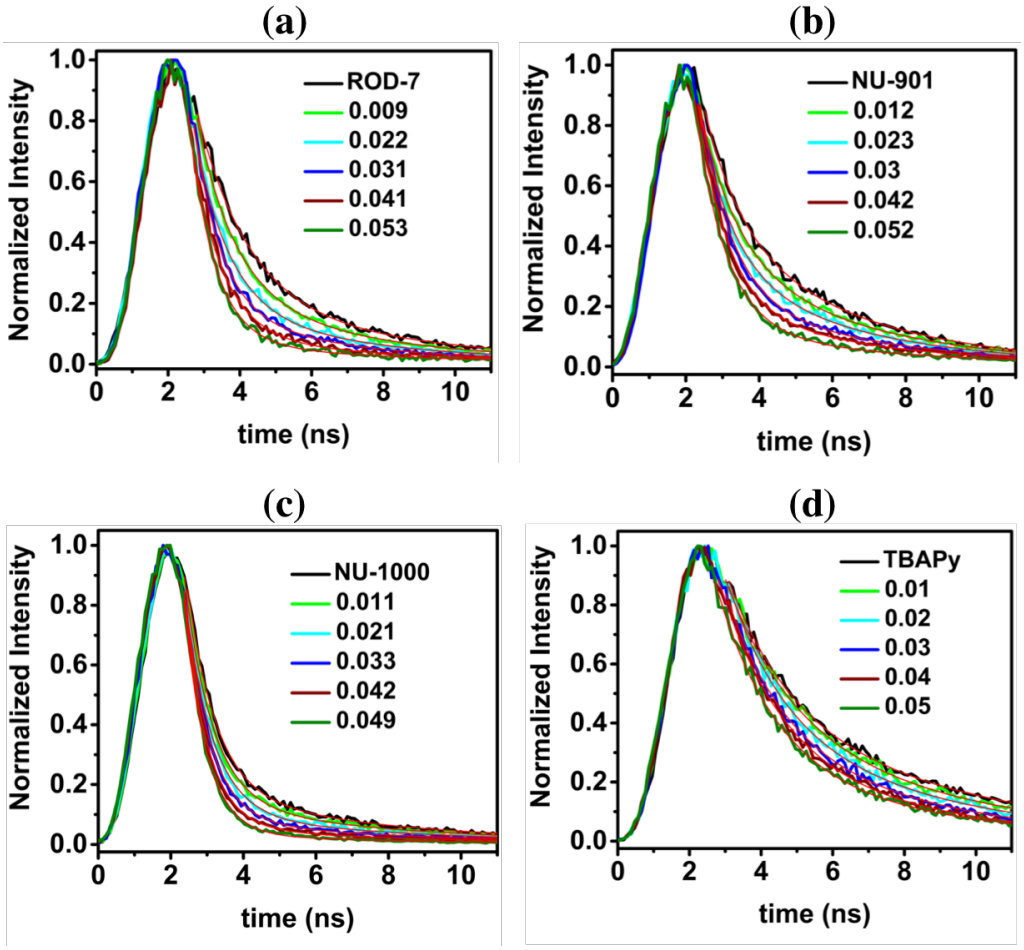

Figure S8. Time resolved emission decay profiles of (a) mixed-ligand ROD-7 samples, (b) mixed-ligand NU-901 samples, (c) mixed-ligand NU-1000 samples, and (d) TBAPy solution (10^{-3} M) for the first series. The biexponential decay fits (shown in red) are overlaid onto the data curves. The values in the legend indicate the [TCPP]/[TBAPy] loading ratios in MOF samples and TBAPy solution (λ_{exc} = 340 nm, λ_{em} = 475 nm).

Series-2

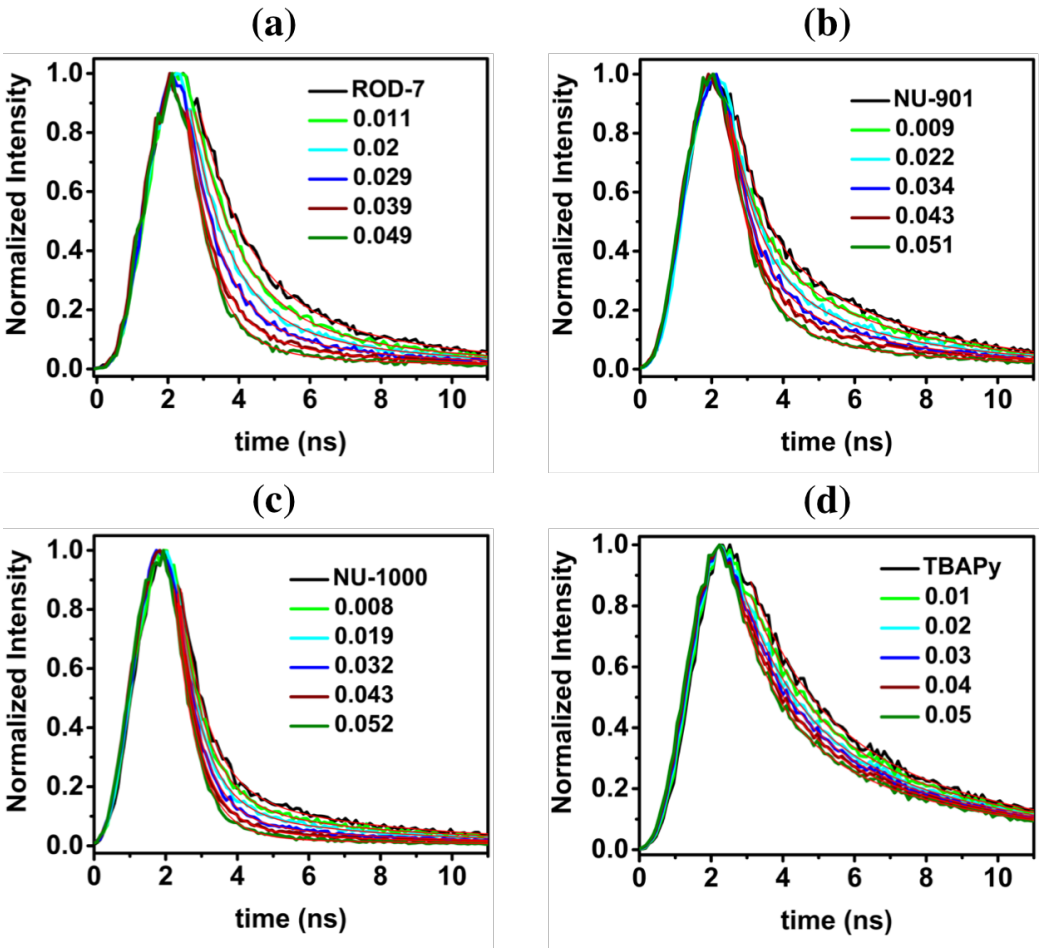

Figure S9. Time resolved emission decay profiles of (a) mixed-ligand ROD-7 samples, (b) mixed-ligand NU-901 samples, (c) mixed-ligand NU-1000 samples, and (d) TBAPy solution (10^{-3} M) for the second series. The biexponential decay fits (shown in red) are overlaid onto the data curves. The values in the legend indicate the [TCPP]/[TBAPy] loading ratios in MOF samples and TBAPy solution (λ_{exc} = 340 nm, λ_{em} = 475 nm).

Series-3

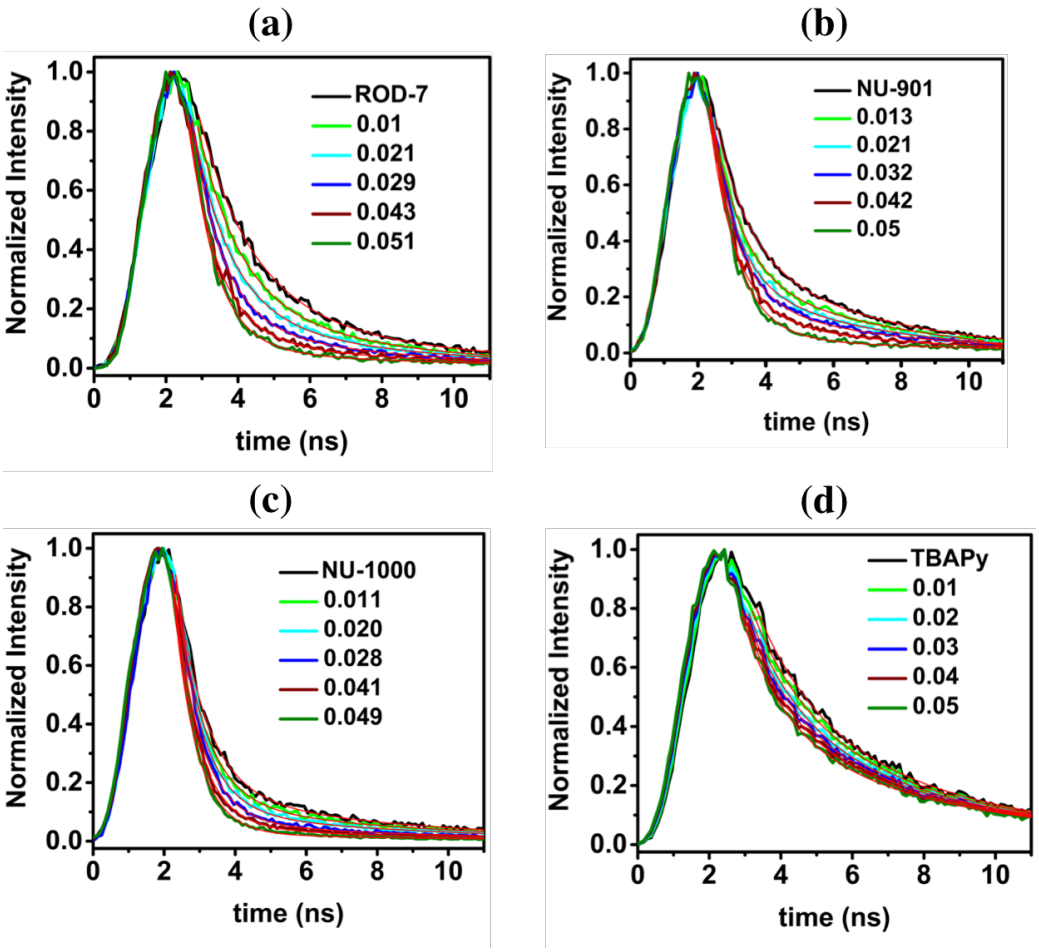

Figure S10. Time resolved emission decay profiles of (a) mixed-ligand ROD-7 samples, (b) mixed-ligand NU-901 samples, (c) mixed-ligand NU-1000 samples, and (d) TBAPy solution (10^{-3} M) for the third series. The biexponential decay fits (shown in red) are overlaid onto the data curves. The values in the legend indicate the [TCPP]/[TBAPy] loading ratios in MOF samples and TBAPy solution (λ_{exc} = 340 nm, λ_{em} = 475 nm).

Table S1. Lifetime data for Series-1. τ_1 and τ_2 are the two observed lifetimes. A_1 and A_2 represent the relative contributions of τ_1 and τ_2 respectively.

ROD-7					NU-901				
[TCPP]/[TBAPy]	A_1	τ_1 (ns)	A_2	τ_2 (ns)	[TCPP]/[TBAPy]	A_1	τ_1 (ns)	A_2	τ_2 (ns)
0	0.62	**1.36**	0.38	4.51	0	0.73	**1.16**	0.27	4.49
0.009	0.64	**1.15**	0.36	4.39	0.012	0.76	**1.05**	0.24	4.71
0.022	0.7	**1.03**	0.30	4.65	0.023	0.69	**0.97**	0.31	4.6
0.031	0.58	**0.91**	0.42	4.82	0.03	0.78	**0.90**	0.22	4.95
0.041	0.67	**0.83**	0.33	4.34	0.042	0.74	**0.84**	0.26	4.48
0.053	0.65	**0.77**	0.35	4.43	0.052	0.79	**0.79**	0.21	4.41
NU-1000					TBAPy solution				
[TCPP]/[TBAPy]	A_1	τ_1 (ns)	A_2	τ_2 (ns)	[TCPP]/[TBAPy]	A_1	τ_1 (ns)	A_2	τ_2 (ns)
0	0.81	**0.91**	0.19	5.07	0	0.42	**1.94**	0.58	5.24
0.011	0.83	**0.84**	0.17	4.69	0.01	0.49	**1.87**	0.51	5.42
0.021	0.77	**0.79**	0.23	5.26	0.02	0.39	**1.81**	0.61	5.02
0.033	0.85	**0.74**	0.15	4.74	0.03	0.45	**1.76**	0.55	5.59
0.042	0.8	**0.7**	0.2	5.13	0.04	0.46	**1.72**	0.54	5.13
0.049	0.87	**0.65**	0.13	4.89	0.05	0.52	**1.68**	0.48	5.28

Table S2. Lifetime data for Series-2. τ_1 and τ_2 are the two observed lifetimes. A_1 and A_2 represent the relative contributions of τ_1 and τ_2 respectively.

ROD-7					NU-901				
[TCPP]/[TBAPy]	A_1	τ_1 (ns)	A_2	τ_2 (ns)	[TCPP]/[TBAPy]	A_1	τ_1 (ns)	A_2	τ_2 (ns)
0	0.65	**1.41**	0.35	4.59	0	0.68	**1.19**	0.32	4.56
0.011	0.59	**1.21**	0.41	4.42	0.009	0.72	**1.08**	0.28	4.28
0.02	0.69	**1.06**	0.31	4.35	0.022	0.77	**0.95**	0.23	4.37
0.029	0.63	**0.94**	0.37	4.68	0.034	0.73	**0.87**	0.27	4.35
0.039	0.59	**0.86**	0.41	4.54	0.043	0.75	**0.81**	0.25	4.58
0.049	0.67	**0.8**	0.33	4.39	0.051	0.80	**0.77**	0.20	4.47
NU-1000					TBAPy solution				
[TCPP]/[TBAPy]	A_1	τ_1 (ns)	A_2	τ_2 (ns)	[TCPP]/[TBAPy]	A_1	τ_1 (ns)	A_2	τ_2 (ns)
0	0.78	**0.94**	0.22	4.75	0	0.47	**1.91**	0.53	5.04
0.008	0.82	**0.86**	0.18	5.13	0.01	0.41	**1.85**	0.59	5.51
0.019	0.86	**0.77**	0.14	4.81	0.02	0.48	**1.81**	0.52	5.17
0.032	0.83	**0.72**	0.17	5.41	0.03	0.36	**1.74**	0.64	5.37
0.043	0.89	**0.69**	0.11	4.89	0.04	0.41	**1.68**	0.59	5.26
0.052	0.86	**0.65**	0.14	4.96	0.05	0.43	**1.65**	0.57	5.34

Table S3. Lifetime data for Series-3. τ_1 and τ_2 are the two observed lifetimes. A_1 and A_2 represent the relative contributions of τ_1 and τ_2 respectively.

ROD-7					NU-901				
[TCPP]/[TBAPy]	A_1	τ_1 (ns)	A_2	τ_2 (ns)	[TCPP]/[TBAPy]	A_1	τ_1 (ns)	A_2	τ_2 (ns)
0	0.62	**1.37**	0.38	4.33	0	0.66	**1.20**	0.34	4.29
0.01	0.64	**1.21**	0.36	4.49	0.013	0.70	**1.08**	0.30	4.41
0.021	0.59	**1.07**	0.41	4.58	0.021	0.74	**0.98**	0.26	4.60
0.029	0.65	**0.94**	0.35	4.64	0.032	0.75	**0.89**	0.25	4.52
0.043	0.67	**0.88**	0.33	4.54	0.042	0.78	**0.83**	0.22	4.38
0.051	0.60	**0.77**	0.40	4.40	0.05	0.77	**0.78**	0.23	4.51
NU-1000					TBAPy solution				
[TCPP]/[TBAPy]	A_1	τ_1 (ns)	A_2	τ_2 (ns)	[TCPP]/[TBAPy]	A_1	τ_1 (ns)	A_2	τ_2 (ns)
0	0.84	**0.89**	0.16	5.18	0	0.49	**1.97**	0.51	5.44
0.011	0.88	**0.82**	0.14	4.99	0.01	0.38	**1.89**	0.62	5.18
0.02	0.76	**0.76**	0.24	4.92	0.02	0.44	**1.84**	0.56	5.54
0.028	0.82	**0.71**	0.18	5.44	0.03	0.49	**1.75**	0.51	5.42
0.041	0.79	**0.66**	0.21	4.83	0.04	0.42	**1.71**	0.58	5.25
0.049	0.85	**0.63**	0.15	5.08	0.05	0.47	**1.67**	0.53	5.31

2.6.5 Steady state fluorescence measurements

Series-1

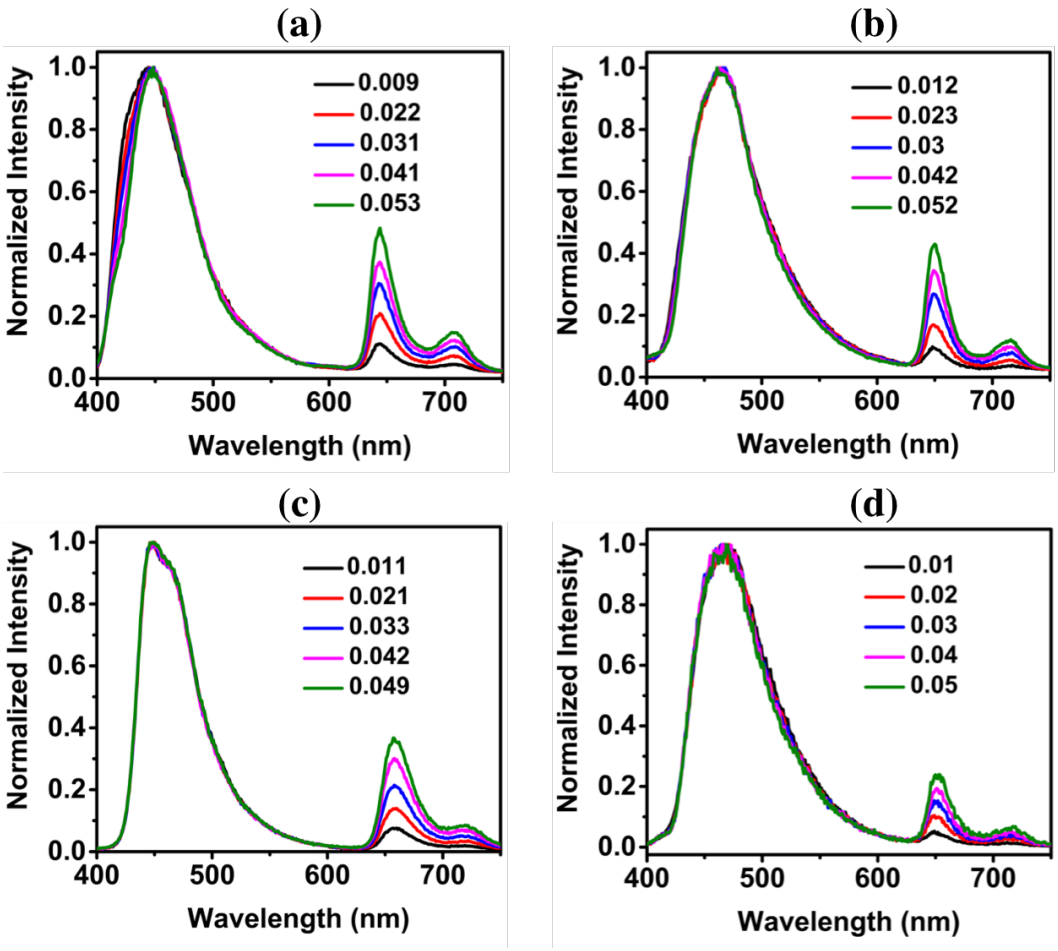

Figure S11. Normalized steady state fluorescence spectra of (a) mixed-ligand ROD-7 samples, (b) mixed-ligand NU-901 samples, (c) mixed-ligand NU-1000 samples, and (d) TBAPy solution (10^{-3} M) for the first series. The values in the legend indicate the [TCPP]/[TBAPy] loading ratios in MOF samples and TBAPy solution (λ_{exc} = 340 nm).

Series-2

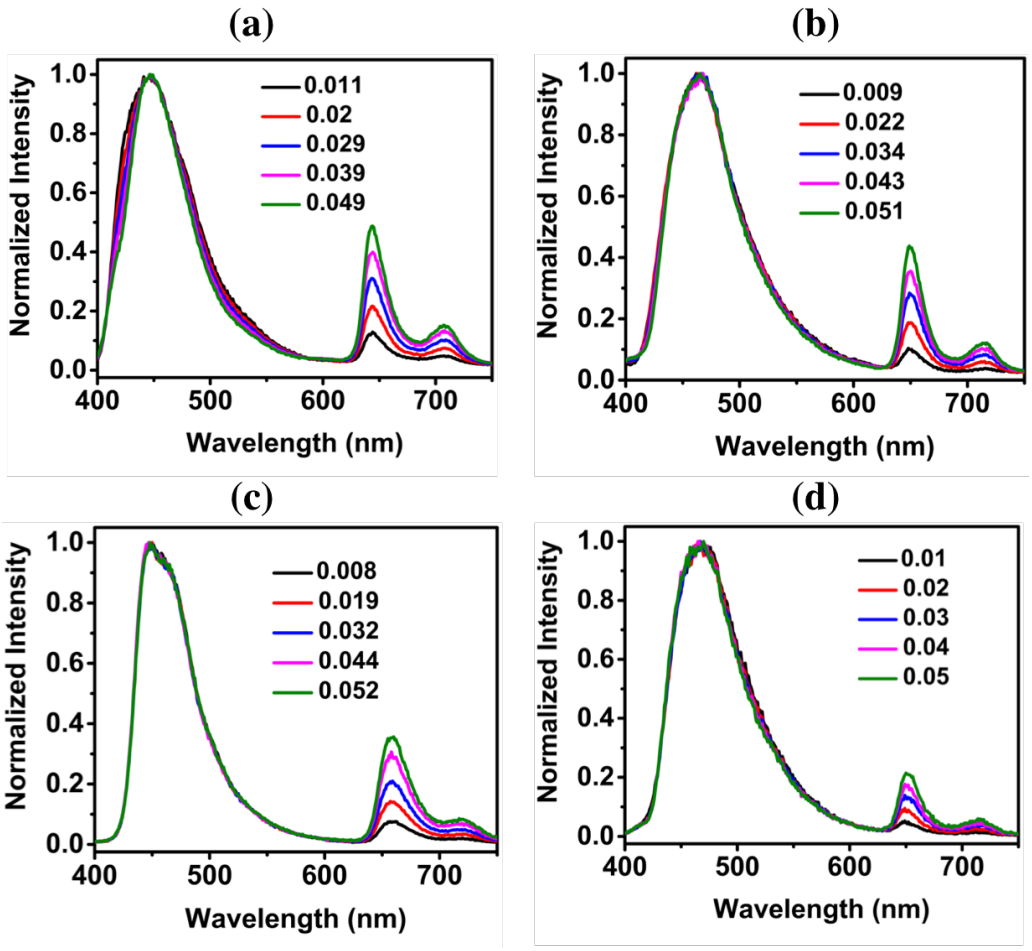

Figure S12. Normalized steady state fluorescence spectra of (a) mixed-ligand ROD-7 samples, (b) mixed-ligand NU-901 samples, (c) mixed-ligand NU-1000 samples, and (d) TBAPy solution (10^{-3} M) phase for the second series. The values in the legend indicate the [TCPP]/[TBAPy] loading ratios in MOF samples and TBAPy solution (λ_{exc} = 340 nm).

Series-3

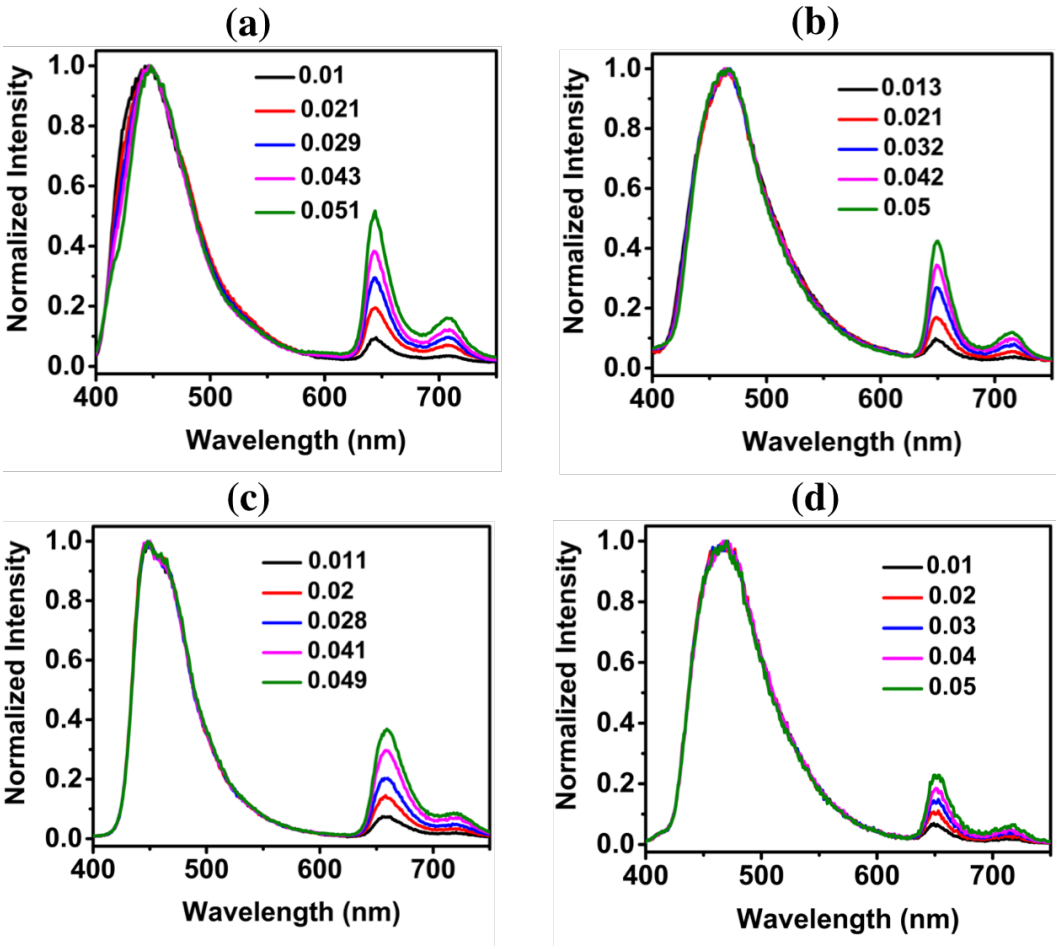

Figure S13. Normalized steady state fluorescence spectra of (a) mixed-ligand ROD-7 samples, (b) mixed-ligand NU-901 samples, (c) mixed-ligand NU-1000 samples, and (d) TBAPy solution (10^{-3} M) phase for the third series. The values in the legend indicate the [TCPP]/[TBAPy] loading ratios in MOF samples and TBAPy solution (λ_{exc} = 340 nm).

Derivation for EET efficiency

The derivation for EET efficiency is based on a previously published report.[40]

The fluorescence intensity corresponding to the TCPP population in the MOF is given by eq. 1,

$$I_{TCPP} = (k \times C_{TCPP} \times \Phi_{TCPP} \times \varepsilon_{TCPP}) + \left(k \times C_{TBAPy} \times \Phi_{TCPP} \times \varepsilon_{TBAPy} \times E\right) \quad (1)$$

where k is a proportionality constant that accounts for instrumental response, C_{TBAPy} and C_{TCPP} are the respective loading concentrations of TBAPy and TCPP in the mixed-ligand MOF samples, Φ_{TBAPy} and Φ_{TCPP} are emission quantum yields of TBAPy and TCPP respectively, ε_{TBAPy} and ε_{TCPP} are the molar absorption coefficients of TBAPy and TCPP respectively, and E is the EET efficiency. The first term in eq. 1 represents fluorescence due to direct emission and the second term represents fluorescence contribution from EET.

Dividing both sides of equation 1 by C_{TBAPy}, we get

$$\frac{I_{TCPP}}{C_{TBAPy}} = (k \times \eta \times \Phi_{TCPP} \times \varepsilon_{TCPP}) + \left(k \times \Phi_{TCPP} \times \varepsilon_{TBAPy} \times E(\eta)\right) \quad (2)$$

The fluorescence intensity corresponding to the TBAPy population is given by eq. 3,

$$I_{TBAPy} = \left(k \times C_{TBAPy} \times \Phi_{TBAPy} \times \varepsilon_{TBAPy}\right) - \left(k \times C_{TBAPy} \times \Phi_{TCPP} \times \varepsilon_{TBAPy} \times E\right) \quad (3)$$

Dividing both sides of eq. 3 by C_{TBAPy}, we get

$$\frac{I_{TBAPy}}{C_{TBAPy}} = \left(k \times \Phi_{TBAPy} \times \varepsilon_{TBAPy}\right) - \left(k \times \Phi_{TCPP} \times \varepsilon_{TBAPy} \times E\right) \quad (4)$$

Now dividing equation 3 by equation 4,

$$\frac{I_{TCPP}}{I_{TBAPy}} = \frac{(\eta \times \Phi_{TCPP} \times \varepsilon_{TCPP}) + \left(\Phi_{TCPP} \times \varepsilon_{TBAPy} \times E\right)}{\left(\Phi_{TBAPy} \times \varepsilon_{TBAPy}\right) - \left(\Phi_{TCPP} \times \varepsilon_{TBAPy} \times E\right)} \quad (5)$$

Rearranging terms,

$$E = \frac{\left(I' \times \Phi_{TBAPy} \times \varepsilon_{TBAPy}\right) - \left(\eta \times \Phi_{TCPP} \times \varepsilon_{TCPP}\right)}{\left(I' \times \Phi_{TCPP} \times \varepsilon_{TBAPy}\right) + \left(\Phi_{TCPP} \times \varepsilon_{TBAPy}\right)} \quad (6)$$

I' is the ratio of the integrated emission intensities of TBAPy and TCPP (I_{TCPP}/I_{TBAPy}) and was obtained using steady state fluorescence measurements. η is the ratio of the loading concentrations of TCPP and TBAPy.

Table S4. Percent efficiency values for Series-1

ROD-7		NU-901	
[TCPP]/[TBAPy]	% efficiency	[TCPP]/[TBAPy]	% efficiency
0.009	15.65	0.012	12.71
0.022	26.11	0.023	21.09
0.031	35.56	0.03	31.80
0.041	40.93	0.042	37.91
0.053	49.99	0.052	44.59
NU-1000		TBAPy soln.	
[TCPP]/[TBAPy]	% efficiency	[TCPP]/[TBAPy]	% efficiency
0.011	10.12	0.01	7.01
0.021	17.34	0.02	12.76
0.033	24.80	0.03	17.86
0.042	33.32	0.04	21.61
0.049	38.72	0.05	25.45

Table S5. Percent efficiency values for Series-2

ROD-7		NU-901	
[TCPP]/[TBAPy]	% efficiency	[TCPP]/[TBAPy]	% efficiency
0.011	17.59	0.009	13.55
0.02	27.31	0.022	22.49
0.029	36.63	0.034	31.13
0.039	43.54	0.043	37.35
0.049	50.15	0.051	44.26
NU-1000		TBAPy soln.	
[TCPP]/[TBAPy]	% efficiency	[TCPP]/[TBAPy]	% efficiency
0.008	10.55	0.01	6.54
0.019	17.27	0.02	10.21
0.032	24.28	0.03	15.92
0.044	32.64	0.04	19.07
0.052	37.20	0.05	22.47

Table S6. Percent efficiency values for Series-3

ROD-7		NU-901	
[TCPP]/[TBAPy]	% efficiency	[TCPP]/[TBAPy]	% efficiency
0.01	14.65	0.013	12.56
0.021	24.42	0.021	20.33
0.029	34.71	0.032	30.41
0.043	41.51	0.042	36.69
0.051	51.70	0.05	44.17
NU-1000		TBAPy soln.	
[TCPP]/[TBAPy]	% efficiency	[TCPP]/[TBAPy]	% efficiency
0.011	9.82	0.01	7.94
0.02	16.81	0.02	12.17
0.028	24.40	0.03	15.83
0.041	33.16	0.04	19.47
0.049	38.95	0.05	23.58

2.6.6 Computational details

Benchmarking studies

A benchmark study of various density functionals was performed to analyze their performance in the characterization of electronic properties of TBAPy monomer. We calculated the energies corresponding to the 1st and 2nd excited state of TBAPy (ES_1 and ES_2) using different functionals, and compared them to published results obtained by multi-reference perturbation theory (MRPT).[41]

Table S7. Excitation energies (in eV) calculated using MRPT (reported in reference 3)

	ES_1	ES_2
MRPT	3.07	3.24

Table S8. Excitation energies (in eV) calculated using different density functionals. Errors values (ΔES_1 and ΔES_2) for the density functionals (= E_{MRPT} - E_{TDDFT}). cc-pVDZ basis set was used for all the calculations.

TDDFT	ES_1	ΔES_1	ES_2	ΔES_2
B3LYP	3.02	0.05	3.43	-0.19
PBE0	3.12	-0.05	3.55	-0.31
M06	3.05	0.02	3.49	-0.25
CAM-B3LYP	3.45	-0.38	3.80	-0.56
wB97X-D	3.49	-0.42	3.82	-0.58
LC-wPBE	3.74	-0.67	3.96	-0.72

We also computed the dominant electronic configurations of ES_1 and ES_2 using different functionals and compared them to the configurations obtained by MRPT (reported in reference 3).

Table S9. Main configurations of the excited states and their weight percentages.

	ES_1	ES_2
MRPT	HOMO → LUMO (87%)	HOMO → LUMO+1 (22%) HOMO-1 → LUMO (21%)
B3LYP	HOMO → LUMO (97%)	HOMO → LUMO+1 (60%) HOMO-1 → LUMO (23%)
PBE0	HOMO → LUMO (97%)	HOMO → LUMO+1 (49%) HOMO-1 → LUMO (30%)
M06	HOMO → LUMO (96%)	HOMO → LUMO+1 (44%) HOMO-1 → LUMO (33%)
CAM-B3LYP	HOMO → LUMO (94%)	HOMO → LUMO+1 (26%) HOMO-1 → LUMO (37%)
wB97X-D	HOMO → LUMO (92%)	HOMO → LUMO+1 (25%) HOMO - 1 → LUMO (36%)
LC-wPBE	HOMO → LUMO (89%)	HOMO → LUMO+1(28%) HOMO-1 → LUMO (36%)

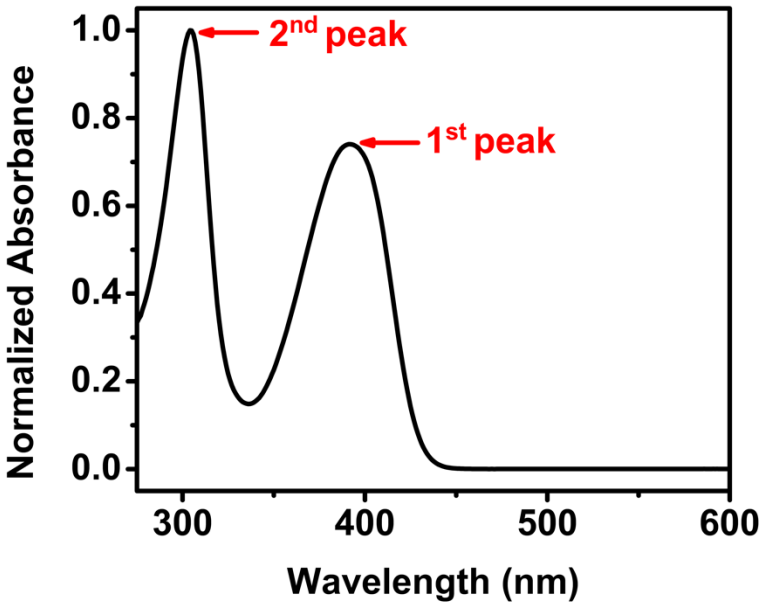

Figure S14. Experimental absorption spectrum of TBAPy with labelled peaks

The excitation energies corresponding to the 1st and 2nd peak (E_1 and E_2) in the absorption spectrum were computed using different functionals, and compared to the experimental values. Polarizable Continuum Model (PCM) was used to simulate the solvation effects of DMF.

Table S10. Excitation energies (in eV) corresponding to the 1st and 2nd peak

	E_1	E_2
Experimental	3.17	4.09

Table S11. Excitation energies (in eV) of 1st and 2nd peak calculated using different density functionals. Errors values (ΔE_1 and ΔE_2) for the density functionals (= $E_{EXPERIMENTAL}$ - E_{TDDFT})

TDDFT	E_1	ΔE_1	E_2	ΔE_2
B3LYP	2.95	0.22	4.12	-0.03
PBE0	3.06	0.11	4.26	-0.17
M06	2.99	0.18	4.20	-0.11
CAM-B3LYP	3.38	-0.21	4.46	-0.37
wB97X-D	3.43	-0.26	4.56	-0.47
LC-wPBE	3.68	-0.51	4.91	-0.82

The hybrid functionals (B3LYP, PBE0 and M06) performed better in characterizing the electronic properties of TBAPy monomer (Table S8, S9 and S11). B3LYP was chosen for calculating excitonic couplings between TBAPy linkers in MOF.

Excitonic coupling calculations

Excitonic couplings were calculated with the help of a software developed that was developed by M. Dommett and is available on github.[24] To evaluate the accuracy of excitonic couplings calculated using the software, we referred to a published paper that reports the excitonic coupling for co-facial dimers of naphthalene, 2-amino-9-methyl-purine, and *trans*-stilbene.[23] We calculated the excitonic coupling for co-facial dimers of these molecules using the software and compared them to values reported in paper. We used B3LYP functional and cc-pVDZ basis set for calculating the excitonic couplings (the paper uses the same functional and basis set). The software used to calculate excitonic couplings reports excitonic couplings only up to three decimal places, while reference 5 gives them up to 4 places.

Naphthalene dimers (excitonic coupling associated with the S_1-S_1 transitions)

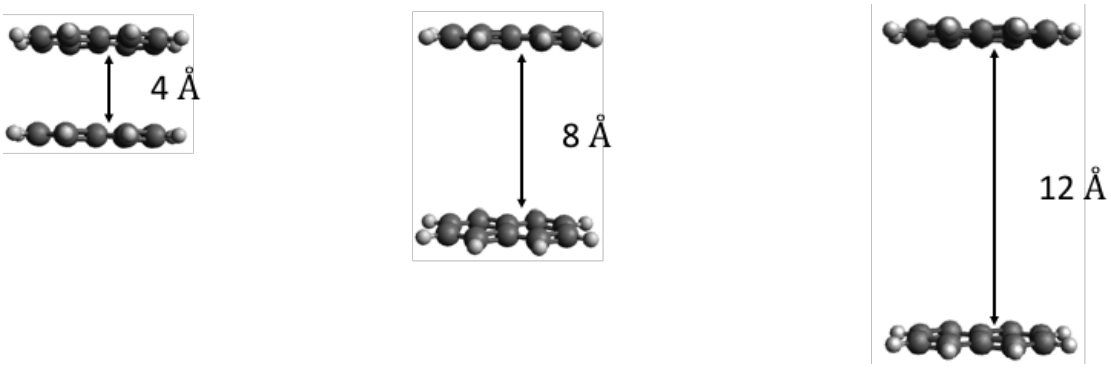

Figure S15. Co-facial naphthalene dimers separated by 4 Å, 8 Å and 12 Å

Table S12. Exitonic couplings (in eV) for co-facial naphthalene dimers

	4 Å	8 Å	12 Å
Calculating using software	0.028	0.005	0.001
Reported in paper	0.0259	0.0043	0.0013
% deviation	8.11%	16.28%	-23.08%

2-amino-9-methyl-purine dimers (excitonic coupling associated with the S_1-S_1 transitions)

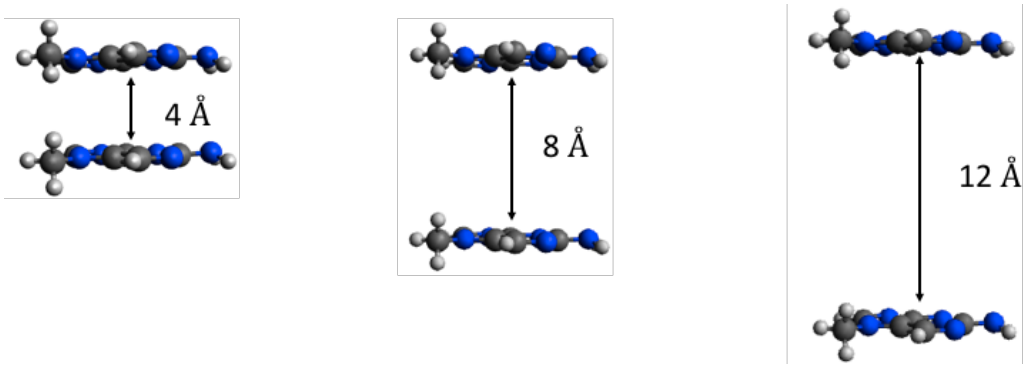

Figure S16. Co-facial 2-amino-9-methyl-purine dimers separated by 4 Å, 8 Å and 12 Å

Table S13. Exitonic couplings (in eV) for co-facial 2-amino-9-methyl-purine dimers

	4 Å	8 Å	12 Å
Calculating using software	0.032	0.006	0.002
Reported in paper	0.0346	0.0066	0.0022
% deviation	-7.51%	-9.09%	-9.09%

trans-stilbene dimers (excitonic coupling associated with the S_1-S_1 transitions)

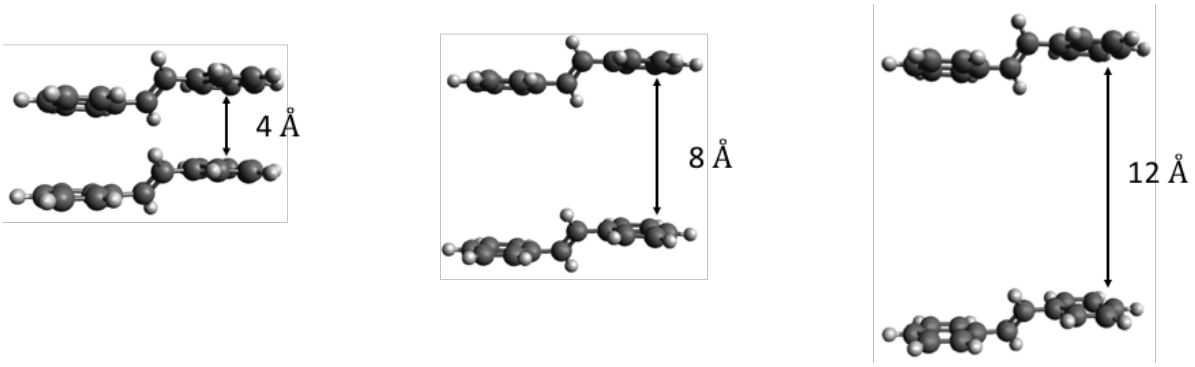

Figure S17. Co-facial *trans*-stilbene dimers separated by 4 Å, 8 Å and 12 Å

Table S14. Exitonic couplings (in eV) for co-facial 2-amino-9-methyl-purine dimers

	4 Å	8 Å	12 Å
Calculating using software	0.092	0.029	0.012
Reported in paper	0.1033	0.0287	0.0111
% deviation	-10.94%	1.04%	8.11%

The excitonic couplings calculated using the software were in good agreement with those reported in the paper.

Oscillator strength Calculation

Oscillator strength was calculated from the absorption spectrum of TBAPy using the eq. 1,

$$f = 1.44 \times 10^{-19} \int \varepsilon(\nu)\, d\nu \qquad (1)$$

where $\varepsilon(\nu)$ is the extinction coefficient (in L mol^{-1} cm^{-1}) and ν is the frequency (in Hertz).[25,26] The absorption spectrum of TBAPy is shown in Figure S13. The calculated oscillator strength for TBAPy is 1.46.

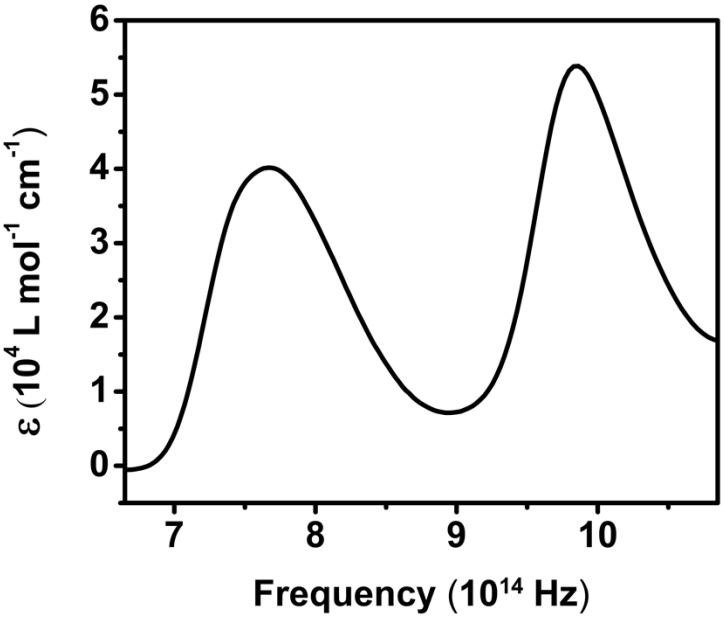

Figure S18. Experimental absorption spectrum of TBAPy (10^{-6} M, DMF) used for determining the oscillator strength

2.6.7 TCPP incorporation in MOF backbone

Indium P-MOF is a TCPP-based MOF that is isostructural with ROD-7.[42] Lifetimes of TCPP units in mixed-ligand ROD-7 MOFs were compared to those of Indium P-MOF. The lifetimes were in good agreement indicating that TCPP units are part of the backbone of mixed-ligand MOFs.

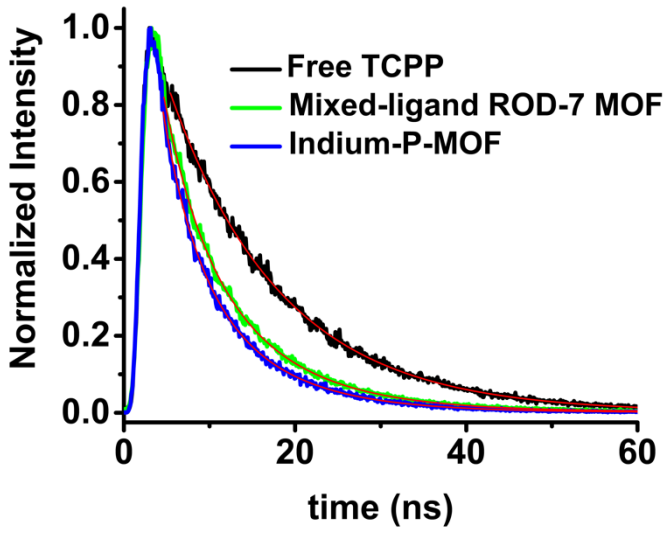

Figure S19. Time resolved emission decay profiles of TCPP in solution (black), TCPP in mixed-ligand ROD-7 MOF (red), TCPP in Indium P-MOF (blue)

Table S15. Lifetime data for free TCPP, mixed-ligand ROD-7 MOF, Indium P-MOF

	τ_{TCPP} (ns)
Free TCPP	13.18
Mixed-ligand ROD-7 MOF	10.65
Indium P-MOF	10.24

NU-902 is a TCPP-based MOF that is isostructural with NU-901.[43] Lifetimes of TCPP units in mixed-ligand NU-901 MOFs were compared to those of NU-902. The lifetimes were in good agreement indicating that TCPP units are part of the backbone of mixed-ligand MOFs.

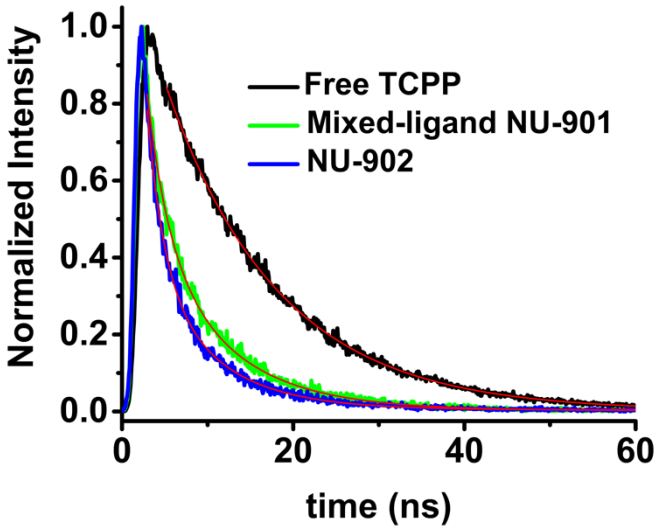

Figure S20. Time resolved emission decay profiles of TCPP in solution (black), TCPP in mixed-ligand NU-901 MOF (red), TCPP in NU-902 MOF (blue)

Table S16. Lifetime data for free TCPP, mixed-ligand NU-901 MOF, NU-902

	τ_{TCPP} (ns)
Free TCPP	13.18
Mixed-ligand NU-901 MOF	9.31
Indium P-MOF	9.03

PCN-222 is a TCPP-based MOF that is isostructural with NU-1000.[44] Lifetimes of TCPP units in mixed-ligand NU-1000 MOFs were compared to those of PCN-222. The lifetimes were in good agreement indicating that TCPP units are part of the backbone of mixed-ligand MOFs.

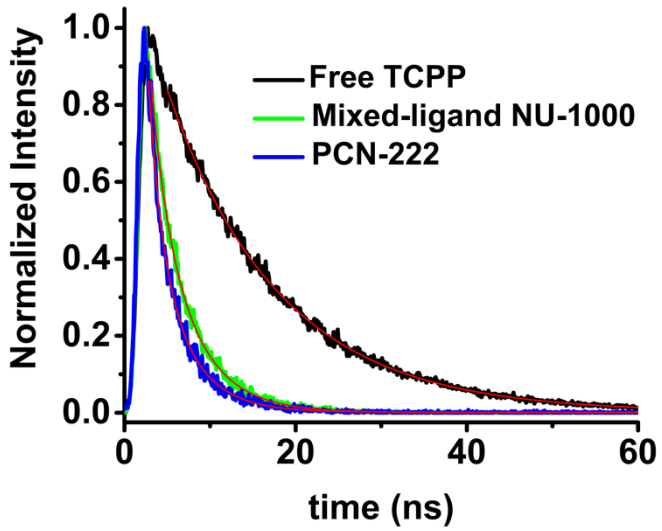

Figure S21. Time resolved emission decay profiles of TCPP in solution (black), TCPP in mixed-ligand NU-1000 MOF (red), TCPP in PCN-222 MOF (blue)

Table S17. Lifetime data for free TCPP, mixed-ligand NU-901 MOF, NU-902

	τ_{TCPP} (ns)
Free TCPP	13.18
Mixed-ligand NU-1000 MOF	8.56
PCN-222	8.40

2.6.8 Spectral overlap integrals

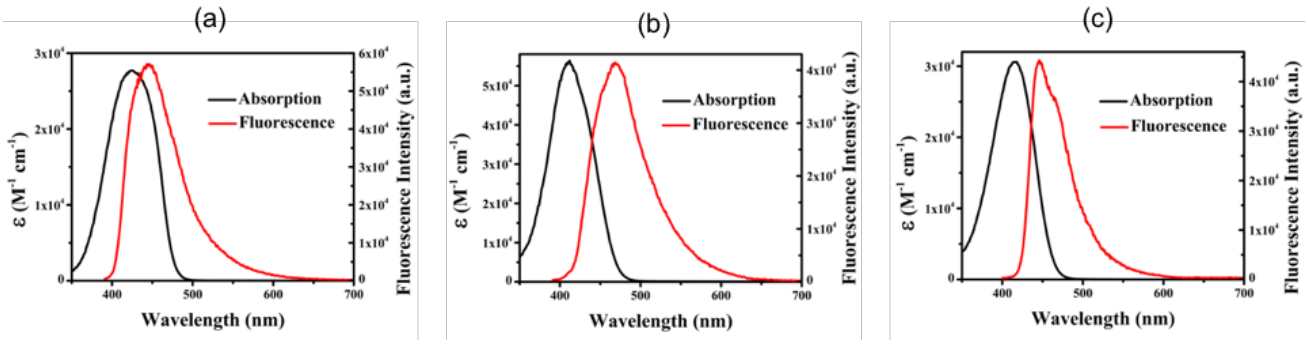

Figure S22. Spectral overlap between the absorption spectrum and emission spectrum of (a) ROD-7, (b) NU-901, and (c) NU-1000.

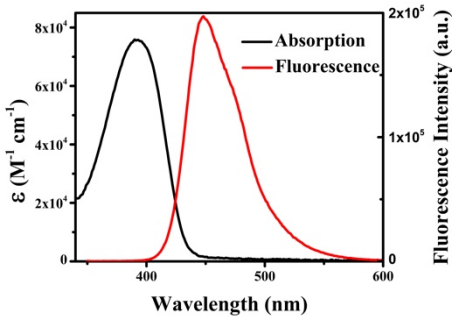

Figure S23. Spectral overlap between the absorption spectrum and emission spectrum of TBAPy.

Table S18. J integrals of MOFs and TBAPy solution

	J (nm^4 $M^{-1}cm^{-1}$)
ROD-7	5.41×10^{14}
NU-901	3.79×10^{14}
NU-1000	2.57×10^{14}
TBAPy	1.15×10^{14}

2.7 References

(1) Mirkovic, T.; Ostroumov, E. E.; Anna, J. M.; van Grondelle, R.; Govindjee; Scholes, G. D. Light Absorption and Energy Transfer in the Antenna Complexes of Photosynthetic Organisms. *Chem. Rev.* **2017**, *117* (2), 249–293. https://doi.org/10.1021/acs.chemrev.6b00002.

(2) van Grondelle, R.; Novoderezhkin, V. I. Energy Transfer in Photosynthesis: Experimental Insights and Quantitative Models. *Phys Chem Chem Phys* **2006**, *8* (7), 793–807. https://doi.org/10.1039/b514032c.

(3) Lakowicz, J. R. *Principles of Fluorescence Spectroscopy*, 3rd Edition.; Lakowicz, J. R., Ed.; Springer, Boston, MA, 2006. https://doi.org/https://doi.org/10.1007/978-0-387-46312-4.

(4) Stock, N.; Biswas, S. Synthesis of Metal-Organic Frameworks (MOFs): Routes to Various MOF Topologies, Morphologies, and Composites. *Chem. Rev.* **2012**, *112* (2), 933–969. https://doi.org/10.1021/cr200304e.

(5) Shuai, Y.; Liang, F.; Kecheng, W.; Jiandong, P.; Matheiu, B.; Christina, L.; Yujia, S.; Junsheng, Q.; Xinyu, Y.; Peng, Z.; et al. Stable Metal–Organic Frameworks: Design, Synthesis, and Applications. *Adv. Mater. 0* (0), 1704303. https://doi.org/10.1002/adma.201704303.

(6) Shaikh, S. M.; Usov, P. M.; Zhu, J.; Cai, M.; Alatis, J.; Morris, A. J. Synthesis and Defect Characterization of Phase-Pure Zr-MOFs Based on Meso-Tetracarboxyphenylporphyrin. *Inorg. Chem.* **2019**, *58* (8), 5145–5153. https://doi.org/10.1021/acs.inorgchem.9b00200.

(7) Lin, J.; Hu, X.; Zhang, P.; Van Rynbach, A.; Beratan, D. N.; Kent, C. A.; Mehl, B. P.; Papanikolas, J. M.; Meyer, T. J.; Lin, W.; et al. Triplet Excitation Energy Dynamics in

Metal-Organic Frameworks. *J. Phys. Chem. C* **2013**, *117* (43), 22250–22259. https://doi.org/10.1021/jp401515r.

(8) Lee, C. Y.; Farha, O. K.; Hong, B. J.; Sarjeant, A. a; Nguyen, S. T.; Hupp, J.; Hupp, J. T. Strut-to-Strut Energy Transfer in Bodipy and Porphyrin-Based MOFs Light-Harvesting Metal-Organic Frameworks (MOFs): Effi- Cient Strut-to-Strut Energy Transfer in Bodipy and Porphyrin- Based MOFs. *Synthesis (Stuttg)*. **2011**, 15858–15861.

(9) So, M. C.; Wiederrecht, G. P.; Mondloch, J. E.; Hupp, J. T.; Farha, O. K. Metal-Organic Framework Materials for Light-Harvesting and Energy Transfer. *Chem. Commun.* **2015**, *51* (17), 3501–3510. https://doi.org/10.1039/C4CC09596K.

(10) Kent, C. A.; Mehl, B. P.; Ma, L.; Papanikolas, J. M.; Meyer, T. J.; Lin, W. Energy Transfer Dynamics in Metal-Organic Frameworks. *J. Am. Chem. Soc.* **2010**, *132* (37), 12767–12769. https://doi.org/10.1021/ja102804s.

(11) Zhu, J.; Shaikh, S.; Mayhall, N. J.; Morris, A. J. Energy Transfer in Metal-Organic Frameworks. In *Elaboration and Applications of Metal-Organic Frameworks*; Series on Chemistry, Energy and the Environment; WORLD SCIENTIFIC, 2017; Vol. Volume 2, pp 581–654. https://doi.org/doi:10.1142/9789813226739_0014.

(12) Shaikh, S. M.; Chakraborty, A.; Alatis, J.; Cai, M.; Danilov, E.; Morris, A. J. Light Harvesting and Energy Transfer in a Porphyrin-Based Metal Organic Framework. *Faraday Discuss.* **2019**, *216* (0), 174–190. https://doi.org/10.1039/C8FD00194D.

(13) Birks, J. B.; Christophorou, L. G. Excimer Fluorescence Spectra of Pyrene Derivatives. *Spectrochim. Acta* **1963**, *19* (2), 401–410. https://doi.org/https://doi.org/10.1016/0371-1951(63)80051-X.

(14) Kashida, H.; Kawai, H.; Azuma, H.; Araki, Y.; Wada, T.; Asanuma, H. Quantitative

Analyses of Förster Resonance Energy Transfer between Identical Pyrene Chromophores (Homo-FRET) In DNA Scaffolds. *ChemPhotoChem* **2020**, *n/a* (n/a). https://doi.org/https://doi.org/10.1002/cptc.202000199.

(15) Porcu, P.; Vonlanthen, M.; Ruiu, A.; González-Méndez, I.; Rivera, E. Energy Transfer in Dendritic Systems Having Pyrene Peripheral Groups as Donors and Different Acceptor Groups. *Polymers* . 2018. https://doi.org/10.3390/polym10101062.

(16) Zaragoza-Galán, G.; Fowler, M.; Rein, R.; Solladié, N.; Duhamel, J.; Rivera, E. Fluorescence Resonance Energy Transfer in Partially and Fully Labeled Pyrene Dendronized Porphyrins Studied with Model Free Analysis. *J. Phys. Chem. C* **2014**, *118* (16), 8280–8294. https://doi.org/10.1021/jp501445n.

(17) Rojas-Montoya, S. M.; Vonlanthen, M.; Porcu, P.; Flores-Rojas, G.; Ruiu, A.; Morales-Morales, D.; Rivera, E. Synthesis and Photophysical Properties of Novel Pyrene–Metalloporphyrin Dendritic Systems. *Dalt. Trans.* **2019**, *48* (28), 10435–10447. https://doi.org/10.1039/C9DT00855A.

(18) Park, K. C.; Seo, C.; Gupta, G.; Kim, J.; Lee, C. Y. Efficient Energy Transfer (EnT) in Pyrene- and Porphyrin-Based Mixed-Ligand Metal–Organic Frameworks. *ACS Appl. Mater. Interfaces* **2017**, *9* (44), 38670–38677. https://doi.org/10.1021/acsami.7b14135.

(19) Stylianou, K. C.; Heck, R.; Chong, S. Y.; Bacsa, J.; Jones, J. T. A.; Khimyak, Y. Z.; Bradshaw, D.; Rosseinsky, M. J. A Guest-Responsive Fluorescent 3D Microporous Metal−Organic Framework Derived from a Long-Lifetime Pyrene Core. *J. Am. Chem. Soc.* **2010**, *132* (12), 4119–4130. https://doi.org/10.1021/ja906041f.

(20) Mondloch, J. E.; Bury, W.; Fairen-Jimenez, D.; Kwon, S.; DeMarco, E. J.; Weston, M. H.; Sarjeant, A. A.; Nguyen, S. T.; Stair, P. C.; Snurr, R. Q.; et al. Vapor-Phase Metalation by

Atomic Layer Deposition in a Metal–Organic Framework. *J. Am. Chem. Soc.* **2013**, *135* (28), 10294–10297. https://doi.org/10.1021/ja4050828.

(21) Kung, C.-W.; Wang, T. C.; Mondloch, J. E.; Fairen-Jimenez, D.; Gardner, D. M.; Bury, W.; Klingsporn, J. M.; Barnes, J. C.; Van Duyne, R.; Stoddart, J. F.; et al. Metal–Organic Framework Thin Films Composed of Free-Standing Acicular Nanorods Exhibiting Reversible Electrochromism. *Chem. Mater.* **2013**, *25* (24), 5012–5017. https://doi.org/10.1021/cm403726v.

(22) Renger, T. Theory of Excitation Energy Transfer: From Structure to Function. *Photosynth. Res.* **2009**, *102* (2), 471–485. https://doi.org/10.1007/s11120-009-9472-9.

(23) Kistler, K. A.; Spano, F. C.; Matsika, S. A Benchmark of Excitonic Couplings Derived from Atomic Transition Charges. *J. Phys. Chem. B* **2013**, *117* (7), 2032–2044. https://doi.org/10.1021/jp310603z.

(24) Dommett, M.; Rivera, M.; Smith, M. T. H.; Crespo-Otero, R. Molecular and Crystalline Requirements for Solid State Fluorescence Exploiting Excited State Intramolecular Proton Transfer. *J. Mater. Chem. C* **2020**, *8* (7), 2558–2568. https://doi.org/10.1039/C9TC05717J.

(25) Son, H.-J.; Jin, S.; Patwardhan, S.; Wezenberg, S. J.; Jeong, N. C.; So, M.; Wilmer, C. E.; Sarjeant, A. A.; Schatz, G. C.; Snurr, R. Q.; et al. Light-Harvesting and Ultrafast Energy Migration in Porphyrin-Based Metal–Organic Frameworks. *J. Am. Chem. Soc.* **2013**, *135* (2), 862–869. https://doi.org/10.1021/ja310596a.

(26) Zhang, Q.; Zhang, C.; Cao, L.; Wang, Z.; An, B.; Lin, Z.; Huang, R.; Zhang, Z.; Wang, C.; Lin, W. F??Rster Energy Transport in Metal-Organic Frameworks Is beyond Step-by-Step Hopping. *J. Am. Chem. Soc.* **2016**, *138* (16), 5308–5315.

https://doi.org/10.1021/jacs.6b01345.

(27) Becke, A. D. Density-functional Thermochemistry. III. The Role of Exact Exchange. *J. Chem. Phys.* **1993**, *98* (7), 5648–5652. https://doi.org/10.1063/1.464913.

(28) Becke, A. D. A New Mixing of Hartree–Fock and Local Density-functional Theories. *J. Chem. Phys.* **1993**, *98* (2), 1372–1377. https://doi.org/10.1063/1.464304.

(29) Dunning, T. H. Gaussian Basis Sets for Use in Correlated Molecular Calculations. I. The Atoms Boron through Neon and Hydrogen. *J. Chem. Phys.* **1989**, *90* (2), 1007–1023. https://doi.org/10.1063/1.456153.

(30) Stratmann, R. E.; Scuseria, G. E.; Frisch, M. J. An Efficient Implementation of Time-Dependent Density-Functional Theory for the Calculation of Excitation Energies of Large Molecules. *J. Chem. Phys.* **1998**, *109* (19), 8218–8224. https://doi.org/10.1063/1.477483.

(31) Bauernschmitt, R.; Ahlrichs, R. Treatment of Electronic Excitations within the Adiabatic Approximation of Time Dependent Density Functional Theory. *Chem. Phys. Lett.* **1996**, *256* (4), 454–464. https://doi.org/https://doi.org/10.1016/0009-2614(96)00440-X.

(32) Casida, M. E.; Jamorski, C.; Casida, K. C.; Salahub, D. R. Molecular Excitation Energies to High-Lying Bound States from Time-Dependent Density-Functional Response Theory: Characterization and Correction of the Time-Dependent Local Density Approximation Ionization Threshold. *J. Chem. Phys.* **1998**, *108* (11), 4439–4449. https://doi.org/10.1063/1.475855.

(33) M. J. Frisch, G. W. Trucks, H. B. Schlegel, G. E. S.; M. A. Robb, J. R. Cheeseman, G. Scalmani, V. Barone, B. M.; G. A. Petersson, H. Nakatsuji, M. Caricato, X. Li, H. P. H.; A. F. Izmaylov, J. Bloino, G. Zheng, J. L. Sonnenberg, M. H.; M. Ehara, K. Toyota, R. Fukuda, J. Hasegawa, M. Ishida, T. N.; Y. Honda, O. Kitao, H. Nakai, T. Vreven, J. A.

Montgomery, J.; J. E. Peralta, F. Ogliaro, M. Bearpark, J. J. Heyd, E. B.; K. N. Kudin, V. N. Staroverov, T. Keith, R. Kobayashi, J. N.; K. Raghavachari, A. Rendell, J. C. Burant, S. S. Iyengar, J. T.; M. Cossi, N. Rega, J. M. Millam, M. Klene, J. E. Knox, J. B. C.; et al. Gaussian 09, Revision E.01. Gaussian, Inc.: Wallingford CT 2013.

(34) Schmidt, J. R.; Polik, W. F. WebMo Enterprise, Version 20.0. WebMO LLC: Holland: MI, USA 2020.

(35) Li, X.; Yu, J.; Gosztola, D. J.; Fry, H. C.; Deria, P. Wavelength-Dependent Energy and Charge Transfer in MOF: A Step toward Artificial Porous Light-Harvesting System. *J. Am. Chem. Soc.* **2019**, *141* (42), 16849–16857. https://doi.org/10.1021/jacs.9b08078.

(36) Yu, J.; Park, J.; Van Wyk, A.; Rumbles, G.; Deria, P. Excited-State Electronic Properties in Zr-Based Metal–Organic Frameworks as a Function of a Topological Network. *J. Am. Chem. Soc.* **2018**, *140* (33), 10488–10496. https://doi.org/10.1021/jacs.8b04980.

(37) Deria, P.; Yu, J.; Smith, T.; Balaraman, R. P. Ground-State versus Excited-State Interchromophoric Interaction: Topology Dependent Excimer Contribution in Metal–Organic Framework Photophysics. *J. Am. Chem. Soc.* **2017**, *139* (16), 5973–5983. https://doi.org/10.1021/jacs.7b02188.

(38) Yu, J.; Anderson, R.; Li, X.; Xu, W.; Goswami, S.; Rajasree, S. S.; Maindan, K.; Gómez-Gualdrón, D. A.; Deria, P. Improving Energy Transfer within Metal–Organic Frameworks by Aligning Linker Transition Dipoles along the Framework Axis. *J. Am. Chem. Soc.* **2020**, *142* (25), 11192–11202. https://doi.org/10.1021/jacs.0c03949.

(39) Majoul I., Jia Y., D. R. *Practical Fluorescence Resonance Energy Transfer or Molecular Nanobioscopy of Living Cells*; Springer, Boston, MA, 2006.

(40) Conroy, E. M.; Li, J. J.; Kim, H.; Algar, W. R. Self-Quenching, Dimerization, and Homo-

FRET in Hetero-FRET Assemblies with Quantum Dot Donors and Multiple Dye Acceptors. *J. Phys. Chem. C* **2016**, *120* (31), 17817–17828. https://doi.org/10.1021/acs.jpcc.6b05886.

(41) Shirai, S.; Inagaki, S. Ab Initio Study on the Excited States of Pyrene and Its Derivatives Using Multi-Reference Perturbation Theory Methods. *RSC Adv.* **2020**, *10* (22), 12988–12998. https://doi.org/10.1039/C9RA10483F.

(42) Rhauderwiek, T.; Waitschat, S.; Wuttke, S.; Reinsch, H.; Bein, T.; Stock, N. Nanoscale Synthesis of Two Porphyrin-Based MOFs with Gallium and Indium. *Inorg. Chem.* **2016**, *55* (11), 5312–5319. https://doi.org/10.1021/acs.inorgchem.6b00221.

(43) Deria, P.; Gómez-Gualdrón, D. A.; Hod, I.; Snurr, R. Q.; Hupp, J. T.; Farha, O. K. Framework-Topology-Dependent Catalytic Activity of Zirconium-Based (Porphinato)Zinc(II) MOFs. *J. Am. Chem. Soc.* **2016**, *138* (43), 14449–14457. https://doi.org/10.1021/jacs.6b09113.

(44) Feng, D.; Gu, Z.-Y.; Li, J.-R.; Jiang, H.-L.; Wei, Z.; Zhou, H.-C. Zirconium-Metalloporphyrin PCN-222: Mesoporous Metal-Organic Frameworks with Ultrahigh Stability as Biomimetic Catalysts. *Angew. Chemie Int. Ed.* **2012**, *51* (41), 10307–10310. https://doi.org/10.1002/anie.201204475.

3. Light Harvesting and Energy Transfer in a Porphyrin-based Metal Organic Framework

This chapter is reproduced from the following reference: ***Faraday Discuss***., 2019, 216, 174-190. Reproduced by permission of The Royal Society of Chemistry.

3.1 Introduction

One of the most important components of artificial photosynthesis assemblies are the antennae, which collect solar energy and direct it towards the reaction centers. A multi-chromophoric array with an energy cascade can direct sequential photoexcited energy flow and perform the function of light harvesting antenna assemblies.[1] Multi-porphyrin arrays have been studied extensively with the aim of constructing antenna assemblies that mimic natural photosynthetic systems in terms of the efficiency of excitation energy transfer (EET). Subtle changes in structural parameters, such as connectivity, distance, and orientation between porphyrin units in the array can have strong implications on the nature of interchromophoric interactions, and the rates and efficiencies of EET.[2] Highlighted by highly-ordered crystal structures and synthetic tunability via crystal engineering, metal organic frameworks (MOFs) allow for precise control of distances and angles between chromophores and their alignment by careful selection of organic ligands and metal nodes.[3–6] Porphyrin based MOFs are therefore ideal candidates to study EET as a function of structural parameters. Such studies will aid in the design of porphyrin-based architectures that are conducive for energy transfer. Before examining the role of MOF structure in EET, it is necessary to first understand the mechanistic aspects of EET and the factors that determine the efficiency of EET in porphyrin-based MOFs. To address these issues, we probed the energy transfer characteristics of PCN-223(free-base), a Zr-MOF based on meso-tetrakis(4-carboxyphenyl)porphyrin (TCPP).

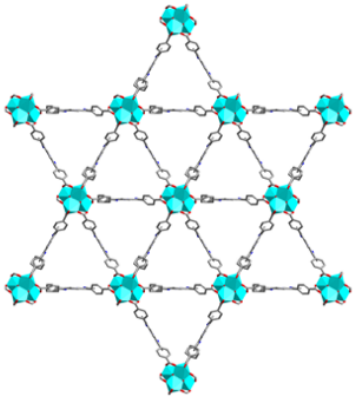

Figure 1. View of PCN-223 along the c axis with uniform triangular 1D channels

Zirconium-based MOFs containing porphyrin ligand have been studied extensively due to their exceptional chemical stability under harsh experimental conditions and their ability to exhibit a variety of functionalities like catalysis, light harvesting, gas-storage and sensing.[4,7–12] PCN-223, in particular, has a very unique structure (Figure 1).[10] It consists of unprecedented D_{6h} symmetric $[Zr_6O_4(OH)_4]^{12+}$ nodes connected to 12 TCPP linkers, representing the first (4,12)-connected MOF with the "shp" topology. The closely-packed structure of PCN-223 supports a high density of chromophores that can simultaneously absorb light and participate in the energy transfer process. The closest distance between two porphyrin struts is 10.71 Å (see Supplementary Information, Section 3.5.9). PCN-223 also manifests a small porphyrin-porphyrin torsional angle (~55°) that facilitates interchromophoric electronic coupling between TCPP units.[13] Based on these merits, PCN-223 qualifies to serve as a model system to explore EET mechanism in porphyrin-based MOFs.

Herein, we present synthesis, structural, and photophysical characterization of PCN-223 MOF constructed from free base TCPP ligand. The effects of pH and temperature on the excited state properties of PCN-223 were investigated and compared with those of ligand. The efficiency of

EET in the MOF was investigated by studying the pH-dependence of fluorescence intensity. The study revealed the presence of static quenching both in ligand and MOF. Fluorescence quenching in MOF was observed to be greatly enhanced as compared to free ligand. The temperature dependence of the fluorescence decay rates was investigated to gain an understanding of the mechanistic aspects of EET in the MOF. The results indicate an incoherent, step-by-step hopping mechanism for EET. A Förster energy transfer model was employed to estimate the rate of energy migration (k_{EET}) in PCN-223. Nanosecond transient absorption spectroscopy was employed to characterize the non-emissive triplet state of PCN-223. The results revealed the presence of a long-lived triplet state (extending beyond 200 μs) that exhibits the characteristic features of a TCPP-based triplet state. Furthermore, femtosecond transient absorption spectroscopy was employed to characterize the ultrafast photophysical processes taking place in TCPP and PCN-223. Kinetic analysis of the ultrafast data of TCPP and PCN-223 showed the presence of three distinct time components that correspond to: (a) solvent-induced vibrational reorganization of excitation energy, (b) vibrational cooling, and (c) fluorescence. Our study revealed the presence of efficient, long-distance energy transfer (100 Å (1D), 141 Å (2D), and 173 Å (3D)) in PCN-223 MOF.

3.2 Experimental section

Materials: Meso-tetra(4-carboxyphenyl)porphyrin (>97%) was purchased from Frontier Scientific and was used without further purification. Zirconium chloride (anhydrous, ≥99.5%) was purchased from Sigma-Aldrich. Dimethylformamide (DMF, spectrophotometric grade, ≥99.9%) was purchased from Fisher chemical. Propionic acid (PA, 99%). were purchased from Alfa Aesar.

Synthesis of PCN-223(free-base): 10 mg of H_2TCPP (1.3×10^{-5} mol) and 7 mg of $ZrCl_4$ (3×10^{-5} mol) were added to 10ml DMF and ultrasonically dissolved in a 6-dram vial. 2 ml propionic acid was added to the vial and the vial was sonicated for 15 minutes to get a homogeneous reaction

mixture. The vial was placed in an oven set at 120 ºC for 16 hours. After allowing them to cool down to room temperature, the resultant MOF powder was collected by centrifugation. It was washed 3 times with DMF and then soaked in ethanol for 3 days with fresh ethanol replacement every day. The MOFs were dried at room temperature and then activated by heating at 100 °C under vacuum.

Powder X-ray diffraction and Scanning electron microscopy (PXRD): A 600 W Rigaku MiniFlex powder diffractometer with a CuKα (0.15418 nm) radiation source was used, with a sweeping range of 2–25° in continuous scanning mode. PXRD traces were collected in 0.05° increments at a scanning rate of 0.2°/min.

Scanning electron microscopy (SEM): SEM samples were prepared by suspending MOF powders in ethanol with sonication. The resulting suspensions were drop-casted on precut glass slides. After drying, the glass slides were mounted on SEM sample pegs with the help of double-sided copper tape. The sides of the glass slides and the platform of sample peg were coated with conductive carbon paint purchased from Electron Microscopy Sciences. A LEO (Zeiss) 1550 field-emission scanning electron microscope, equipped with an in-lens detector, operating at 5.0 kV was used to obtain high-resolution images of the MOF particles.

Thermogravimetric Analysis (TGA): A Q-series thermogravimetric analyzer from TA Instruments was used to assess the thermal stability of MOFs. Samples weighing ~3-5 mg were placed on a platinum pan and heated under air at a rate of 5 °C/min over the temperature range of 25−800 °C.

Gas adsorption isotherms: The N_2 adsorption measurements were conducted using a Micromeritics 3Flex instrument. A 6 mm large bulb sample cell was used to hold the samples and was degassed under vacuum at a temperature of 100 °C for 24 h. The surface area of the MOFs

was determined from the N_2 adsorption isotherms at 77 K by fitting the adsorption data within the 0.05−0.3 P/P_0 pressure range to the BET equation.

Diffuse absorption spectroscopy: The diffuse absorption spectra of TCPP and PCN-223 were obtained using an Agilent Technologies 8453 UV-Vis diode array spectrophotometer (1 nm resolution) where the sample compartment was replaced with an integration sphere. The powder samples were diluted by mixing with $BaSO_4$.

Steady-state emission spectroscopy and time-resolved emission lifetimes: The steady-state emission spectra were obtained using a QuantaMaster Model QM-200-4E emission spectrophotometer from Photon Technology, Inc. (PTI). The excitation light source was a 75 W Xe arc lamp (Newport). The detector was a thermoelectrically cooled Hamamatsu 1527 photomultiplier tube (PMT). Emission traces were analyzed using Origin 9.0. Time-resolved fluorescence lifetimes were obtained via the time-correlated single photon counting technique (TCSPC) with the same QuantaMaster Model QM-200-4E emission spectrophotometer from Photon Technology, Inc. (PTI) equipped with a 415 nm LED and a Becker & Hickl GmbH PMH-100 PMT detector with time resolution of < 220 ps FWHM. Florescence lifetime decays were analyzed with the help of Origin 9.0.

Nanosecond transient absorption spectroscopy:

Transient absorption difference spectra and kinetic traces were collected with LP 980 laser flash photolysis system (Edinburgh Instruments) equipped with a PMT detector (R928, Hamamatsu). The excitation source was 532 nm Nd:YAG laser (Spectra-Physics-Quanta-Ray Lab) operating at 1 Hz. The laser system was also equipped with an image intensified CCD (ICCD) camera detector. Triplet lifetime decays were analyzed with the help of Origin 9.0.

Femtosecond transient absorption spectroscopy:

Time-resolved transient absorption measurements were performed at the Imaging and Kinetic Spectroscopy (IMAKS) Laboratory, Department of Chemistry, NCSU (North Carolina State University). A mode-locked Ti:sapphire laser (Coherent Libra, 800 nm, 1 kHz repetition rate, 100 fs, 4 mJ/pulse) was used as the main light source. The output from the laser was split into the pump beam and probe beam. The pump beam was directed into the parametric amplifier (Coherent OPerA Solo) to generate the 400nm excitation. The probe beam was delayed in a 6ns optical delay stage and then focused into a CaF_2 crystal for white light continuum generation between 340 nm and 750 nm. The pump beam was then focused on the sample (into an 800 μm spot) and overlapped with the probe beam (~200 μm). The relative polarizations of the pump beam and the probe beam were set at the magic angle of 54.7º. The ground state absorption spectra of the samples were measured before and after the measurements to ensure that there is no degradation. Transient kinetics were analyzed using the fitting routines available in Origin 9.0.

3.3 Results and Discussion

Synthesis of PCN-223(free-base) was achieved by following a procedure that gives highly crystalline, phase-pure powder. Briefly, 3×10^{-5} mol of $ZrCl_4$ and 1.3×10^{-5} mol of TCPP were dissolved in 10 mL DMF along with 2.5×10^{-2} mol of propionic acid as the modulator. The mixture was sonicated for 15 minutes then the vial was placed in an oven and heated at 120 ºC for 16 h. The resulting MOF powders were characterized by PXRD (Figure 2a) and SEM (Figure 2b). Comparison of the PXRD pattern obtained from synthesis to the simulated pattern from single crystal XRD data indicated high phase purity. The SEM image shows small bean-shaped particles that are characteristic of PCN-223 MOF. All MOF particles are morphologically identical, which further confirms the high phase purity. In addition, the effective molecular weight of as-prepared PCN-223 sample was determined by TGA analysis (see Supplementary Information, Section

3.5.1). The BET surface area of the MOF obtained from gas adsorption data agrees well with the literature (see Supplementary Information, Section 3.5.2).[10]

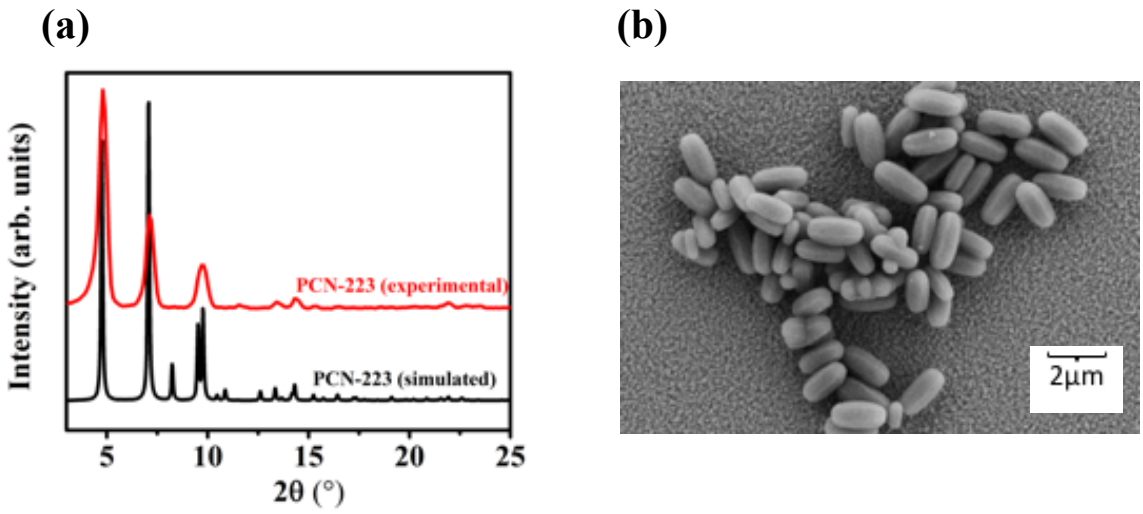

Figure 2. (a) PXRD characterization of PCN-223. (b) SEM image of PCN-223.

To examine how the ground and excited-state properties of TCPP are affected upon coordination into the MOF structure, the electronic absorption spectra of TCPP and PCN-223 were compared (Figure 3). The absorption spectrum of TCPP consists of the Soret band ($S_0 \rightarrow S_2$ transition) around 415 nm in the near UV region and four weak Q bands ($S_0 \rightarrow S_1$ transition) in the visible region (between 500 to 700 nm). PCN-223 displays an absorption spectrum similar to that of TCPP with a sharp Soret band and four Q bands. The Soret band of PCN-223 is blue shifted by 13 nm relative to the ligand, which is attributed to structural changes that TCPP undergoes as it is incorporated in the MOF (see Supplementary Information, Section 3.5.4). Twisting of phenyl rings and changes in the macrocyclic ring planarity of TCPP may be responsible for increasing the energy gap between the ground state and second excited state (S_0-S_2), which causes the blue shift. The peak positions and intensities of Q bands of PCN-223 match those of TCPP, suggesting that the energy gap between ground state and first excited state of TCPP is relatively unaffected upon incorporation into the MOF.

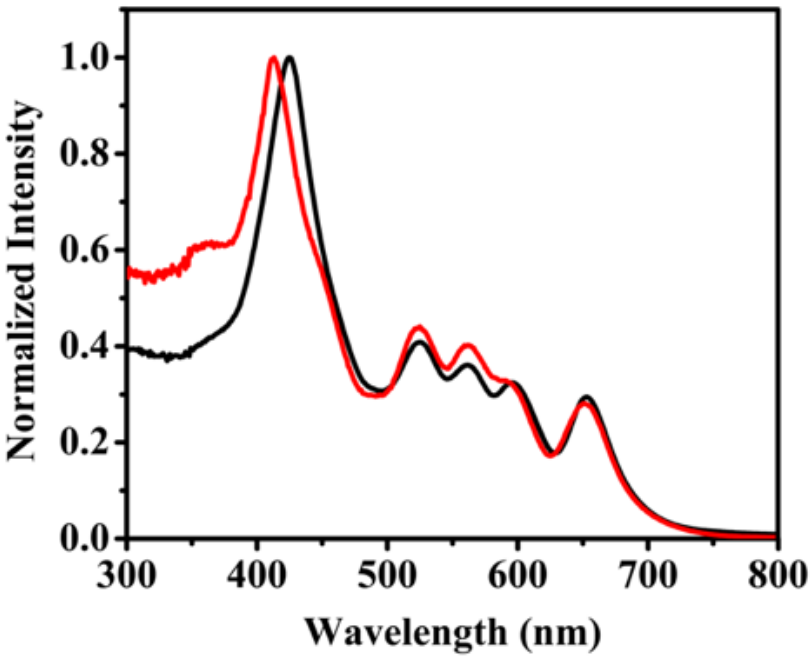

Figure 3. Diffuse absorption spectra of TCPP (black) and PCN-223 (red)

The acid-base properties of porphyrins in aqueous solutions provide important information about their reactivity, aromaticity, tautomerization mechanisms and stereochemistry.[14–16] The central macrocycle of porphyrins exhibits an amphoteric behavior and can exist in either neutral (free-base), N-protonated, or deprotonated form (Figure 4). Mono-protonation of the free-base form induces nonplanar distortions in the porphyrin structure, which makes the second protonation more favorable.[17,18] The first protonation step is immediately followed by the second step, producing the porphyrin dication, while the monoprotonated species is present in very small amounts at any given time. To determine the pK_a values corresponding to the successive protonation steps, we titrated an aqueous solution of TCPP (10^{-6} M) against 0.01 M NaOH solution. A dilute suspension of PCN-223 in water was also titrated against 0.01 M NaOH solution to determine the pK_a values for TCPP incorporated in the MOF. The pK_a values for TCPP and PCN-223 are reported in Figure 4.

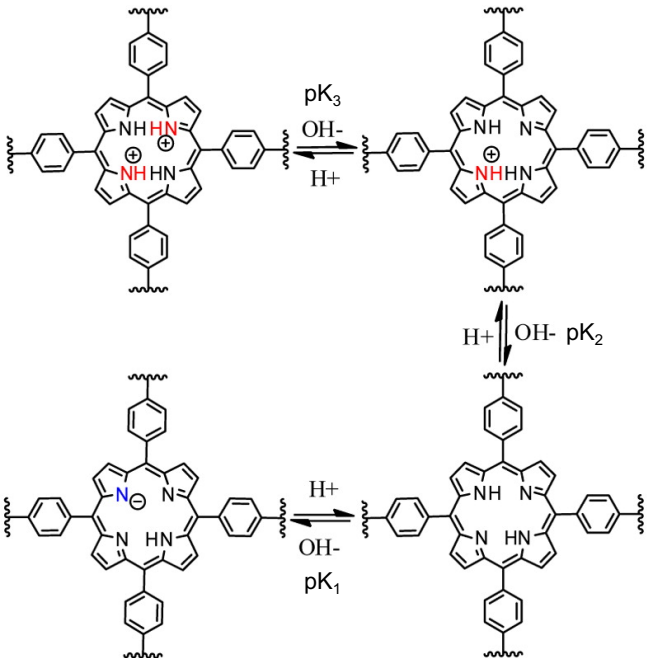

Figure 4. Protonation and deprotonation processes of TCPP in acidic and basic media.[8] pK_1, pK_2 and pK_3 represent the pK_a values associated with these processes. The first and second protonation processes are almost indistinguishable, such that $pK_2 \approx pK_3$. For TCPP, $pK_2 \approx pK_3 = 3.2$, and for PCN-223 $pK_2 \approx pK_3 = 3.75$ (see Supplementary Information, Section 3.5.3).

Varying solution pH can shift the protonation-deprotonation equilibrium of the macrocycle in favor of a particular form, which can greatly influence the photophysics of the porphyrin molecule.[18] Non-planarity induced in the porphyrin structure due to protonation of the nitrogen atoms breaks up their π-electron conjugated double-bond system. Loss of conjugation promotes non-radiative relaxation of the excited state that results in significant fluorescence quenching and short fluorescence lifetimes.[19] To investigate the effects of pH variation on the fluorescence properties of TCPP and PCN-223, their steady-state emission spectra were measured in an experimental pH range of 3.5 to 8.5 ($\lambda_{excitation}$ = 415 nm). Given that PCN-223 is stable in aqueous environments with pH values ranging from 0 to 10,[10] the experimental pH range is suitable for investigating the photophysics of the MOF without loss in crystallinity. The peak positions and

intensities of fluorescence spectra of TCPP and PCN-223 were found to be strongly correlated with pH of solution/suspension. For pH > 5.5, fluorescence spectra of TCPP and PCN-223 displayed a sharp band at 645 nm (Q(0,0) band) and a relatively weaker band at 720 nm (Q(0,1) band) (Figure 5a and 5b). Structural changes induced in the porphyrin macrocycle due to protonation of central nitrogen atoms cause the band at 645 nm to broaden and red shift by ~35 nm. As a result, for pH < 5.5 the fluorescence spectrum of TCPP and PCN-223 appears to be a single broad band centered at 680 nm (Figure 5c).

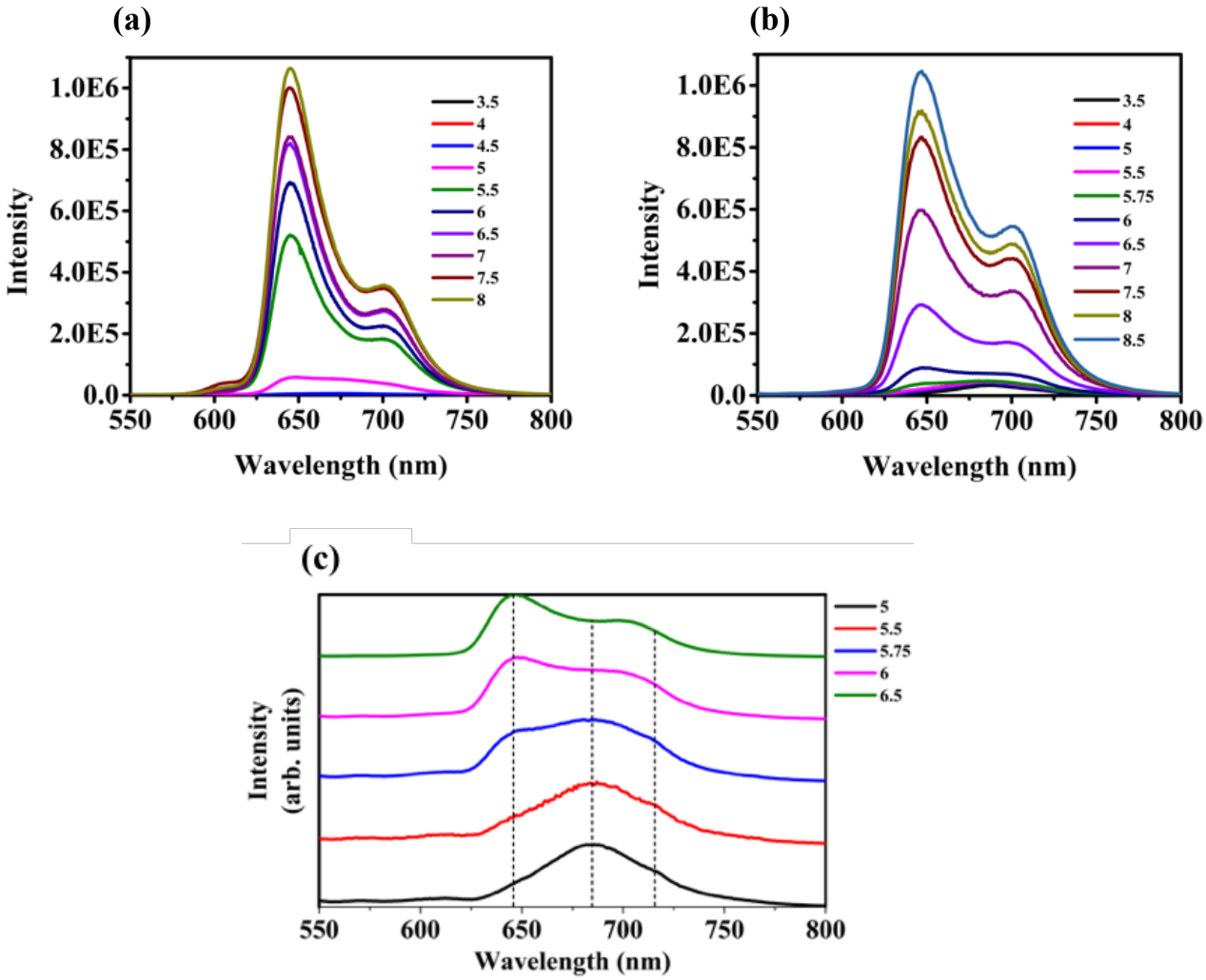

Figure 5. (a) Fluorescence spectra of TCPP in water (10^{-6}M) as a function of pH. (b) Fluorescence spectra of PCN-223 in water as a function of pH. (c) Spectral evolution of PCN-223 in the pH range of 5 to 6.5.

3.3.1 Fluorescence quenching in PCN-223

Due to the overlap between the absorption spectrum of N-protonated TCPP and the emission spectrum of neutral TCPP, N-protonated TCPP linkers can potentially act as energy traps and quench the fluorescence of neutral TCPP linkers via energy transfer (see Supplementary Information, Section 3.5.7). To confirm the presence of energy transfer between neutral TCPP and N-protonated TCPP units, a Stern-Volmer analysis was performed. The relationship between the quencher concentration and extent of quenching is provided by Stern-Volmer equation (eq. 1),

$$\frac{I_0}{I} = 1 + K_{SV}[Q] \quad (1)$$

where I_0 is the fluorescence intensity in the absence of quencher, I is the fluorescence intensity at a particular concentration of quencher, K_{SV} is the Stern-Volmer quenching constant, and [*Q*] is the quencher concentration. Figure 6 shows the modified Stern-Volmer plots for TCPP and PCN-223, where I_0/I is plotted against the ratio of N-protonated and neutral TCPP concentration (see Supplementary Information, Section 3.5.5).

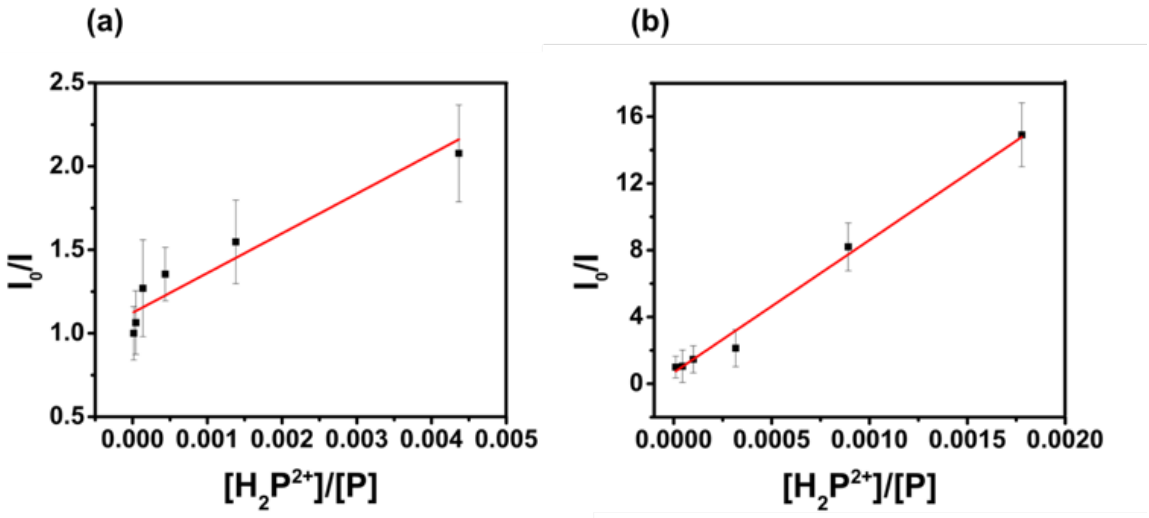

Figure 6. (**a**) Modified Stern-Volmer plot of TCPP in the pH range of 5.5 to 8. (**b**) Modified Stern-Volmer plot of PCN-223 in the pH range of 5.5 to 8.5.

Table 2. Stern-Volmer rate constant and quenching rate constants of TCPP and PCN-223

	K_{sv} (M^{-1})	k_Q ($M^{-1}s^{-1}$)
TCPP	237.68	2.71×10^{10}
PCN-223	7298.96	8.06×10^{11}

The quenching rate constant (k_Q) can be calculated by dividing K_{SV} by the fluorescence lifetime of donor in the absence of quencher (τ_0). K_{SV} and k_Q values of TCPP and PCN-223 are provided in Table 2. The quenching rate constant for PCN-223 is significantly larger than that for TCPP, which is attributed to energy migration from neutral TCPP linkers to N-protonated TCPP linkers. Although a dramatic decrease in fluorescence intensity of MOF was observed on lowering the pH, time-resolved fluorescence measurements revealed that the lifetime of the MOF was not quenched.

3.3.2 Energy transfer efficiency in PCN-223 MOF

Excitation energy transfer primarily occurs through two coupling mechanisms: Dexter exchange mechanism and Förster dipole-dipole mechanism.[4,26–30] The Dexter mechanism requires the presence of electronic communication between the donor and acceptor via orbital overlap.[31,32] Since orbital overlap between adjacent TCPP struts of PCN-223 is poor, the Dexter mechanism may not be suitable to describe energy transfer in this case.[20] The Förster mechanism (FRET), on the other hand, adequately describes the "through space" energy migration in PCN-223. The rate and efficiency of FRET is dependent on three physical parameters. These parameters are (1) the degree of overlap between donor emission spectrum and acceptor absorption spectrum, (2) relative geometric orientation of donor and acceptor, and (3) the separation distance between donor and acceptor units.[33] The FRET efficiency of porphyrin-based MOFs has been previously quantified

by performing fluorescence quenching experiments.[20,28,34] We performed a qualitative analysis of FRET efficiency by relating the extent of quenching (Φ_q) to the concentration of quencher (N-protonated TCPP). Φ_q is given by eq. 2,

$$\Phi_q = 1 - \frac{I_q}{I_0} \quad (2)$$

where I_q and I_0 are the fluorescence intensities of donor in the presence and absence of quencher.[35] Φ_q for TCPP and PCN-223 was estimated to be 93% and 51%, respectively, when 1% of the TCPP linkers are protonated (see Supplementary Information, Section 3.5.5). The significantly higher magnitude of Φ_q for the MOF complements the results of Stern-Volmer analysis in the previous section. The quenching observed in MOF can be considered as a combination of "self-quenching" and quenching via energy transfer from neutral TCPP linkers to N-protonated TCPP linkers.

The rate constant of energy transfer defined by the Förster model is given by eq. 3,

$$k_{EET} = \frac{1}{\tau_0}\left(\frac{R_0}{r}\right)^6 \quad (3)$$

where τ_0 is the lifetime of donor in the absence of acceptor, r is the donor-acceptor distance and R_0 is the Förster radius.[21] R_0 is defined as the distance at which the energy transfer efficiency is 50%, and is dependent on the fluorescence quantum yield of donor in the absence of acceptor (Φ_D) and the spectral overlap integral (J). R_0 is given by eq. 4,

$$R_0 = \left(\frac{9000(\ln 10)\kappa^2\,\Phi_D J}{128\pi^5 N_A n^4}\right)^{\frac{1}{6}} \quad (4)$$

where κ^2 is a geometric parameter that describes the relative orientation between the transition dipole moments of donor and acceptor, N_A is Avogadro's number, and n is the refractive index of the surrounding media. Based on the above equation, the Förster radius for PCN-223 was found to

be 54.5 Å ($J = 5.344 \times 10^{-14}$ $M^{-1}cm^3$, see Supplementary Information, Section 3.5.7 and 3.5.8).[36,37] The rate constant of energy transfer (k_{EET}) was estimated to be 1.9×10^{12} s^{-1}, which is broadly consistent with k_{EET} values reported by Son et al. for other porphyrin-based MOFs.[25] The total energy migration distance (R_{hop}) was obtained using eq. 5,

$$R_{hop} = \sqrt{m \frac{D_{RET}}{k_{EET}}} \quad (5)$$

where m is the dimensionality factor and D_{RET} is the diffusion coefficient of energy migration.[36–40] Long distance energy transfer corresponding to 100 Å for one-dimensional energy transfer, 141 Å for two-dimensional energy transfer, and 173 Å for three-dimensional energy transfer was estimated. Since very little information is available about D_{RET} values of porphyrin-based MOFs, we used the D_{RET} of meso-tetra(4-sulfonatophenyl) porphyrin (TPPS) nanotubes (95×10^{-6} m^2 s^{-1}) for calculating the energy migration distances.[36]

3.3.3 Temperature dependence of fluorescence lifetimes

The temperature dependence of the fluorescence decay rates (k_{obs}) of an emissive MOF can give insight into the mechanism of energy transfer.[20] At room temperature, there are various vibrational degrees of freedom that allow the excited state to fully relax between energy transfer events. However, at low temperatures (~77K) some of the vibrational degrees of freedom are frozen out. If the electronic interactions between the linkers in a MOF are very strong (strong coupling regime), then at low temperatures the rate of energy transfer can exceed that of vibrational relaxation. In such a scenario, the excitation energy can move as an exciton that is delocalized over the whole system.[1,21] The MOF should behave as an "aggregate" and the energy transfer process is termed as "coherent". In contrast, if the electronic interactions between the linkers in a MOF are weak (weak coupling regime), then vibrational relaxation dominates at all temperatures. In this

case, the excitation energy remains localized on a linker and energy is transferred via a step-by-step hopping mechanism. The MOF behaves as a "monomer" and the energy transfer process is termed as "incoherent".

To determine whether PCN-223 belongs to the strong coupling regime or the weak coupling regime, the temperature-dependence of the fluorescence decay kinetics of TCPP and PCN-223 was investigated.[22] The fluorescence decay rate constants (k_f) of TCPP and PCN-223 were obtained at temperatures ranging from 77K to 333K (Figure 7a and 7b). To plot the temperature dependence curves, k_f were fit to eq. 6,

$$k_f = k_0 + k_1 e^{-\Delta E/k_B T} \quad (6)$$

where k_0 is the temperature independent term and the Arrhenius term describes the temperature dependence of k_f.[23,24] The pre-exponential factor (k_1) and the activation energy required for transitioning from the ground state to the excited state (ΔE) were extracted from the fits (Table 1). The magnitudes of k_1 and ΔE are very similar for TCPP and PCN-223, suggesting that the temperature-dependent fluorescence behavior of the MOF is comparable to that of monomeric TCPP units. Based on this result, it was concluded that PCN-223 belongs to the weak coupling regime and an incoherent mechanism is proposed for EET in PCN-223.

Table 1. Experimental parameters associated with TCPP and PCN-223

	k_0 (s^{-1}) ($\times 10^7$)	k_1 (s^{-1}) ($\times 10^7$)	ΔE (J/molecule) ($\times 10^{-21}$)
TCPP	6.7 ± 0.1	4 ± 0.1	7.3 ± 0.1
PCN-223	6.4 ± 0.2	3.3 ± 0.6	8.3 ± 0.5

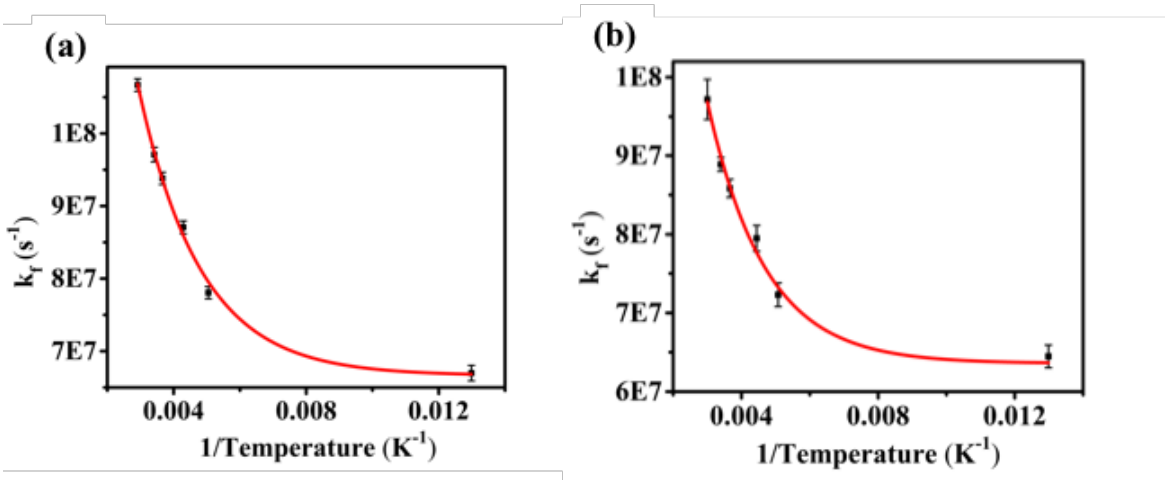

Figure 7. (a) Temperature dependence of k_{obs} of TCPP in MeOH-EtOH (3:1 v/v) mixture (pH ≈ 7). (b) Temperature dependence of k_{obs} of PCN-223 suspension (3:1 v/v) mixture (pH ≈ 7).

3.3.4 Nanosecond transient absorption spectroscopy

Thus far, we have investigated the singlet excited states of TCPP and PCN-223. Nanosecond transient absorption (nsTA) spectroscopy was used as an additional tool to get further insight into the excited state photophysics of TCPP and PCN-223. With the help of this technique, the triplet excited state of TCPP and PCN-223 were studied. Nanosecond transient absorption difference spectra were acquired for a TCPP solution and PCN-223 suspension in water at pH 8 (in the nanosecond to microsecond time domain, Figure 8a and b). The nsTA difference spectra of TCPP and PCN-223 were almost identical, having an intense ground state bleach at ~420 nm followed by an excited state absorption centered near 470 nm. The study also revealed that the nature of the excited state did not change between the nanosecond to microsecond time domain (see Supplementary Information, Section 3.5.10). The transient absorption decay of TCPP at 470 nm exhibited single-exponential kinetics with a lifetime of 260 ± 7 μs (Fig. 8c). The triplet lifetime of TCPP was in good agreement with the previously reported studies.[41] PCN-223 also exhibited a mono-exponential decay with a lifetime of 201 ± 27 μs (Fig. 8d).

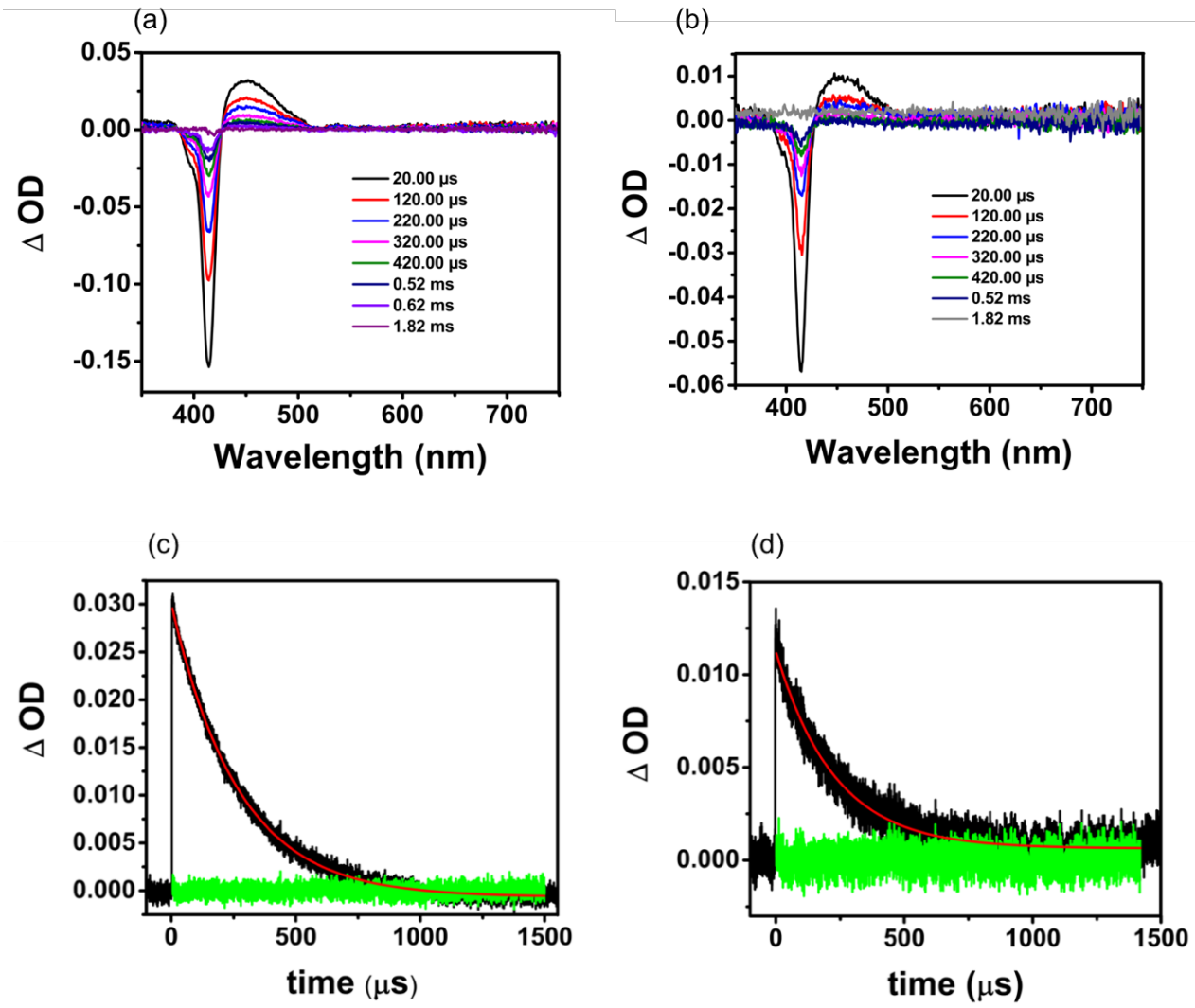

Figure 8. Transient absorption difference spectra (mapping) of (a) TCPP and (b) PCN-223 measured in degassed water at room temperature following 532 nm pulsed laser excitation (4-5 mJ/pulse, 5−7 ns fwhm). Both difference spectra represent an average of 30 transients. Fitted transient absorption decay of (c) TCPP and (d) PCN-223 along with the residuals (green colored). Both the transient absorption kinetic measurements were probed at 470 nm.

Due to the rigidity of the MOF structure, the rate of non-radiative deactivation pathways is expected to decrease, which in turn should lead to an increase in the lifetime of TCPP incorporated in PCN-223. Contrastingly, the lifetime of PCN-223 was found to be relatively shorter as compared to the ligand. The shorter triplet lifetime of PCN-223 may be attributed to energy transfer

pathways within the donor-acceptor framework. One of the possible pathways could be energy transfer to trap sites such as N-protonated porphyrins. In order to further investigate the role of N-protonated porphyrins as quenchers, nanosecond transient absorption measurements were attempted at different pH values. However, the strength of transient signal dramatically decreases on lowering the pH, resulting in poor signal-to-noise ratio. Consequently, nsTA measurements were not successful at low pH.

3.3.5 Femtosecond Transient absorption spectroscopy

To further map the excited state trajectory across all available timescales, ultrafast transient absorption (fsTA) studies were performed on TCPP and PCN-223 with 400 nm excitation and probe wavelengths that ranged across the UV-Visible region. The fsTA difference spectra of both TCPP and PCN-223 consist of a ground state bleach at 415 nm followed by an excited state absorption band starting at 430 nm. Composite spectral features that can be attributed to ground state bleach (from the Q band absorption) and excited state absorption can be observed in the 500-650 nm range. The evolution of their transients is presented in Figure 9a and b. Over the course of the first 500 fs, the ground state bleach at 415 nm and the excited state absorbance centered near 470 nm appear. As time progresses, no change is observed in the positions of the bands. The features in the fsTA difference spectrum of TCPP and PCN-223 qualitatively match those of the nsTA difference spectrum (see Supplementary Information, Section 3.5.11), signifying that the nature of excited state in both the ligand and the MOF did not change as we moved from the femtosecond to microsecond time domain.

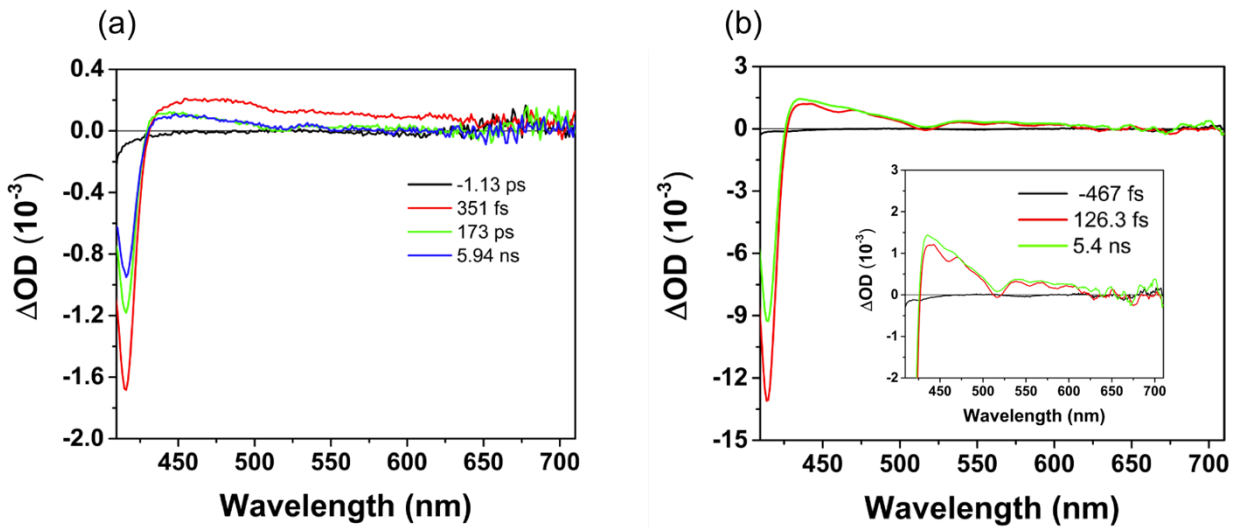

Figure 9. Transient absorption difference spectra of (a)TCPP (in a 1:1 (v/v) water-ethanol mixture (~ 10^{-6} M)) at pH-8 following 400 nm pulsed laser excitation (140 fs fwhm), (b) PCN-223 in water at pH-8 following 400 nm pulsed laser excitation (140 fs fwhm). Inset shows an expanded view of the excited state absorption band. Experimental delay times are indicated in the legend.

The transient kinetics of TCPP were probed at 418 nm and 506 nm, and analyzed using single and multiexponential models (see Supplementary Information, Section 3.5.12). The kinetic trace at 418 nm was best fit to a triexponential model. The lifetimes determined from the fit are provided in Table 3. Following previous assignments provided in the literature,[42–47] the shortest component (τ_1) is assigned to a solvent-induced process that causes vibrational reorganization of excitation energy in the S_1 state of TCPP (solvent reorganization). Elastic collisions between the ligand and solvent molecules are believed to be responsible for this process. The second component (τ_2) is attributed to vibrational relaxation of the first excited state (S_1) due to interaction with solvent molecules (vibrational cooling). The third component is too long to be measured accurately with our apparatus and is attributed to fluorescence in TCPP.[42] The trace at 506 nm exhibited single exponential decay kinetics with a lifetime consistent with the vibrational cooling component of excited state relaxation.

Table 3. Time constants obtained for TCPP in 1:1 water-ethanol mixture at selected probe wavelengths (pump wavelength = 400 nm)

Wavelength (nm)	τ_1 (ps)	τ_2 (ps)	τ_3 (ns)
418 nm	2 ± 1	57 ± 22	>1
506 nm	51 ± 26	-	-

In the case of PCN-223 MOF, the kinetics were probed at 348 nm and 510 nm (see Supplementary Information, Section 3.5.12). Kinetic analysis of the ultrafast data revealed the presence of three distinct time constants (Table 4). Based on a comparison between the time constants of TCPP and PCN-223, the first component (τ_1) is assigned to solvent reorganization. The second component (τ_2) is assigned to vibrational cooling in the MOF. The third component ($\tau_3 > 1$ ns) is assigned to fluorescence in the MOF.

Table 4. Time constants obtained for PCN-223 in water at selected probe wavelengths (pump wavelength = 400 nm)

Wavelength (nm)	τ_1 (ps)	τ_2 (ps)	τ_3 (ns)
348 nm	5 ± 2	115 ± 22	>1
510 nm	123 ± 29	-	-

It is worth noting that the lifetime corresponding to solvent reorganization and vibrational cooling in the MOF is higher than the free ligand. Such an observation can be explained by three hypotheses. The first is that immobilization of the TCPP within the rigid structure of MOF decreases the number of vibrational modes able to couple to this cooling process. It has been previously reported that immobilization of chromophores in MOFs decreases the rate of non-radiative excited state decay, leading to longer lifetimes.[48,49] The second is that the solvent molecules coupled to the vibrational cooling process have less accessibility to the porphyrin units

in the MOF. The third hypothesis attributes the differences in the lifetimes of TCPP and MOF samples to the different solvent systems used to measure each. Ultrafast TA measurements on TCPP samples were conducted in a 1:1 (v/v) mixture of water and ethanol. Ethanol was added to improve the solubility of TCPP in water, which in turn improves its absorbance. On the other hand, fsTA measurements on MOF samples were conducted in water (without ethanol). The difference in solvent polarities may be responsible for the higher lifetimes in MOF.

3.4 Conclusions

In summary, PCN-223 MOF was synthesized from free-base TCPP and was thoroughly characterized. The photophysical properties of the synthesized MOF and the free ligand were explored extensively using various steady state and time-resolved spectroscopic techniques. pH-dependent fluorescence quenching experiments were performed on TCPP and PCN-223. Stern-Volmer analysis of quenching data revealed that the quenching rate constant for PCN-223 is more than an order of magnitude larger than that for TCPP. Furthermore, PCN-223 demonstrated a significantly higher extent of quenching (Φ_q = 93%) as compared to monomeric TCPP solution (Φ_q = 51%), at similar concentrations of quencher. The enhanced quenching in MOF is attributed to energy transfer from neutral TCPP linkers to N-protonated TCPP linkers. The rate constant of EET in the MOF was estimated using the Förster energy transfer model and its magnitude was found to be consistent with other porphyrin-based MOFs. The temperature dependence of the fluorescence decay rates of PCN-223 was comparable to that of monomeric TCPP units, suggesting that the interchromophoric interactions between TCPP linkers belong to the weak coupling regime. Therefore, an incoherent, step-by-step hopping mechanism was proposed for EET in PCN-223. Femtosecond and nanosecond transient absorption studies were conducted on free ligand and MOF to characterize their excited state properties. Nanosecond transient absorption

decays showed that the triplet lifetime of MOF is shorter than that of free ligand, which may be due to triplet-triplet energy transfer in the MOF. The enhanced energy migration distance in PCN-223 MOF (173 Å in 3D) suggests that it is a promising candidate to play the role of light harvesting antennae in solar energy conversion devices.

3.5 Supplementary Information

3.5.1 Thermogravimetric analysis

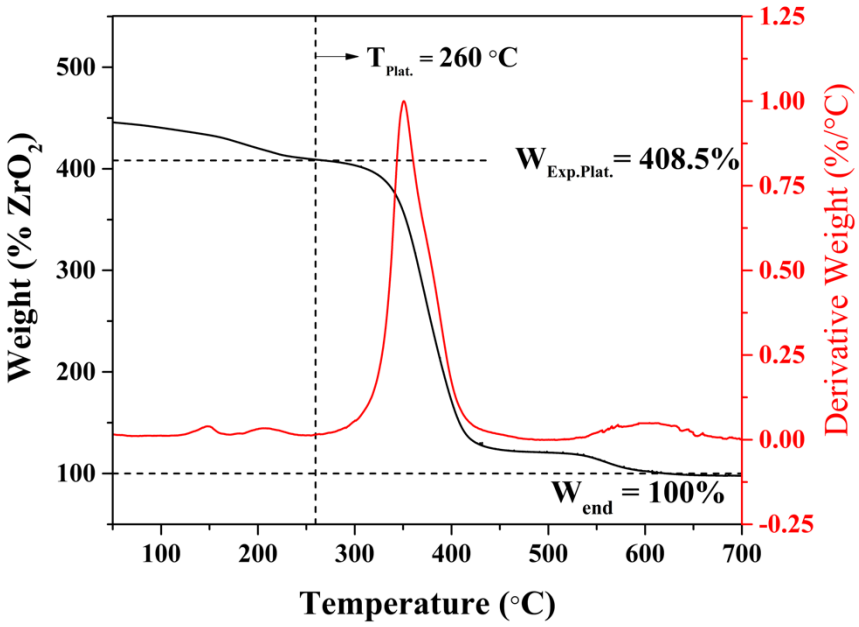

Figure S1. TGA plot of PCN-223. The intersection of the horizontal and vertical dashed lines pinpoints the theoretically expected TGA plateau for PCN-223.

The reaction for the complete combustion of ideal (defect-free), hydroxylated PCN-223 MOF is-

$$Zr_6O_4(OH)_4(TCPP)_3\ (s) + 154.5\ O_2\ (g) \rightarrow 6\ ZrO_2\ (s) + 144\ CO_2\ (g) + 41\ H_2O\ (g)$$

$$\frac{\text{moles of } Zr_6O_4(OH)_4(TCPP)_3}{\text{moles of } ZrO_2} = \frac{1}{6}$$

$$\text{moles of } Zr_6O_4(OH)_4(TCPP)_3 = \frac{\text{moles of } ZrO_2}{6}$$

$$\left(\frac{W_{\text{TGA plateau}}}{W_{\text{end}}}\right)_{\text{theoretical}} = \frac{MW_{Zr_6O_4(OH)_4(TCPP)_3}}{6 \times MW_{ZrO_2}}$$

$$\left(\frac{W_{\text{TGA plateau}}}{W_{\text{end}}}\right)_{\text{theoretical}} = \frac{3039.57}{6 \times 123.22}$$

$$\left(\frac{W_{\text{TGA plateau}}}{W_{\text{end}}}\right)_{\text{theoretical}} = 4.11$$

If the end weight of the TGA run is normalized to 100%, then for hydroxylated, defect-free, solvent-free PCN-223 material, the experimental TGA plateau should be found at 411% on the TGA curve. By using the experimental $\left(\frac{W_{\text{TGA plateau}}}{W_{\text{end}}}\right)$ ratio, the effective molecular weight of a MOF can be calculated,

$$MW_{\text{effective}} = \left(\frac{W_{\text{TGA plateau}}}{W_{\text{end}}}\right)_{\text{experimental}} \times 6 \times MW_{ZrO_2}$$

$$\text{For PCN-223, } \left(\frac{W_{\text{TGA plateau}}}{W_{\text{end}}}\right)_{\text{experimental}} = \mathbf{4.085}$$

$$MW_{\text{effective}} = 4.085 \times 6 \times 123.2 = 3019.6 \text{ g/mol}$$

The general molecular formula for a hydroxylated PCN-223 MOF in which modulator loss has not occurred is $Zr_6O_4(OH)_4(TCPP)_x(Mod)_{([Mod]/[Ligand])x}$. The value of x in this formula can be determined by,

$$x = \frac{MW_{effective} - 547.2 - 64 - 68}{786.79 + MW_{Modulator} \times ([Mod]/[Ligand])}$$

The modulator to ligand molar ratio in the framework ([Mod]/[Ligand]) for PCN-223 was found to be is 1.48 (from ^{1}H NMR analysis).

$$x = \frac{3019.6 - 547.2 - 64 - 68}{786.79 + (74.08 \times 1.48)} = \mathbf{2.61}$$

The resulting molecular formula of the MOF is $\mathbf{Zr_6O_4(OH)_4(TCPP)_{2.61}(Mod)_{3.84}}$

Propionic acid (PA) is the modulator used in the synthesis. Therefore, the molecular formula of MOF is $\mathbf{Zr_6O_4(OH)_4(TCPP)_{2.61}(PA)_{3.84}}$

3.5.2 Nitrogen gas adsorption isotherm

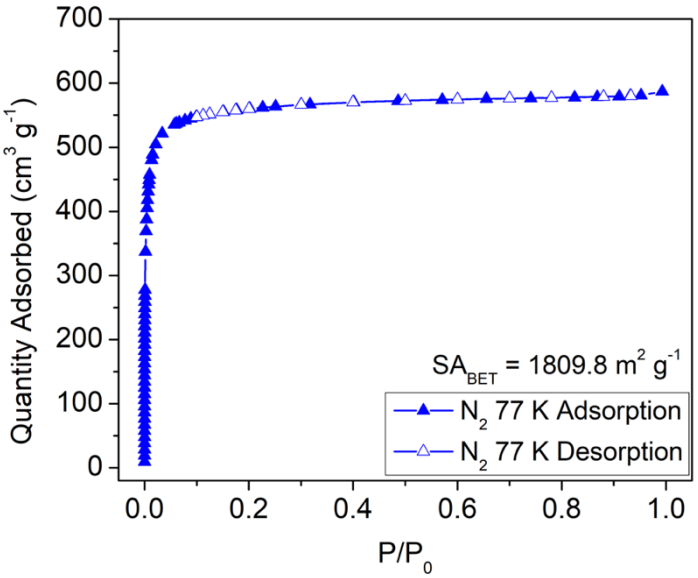

Figure S2. N_2 gas adsorption isotherm of PCN-223 MOF

The BET surface area of the MOF was found to be 1809.8 m^2 g^{-1}, which agrees with previously published literature.[10]

3.5.3 Acid-base titration curves of TCPP and PCN-223

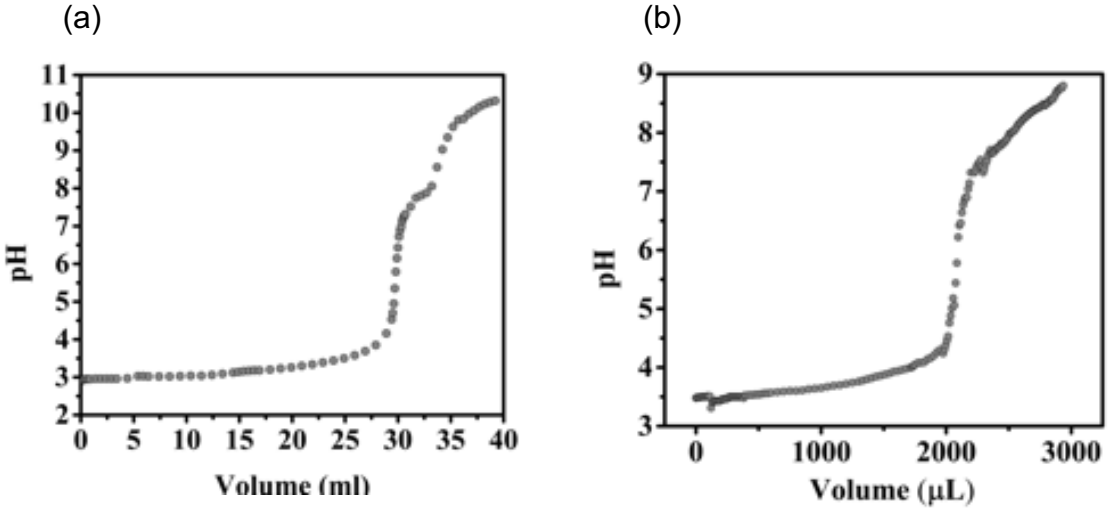

Figure S3. (a) Titration curve of TCPP in water (10^{-6}M) against 0.01 M NaOH solution. The first and second equivalence points of titration are around pH 5.54 and 7.5 respectively (b) Titration curve of PCN-223 in water against 0.01 M NaOH solution. The equivalence point of titration is around pH 5.70.

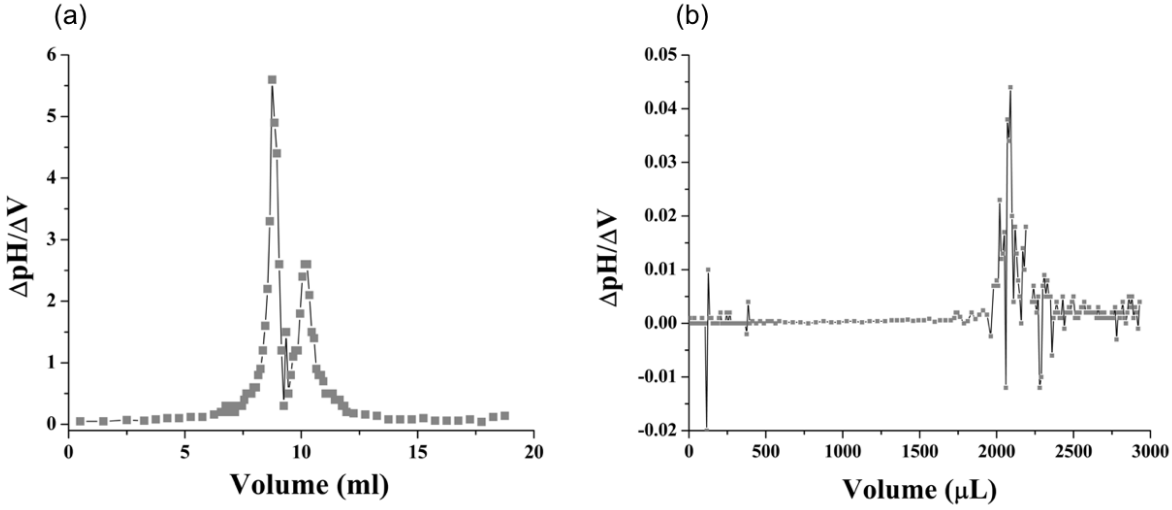

Figure S4. (a) First derivative of the titration curve for TCPP as a function of volume of titrant (b) First derivative of the titration curve for PCN-223 as a function of volume of titrant.

3.5.4 Absorption data for TCPP and PCN-223

Table 1. Positions of Soret (B) band and Q bands in the diffused absorption spectra of TCPP and PCN-223

	B(Soret)	$Q_y(1,0)$	$Q_y(0,0)$	$Q_x(1,0)$	$Q_x(0,0)$
TCPP	425nm	525nm	561nm	597nm	652nm
PCN-223	412nm	524nm	561nm	595nm	652nm

3.5.5 Determination of $[HP^{2+}]/[P]$ in TCPP solutions and MOF suspensions

The ratio of the concentration of protonated porphyrins to that of neutral porphyrins in TCPP solutions and MOF suspensions was determined using the Henderson-Hasselbalch equation.

$pH = pK_a + \log_{10}([P]/[HP^{2+}])$

$[P]/[HP^{2+}] = 10^{pH-pK_a}$

$[HP^{2+}]/[P] = \frac{1}{10^{(pH-pK_a)}}$

The concentration of N-protonated TCPP in solution is ~1% at pH 5.5. The emission intensity of monomeric TCPP at pH 5.5 was set as I_q. The emission intensity of TCPP at pH 8 was set as I_0. Φ_q for TCPP was estimated to be 51%.

The concentration of N-protonated TCPP in PCN-223 is ~1% at pH 6. The emission intensity of the MOF at pH 6 was set as I_q. The emission intensity of the MOF at pH 8 was set as I_0. Φ_q for the MOF was estimated to be 93%.

3.5.6 Emission spectra of TCPP and PCN-223 as a function of temperature

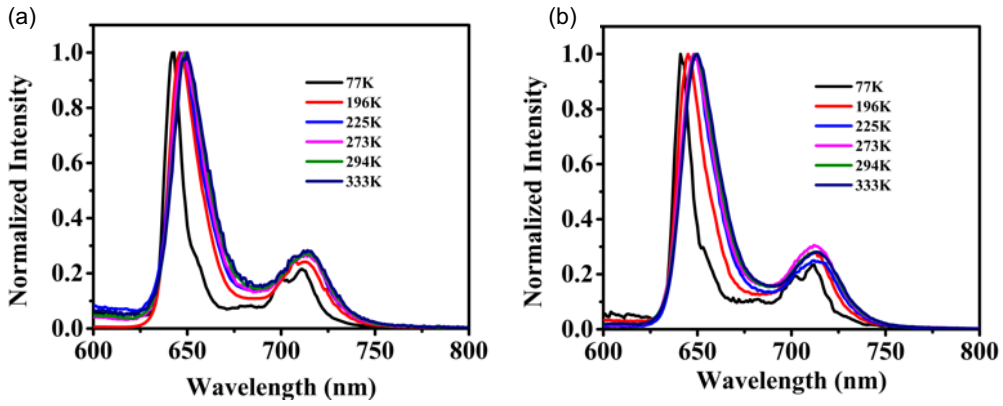

Figure S5. (a) Steady-state emission spectra of TCPP as a function of temperature (b) Steady-state emission spectra of PCN-223 as a function of temperature.

3.5.7 Spectral overlap integral calculation

$$J(\lambda) = \int_0^\infty \varepsilon_A(\lambda)\, \lambda^4\, F_D(\lambda)\, d\lambda$$

where ε_A is the extinction coefficient spectrum of the acceptor in units of $M^{-1}cm^{-1}$, λ is the wavelength in nm and F_D is the wavelength dependent donor emission spectrum normalized to an area of 1.

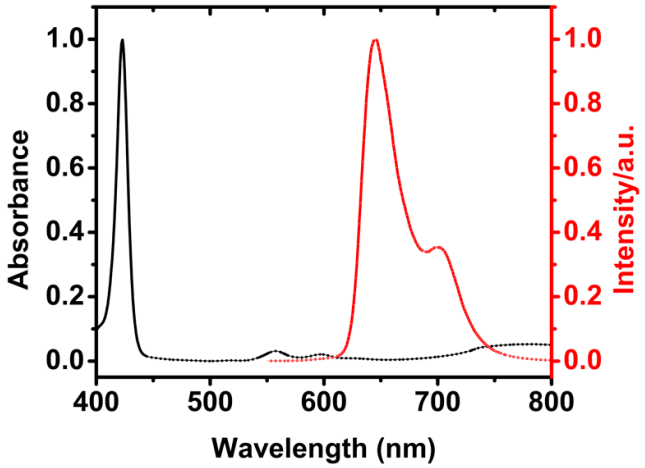

Figure S6. Spectral overlap between the absorption spectrum of N-protonated TCPP (acceptor) and emission spectrum of neutral TCPP (donor)

The spectral overlap integral was estimated to be $5.344 \times 10^{-14}\ M^{-1}cm^3$.

3.5.8 Quantum yield calculation

The relative quantum yield of donor (neutral TCPP) in the absence of acceptor (protonated TCPP) was calculated using,

$$\frac{Q}{Q_R} = \frac{I}{I_R} \times \frac{OD_R}{OD} \times \frac{\eta^2}{\eta_R^2}$$

where Q is the quantum yield, I is the integrated intensity, η is the refractive index, and OD is the optical density. The subscript R refers to the reference fluorophore of known quantum yield.

Quantum yield of neutral TCPP in methanol (reference) = 0.09.

Quantum yield of neutral TCPP (in water) was estimated to be 0.27 ± 0.035.

3.5.9 Closest interchromophoric distance in PCN-223

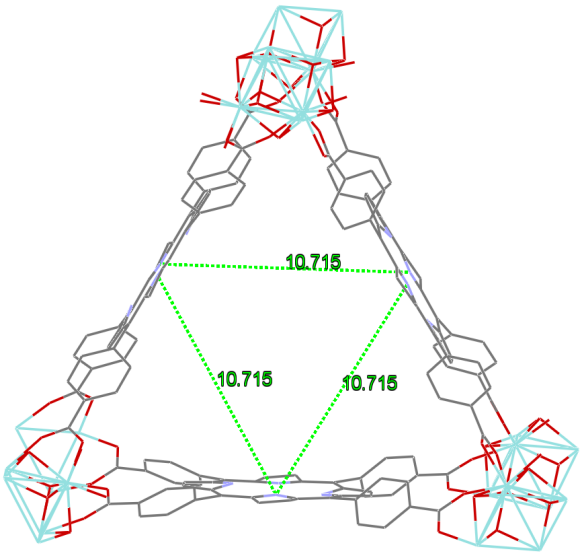

Figure S7. Molecular model of PCN-223 generated using X-ray diffraction data.[10] The closest center-to-center donor-acceptor distance in the model is 10.715 Å.

3.5.10 Transient absorption difference spectra

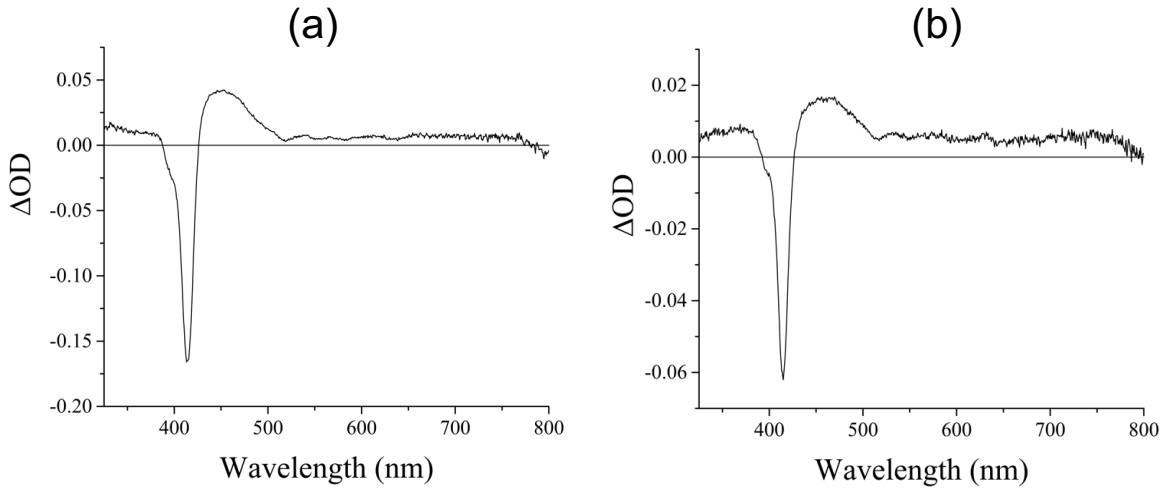

Figure S8. Transient absorption difference spectra of (a) TCPP and (b) PCN-223 measured in degassed water at room temperature following 532 nm pulsed laser excitation (4-5 mJ/pulse, 5−7 ns fwhm). Both difference spectra represent an average of 30 transients.

3.5.11 Comparison between nanosecond and femtosecond TA difference spectra

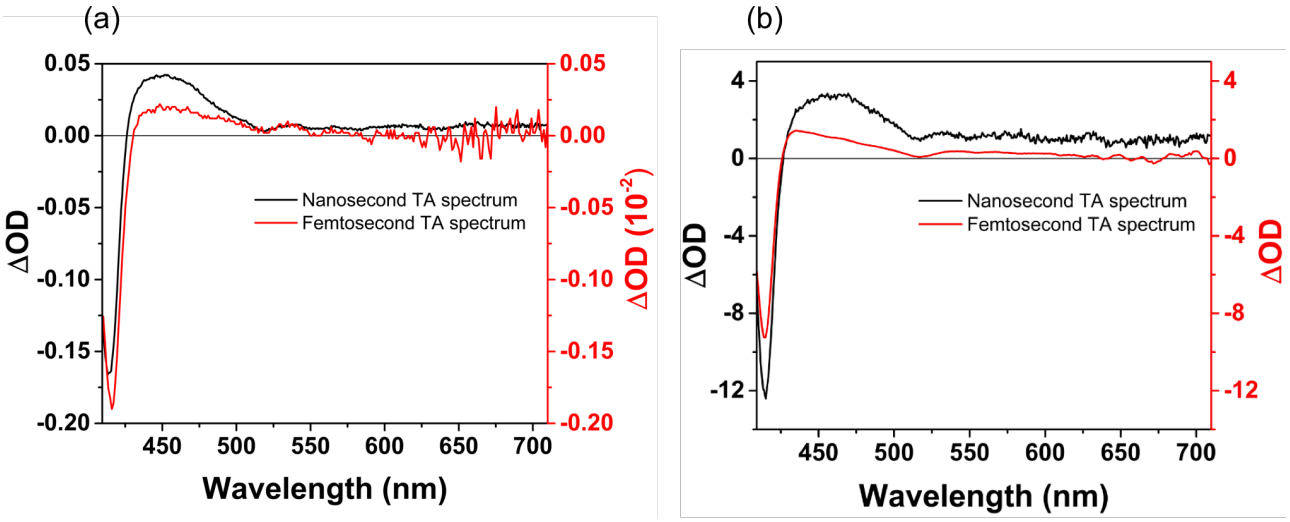

Figure S9. Comparison between the femtosecond TA (at a time delay of 5.5 ns) and nanosecond TA difference spectra (collected promptly after laser excitation) of (a) TCPP and (b) PCN-223.

3.5.12 Kinetic analysis of the ultrafast data

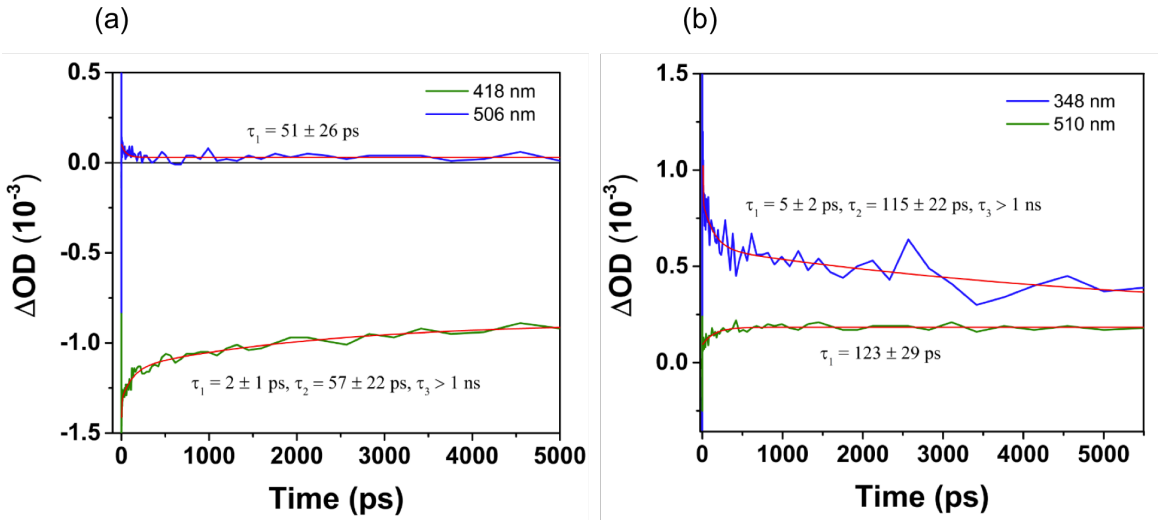

Figure S10. Transient absorption kinetic traces of (a) TCPP in 1:1 water-ethanol (v/v) mixture (pH-8) and (b) PCN-223 in water (pH-8) following 400 nm pulsed laser excitation (140 fs fwhm) at probe wavelengths indicated in the legend. Time components of the kinetic traces obtained from fitting are shown in the figure.

3.6 References

(1) Renger, T. *Photosynth. Res.* **2009**, *102* (2), 471–485.

(2) Yang, J.; Yoon, M.-C.; Yoo, H.; Kim, P.; Kim, D. *Chem. Soc. Rev.* **2012**, *41* (14), 4808–4826.

(3) Li, Y.; Xu, H.; Ouyang, S.; Ye, J. *Phys. Chem. Chem. Phys.* **2016**, *18* (11), 7563–7572.

(4) So, M. C.; Wiederrecht, G. P.; Mondloch, J. E.; Hupp, J. T.; Farha, O. K. *Chem. Commun.* **2015**, *51* (17), 3501–3510.

(5) Furukawa, H.; Cordova, K. E.; O'Keeffe, M.; Yaghi, O. M. *Science (80-.).* **2013**, *341* (August), 974.

(6) Kuc, A.; Enyashin, A.; Seifert, G. *J. Phys. Chem. B* **2007**, *111* (28), 8179–8186.

(7) Feng, D.; Gu, Z.-Y.; Li, J.-R.; Jiang, H.-L.; Wei, Z.; Zhou, H.-C. *Angew. Chemie Int. Ed.* **2012**, *51* (41), 10307–10310.

(8) Jiang, H.-L.; Feng, D.; Wang, K.; Gu, Z.-Y.; Wei, Z.; Chen, Y.-P.; Zhou, H.-C. *J. Am. Chem. Soc.* **2013**, *135* (37), 13934–13938.

(9) Morris, W.; Volosskiy, B.; Demir, S.; Gándara, F.; McGrier, P. L.; Furukawa, H.; Cascio, D.; Stoddart, J. F.; Yaghi, O. M. *Inorg. Chem.* **2012**, *51* (12), 6443–6445.

(10) Feng, D.; Gu, Z.-Y.; Chen, Y.-P.; Park, J.; Wei, Z.; Sun, Y.; Bosch, M.; Yuan, S.; Zhou, H.-C. *J. Am. Chem. Soc.* **2014**, *136* (51), 17714–17717.

(11) Feng, D.; Jiang, H.-L.; Chen, Y.-P.; Gu, Z.-Y.; Wei, Z.; Zhou, H.-C. *Inorg. Chem.* **2013**, *52* (21), 12661–12667.

(12) Deria, P.; Gómez-Gualdrón, D. A.; Hod, I.; Snurr, R. Q.; Hupp, J. T.; Farha, O. K. *J. Am. Chem. Soc.* **2016**, *138* (43), 14449–14457.

(13) Deria, P.; Yu, J.; Balaraman, R. P.; Mashni, J.; White, S. N. *Chem. Commun.* **2016**, *52* (88), 13031–13034.

(14) Seybold, P. G.; Gouterman, M. *J. Mol. Spectrosc.* **1969**, *31* (1–13), 1–13.

(15) Biesaga, M.; Pyrzyńska, K.; Trojanowicz, M. *Talanta* **2000**, *51* (2), 209–224.

(16) Lo, P.-C.; Leng, X.; Ng, D. K. P. *Coord. Chem. Rev.* **2007**, *251* (17), 2334–2353.

(17) Rudine, A. B.; DelFatti, B. D.; Wamser, C. C. *J. Org. Chem.* **2013**, *78* (12), 6040–6049.

(18) Hynninen, P. H. *J. Chem. Soc. Perkin Trans. 2* **1991**, No. 5, 669–678.

(19) Kruk, M. M.; Starukhin, A. S.; Maes, W. *Macroheterocycles* **2011**, *4* (2), 69–79.

(20) Zhu, J.; Shaikh, S.; Mayhall, N. J.; Morris, A. J. In *Elaboration and Applications of Metal-Organic Frameworks*; Series on Chemistry, Energy and the Environment; WORLD SCIENTIFIC, 2017; Vol. Volume 2, pp 581–654.

(21) Valeur, B.; Berberan-Santos, M. N. *Excitation Energy Transfer*; 2012.

(22) De Rossi, U.; Dähne, S.; Gomez, U.; Port, H. *Chem. Phys. Lett.* **1998**, *287* (3), 395–402.

(23) Abrahamsson, M.; Becker, H.-C.; Hammarström, L.; Bonnefous, C.; Chamchoumis, C.; Thummel, R. P. *Inorg. Chem.* **2007**, *46* (24), 10354–10364.

(24) Abrahamsson, M.; Becker, H.-C.; Hammarström, L. *Dalt. Trans.* **2017**, *46* (39), 13314–13321.

(25) Son, H. J.; Jin, S.; Patwardhan, S.; Wezenberg, S. J.; Jeong, N. C.; So, M.; Wilmer, C. E.; Sarjeant, A. A.; Schatz, G. C.; Snurr, R. Q.; Farha, O. K.; Wiederrecht, G. P.; Hupp, J. T. *J. Am. Chem. Soc.* **2013**, *135* (2), 862–869.

(26) Patwardhan, S.; Jin, S.; Son, H.-J.; Schatz, G. C. *Mater. Res. Soc. Symp. Proc.* **2013**, *1539*, 22–27.

(27) Son, H.-J.; Jin, S.; Patwardhan, S.; Wezenberg, S. J.; Jeong, N. C.; So, M.; Wilmer, C. E.; Sarjeant, A. A.; Schatz, G. C.; Snurr, R. Q.; Farha, O. K.; Wiederrecht, G. P.; Hupp, J. T. *J. Am. Chem. Soc.* **2013**, *135* (2), 862–869.

(28) Lee, C. Y.; Farha, O. K.; Hong, B. J.; Sarjeant, A. A.; Nguyen, S. T.; Hupp, J. T. *J. Am. Chem. Soc.* **2011**, *133* (40), 15858–15861.

(29) Kent, C. A.; Mehl, B. P.; Ma, L.; Papanikolas, J. M.; Meyer, T. J.; Lin, W. *J. Am. Chem. Soc.* **2010**, *132* (37), 12767–12769.

(30) Zhang, Q.; Zhang, C.; Cao, L.; Wang, Z.; An, B.; Lin, Z.; Huang, R.; Zhang, Z.; Wang, C.; Lin, W. *J. Am. Chem. Soc.* **2016**, *138* (16), 5308–5315.

(31) Dexter, D. L. *J. Chem. Phys.* **1953**, *21* (5), 836.

(32) Lin, J.; Hu, X.; Zhang, P.; Van Rynbach, A.; Beratan, D. N.; Kent, C. A.; Mehl, B. P.; Papanikolas, J. M.; Meyer, T. J.; Lin, W.; Skourtis, S. S.; Constantinou, M. *J. Phys. Chem. C* **2013**, *117* (43), 22250–22259.

(33) Andrews, D. L. *Chem. Phys.* **1989**, *135* (2), 195–201.

(34) Maligaspe, E.; Kumpulainen, T.; Lemmetyinen, H.; Tkachenko, N. V.; Subbaiyan, N. K.; Zandler, M. E.; D'Souza, F. *J. Phys. Chem. A* **2010**, *114* (1), 268–277.

(35) Majoul I., Jia Y., D. R. *Practical Fluorescence Resonance Energy Transfer or Molecular Nanobioscopy of Living Cells*; Springer, Boston, MA, 2006.

(36) Kim, T.; Ham, S.; Lee, S. H.; Hong, Y.; Kim, D. *Nanoscale* **2018**, *10* (35), 16438–16446.

(37) Siebbeles, L. D. A.; Huijser, A.; Savenije, T. J. *J. Mater. Chem.* **2009**, *19* (34), 6067–6072.

(38) Maza, W. A.; Haring, A. J.; Ahrenholtz, S. R.; Epley, C. C.; Lin, S. Y.; Morris, A. J. *Chem. Sci.* **2016**, *7* (1), 719–727.

(39) Kaushal, M.; Ortiz, A. L.; Kassel, J. A.; Hall, N.; Lee, T. D.; Singh, G.; Walter, M. G. *J. Mater. Chem. C* **2016**, *4* (24), 5602–5609.

(40) Mikhnenko, O. V; Blom, P. W. M.; Nguyen, T.-Q. *Energy Environ. Sci.* **2015**, *8* (7), 1867–1888.

(41) Kathiravan, A.; Renganathan, R.; Anandan, S. *J. Colloid Interface Sci.* **2010**, *348* (2), 642–648.

(42) Baskin, J. S.; Yu, H.-Z.; Zewail, A. H. *J. Phys. Chem. A* **2002**, *106* (42), 9837–9844.

(43) Yu, H.-Z.; Baskin, J. S.; Zewail, A. H. *J. Phys. Chem. A* **2002**, *106* (42), 9845–9854.

(44) Kumble, R.; Palese, S.; Lin, V. S.-Y.; Therien, M. J.; Hochstrasser, R. M. *J. Am. Chem. Soc.* **1998**, *120* (44), 11489–11498.

(45) Li, X.; Gong, C.; Gurzadyan, G. G.; Gelin, M. F.; Liu, J.; Sun, L. *J. Phys. Chem. C* **2018**, *122* (1), 50–61.

(46) Sorgues, S.; Poisson, L.; Raffael, K.; Krim, L.; Soep, B.; Shafizadeh, N. *J. Chem. Phys.* **2006**, *124* (11), 114302.

(47) Rodriguez, J.; Kirmaier, C.; Holten, D. *J. Chem. Phys.* **1991**, *94* (9), 6020–6029.

(48) Maza, W. A.; Padilla, R.; Morris, A. J. *J. Am. Chem. Soc.* **2015**, *137* (25), 8161–8168.

(49) Maza, W. A.; Morris, A. J. *J. Phys. Chem. C* **2014**, *118* (17), 8803–8817.

4. Preparation of Novel MOF-on-MOF composites for Achieving Directional Energy Transfer (ongoing project)

4.1 Introduction

Millions of years of evolution have facilitated the development of highly sophisticated light harvesting complexes (LHC's) in natural photosynthetic systems.[1,2] Pigment chromophores in LHC's perform the dual role of absorbing light energy and then efficiently funneling it towards the reaction centers. The ability of LHC's to carry out directional energy transfer has fascinated scientists for a long time. Recently, a significant amount of research effort has been dedicated towards developing materials with geometric layouts that promote directional energy transfer.[3–7] Materials with core-shell architectures have emerged as promising candidates for achieving long-range, directional energy transfer.[8–13] Core shell particles are biphasic in nature with an inner core structure and outer shell made of different components. By confining photoactive donor species in the core and acceptor species in the shell layer, one can spatially isolate the donors and acceptors. Arranging donor and acceptor species in spatially separated domains gives rise to an energy cascade, resulting in directed energy transfer from core to shell. Metal-organic frameworks (MOFs) have proven to be viable platforms for incorporating a wide variety of chromophores and systematically studying energy transfer. Previous studies have confirmed the presence of efficient, long-distance ligand-to-ligand energy transfer in photoactive MOFs.[14–23] In this chapter, we present synthesis and structural characterization of photoactive core-shell MOF composites that can potentially demonstrate directional energy transfer.

Metal organic frameworks (MOFs), also known as coordination polymers, are formed by the self-assembly of inorganic nodes (metal ions or clusters) with organic ligands via coordination bonds.[24,25] Due to their well-defined structures, large surface areas, and structural and functional

tunability, MOFs have shown remarkable potential in applications such as light-harvesting, catalysis, drug-delivery, gas storage and gas separation.[23,24,26–30] Recently, MOF-on-MOF composites with core-shell architecture have attracted great interest from the scientific community.[37] MOF-on-MOF composites offer the unique possibility of effectively combining the advantageous attributes of both the MOFs, and negating the disadvantages of constituent single components. Furthermore, there is potential for the discovery of novel synergistic effects, which cannot be achieved by the individual components. MOF-on-MOF composites with lattice mismatch between the core MOF and shell MOF are difficult to construct but are highly coveted as they afford additional levels of structural and functional diversity. The difference between the chemical composition and morphology of core and shell layers can be exploited to tailor the properties of core-shell MOFs for desired applications. Zhou and co-workers have previously reported the synthesis of core-shell lattice-mismatched MOFs.[31] Guided by a kinetically controlled strategy, they demonstrated one-pot synthesis of UiO-67-on-PCN-222 composites by solvothermal reaction between $ZrCl_4$, BPDC (biphenyl-4,4′-dicarboxylate) and TCPP (meso-tetrakis(4-carboxyphenyl)porphyrin). Due to the high connectivity of TCPP ligands, they bind preferentially to the Zr^{4+} ions and quickly form the rod-shaped PCN-222 crystals. These crystals then act as seeds and facilitate the growth of UiO-67 shell layer on their surface. Since heterogeneous nucleation is kinetically more favorable than homogeneous nucleation, growth of the core-shell structure is preferred over the formation of two MOFs as separate phases.

Herein, we aim to employ UiO-67-on-PCN-222 composites as model systems to explore the possibility of achieving directional energy transfer in MOF-based core-shell structures. Known amounts of Ruthenium(II) tris(5,5′-dicarboxy-2,2′-bipyridine), RuDCBPY, were doped in the shell

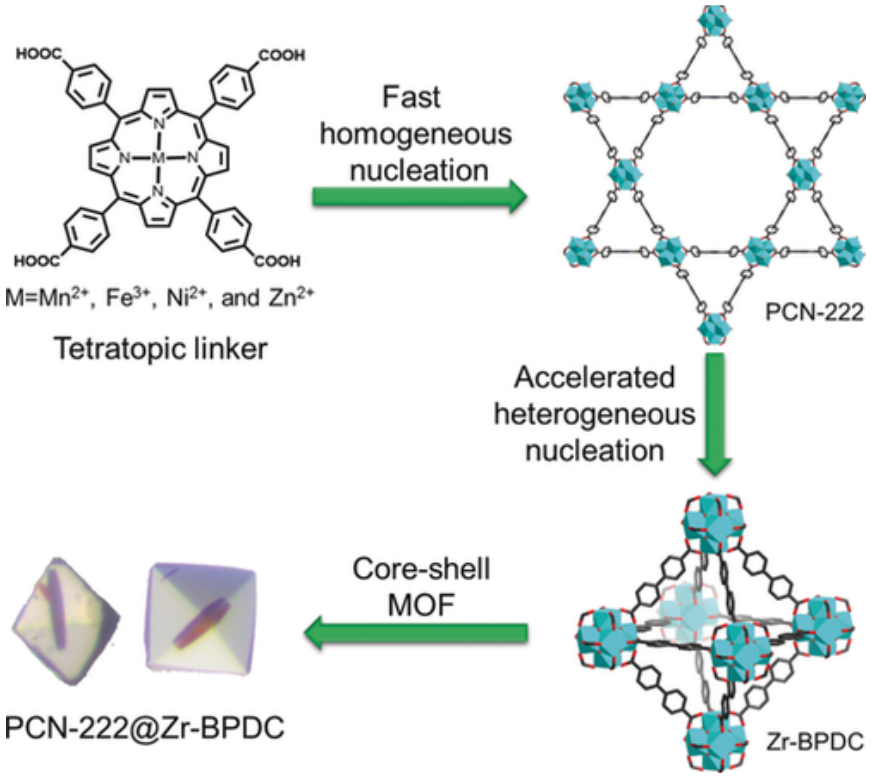

Figure 1. Kinetically guided synthesis procedure of UiO-67-on-PCN-222 composites (referred to as PCN-222@Zr-BPDC by Zhou and co-workers). Reproduced from reference 31 with permission.

layer to produce a series of Ru-UiO-67-on-PCN-222 composites with varying degree of RuDCBPY loading. DCBPY is isostructural with BPDC, which allows RuDCBPY to replace BPDC within the Zr-BPDC shell.[17,32,33] Sauvage and co-workers have previously studied the photoinduced processes in dyads consisting of a porphyrin unit and a ruthenium complex.[34] They reported that the lowest singlet excited state of the porphyrin moiety (S_1) is quenched by energy transfer to give the triplet metal-to-ligand charge-transfer excited state of the Ru complex (^{3}MLCT). We hypothesize that upon photo-excitation of TCPP units in the core, singlet-singlet energy transfer would occur between TCPP linkers. This process will continue until the excitation energy is transferred to a RuDCBPY unit across the interface, which quenches the excitation. Thus, directional energy transfer from core domain to shell layer will be achieved. The validity of this

hypothesis can be tested by investigating the photophysical properties of Ru-UiO-67-on-PCN-222 composites. Before exploring the energy transfer dynamics of Ru-UiO-67-on-PCN-222 composites, it is critical to confirm that (a) the as-prepared Ru-UiO-67-on-PCN-222 composites exhibit core-shell architecture, (b) PCN-222 and UiO-67 are the constituent components of the composites, and (c) RuDCBPY is incorporated in the UiO-67 shell layer. SEM (scanning electron microscopy) characterization was employed to confirm the formation of core-shell nanoparticles. PXRD (powder X-ray diffraction) analysis was carried out to assess the phase composition of composites and identify the constituent components. Diffuse reflectance spectroscopy and N_2 adsorption/desorption measurements were performed to confirm the incorporation of RuDCBPY in the UiO-67 shell layer. After completing structural characterization of composites, their photophysical properties will be investigated with the help of steady state and time resolved emission spectroscopy.

4.2 Materials and Methods

Synthesis of Zr-BPDC_on_PCN-222

$ZrCl_4$ (130 mg), TCPP (10 mg), BPDC (100 mg), trifluoroacetic acid (2.5 ml) and DMF (15 ml) were charged in a 6-dram vial. The mixture was heated in a 120℃ oven for 7 days. After cooling down to room temperature, the resulting powder was collected using centrifugation. It was washed several times with DMF and then soaked in DMF for two days (with fresh DMF replacement every day). The MOFs were then soaked in acetone, dried at room temperature and then activated by heating at 80 ºC under vacuum.

Synthesis of Ru-UiO-67-on-PCN-222

A series of Ru-UiO-67-on-PCN-222 samples (**CS-1**, **CS-2**, **and CS-3**) were prepared according to the following procedure. $ZrCl_4$ (130 mg), TCPP (10 mg), BPDC (100 mg) were added

to 15 ml of DMF and ultrasonically dissolved in a 6-dram vial. Then, RuDCBPY (10 mg for **CS-1**; 20 mg for **CS-2**, and 30 mg for **CS-3**) was added to the reaction mixture. The mixture was heated in a 120℃ oven for 7 days. After cooling down to room temperature, the resulting powder was collected using centrifugation. It was washed several times with DMF and then soaked in DMF for two days (with fresh DMF replacement every day). The MOFs were then soaked in acetone, dried at room temperature and then activated by heating at 80 ^{o}C under vacuum.

Powder X-ray Diffraction (PXRD)

A 600 W Rigaku MiniFlex powder diffractometer with a CuKα (0.15418 nm) radiation source was used, with a sweeping range of 2–25° in continuous scanning mode. PXRD traces were collected in 0.05° increments at a scanning rate of 0.5°/min.

Scanning Electron Microscopy (SEM)

SEM samples were prepared by suspending MOF powders in ethanol with sonication. The resulting suspensions were drop-casted on precut glass slides. After drying, the glass slides were mounted on SEM sample pegs with the help of double-sided copper tape. The sides of the glass slides and the platform of sample peg were coated with conductive carbon paint purchased from Electron Microscopy Sciences. A LEO (Zeiss) 1550 field-emission scanning electron microscope, equipped with an in-lens detector, operating at 5.0 kV was used to obtain high-resolution images of the MOF particles.

Diffuse reflectance spectroscopy

The diffuse reflectance spectra of TCPP and PCN-223(fb) were obtained using an Agilent Technologies 8453 UV-vis diode array spectrophotometer (1 nm resolution) where the sample compartment was replaced with an integration sphere. The powder samples were diluted by mixing with $BaSO_4$.

4.3 Results and Discussion

Synthesis of core-shell MOF composites was achieved by modifying a previously published procedure. Briefly, 5.6×10^{-4} mol of $ZrCl_4$, 1.3×10^{-5} mol of TCPP, 4.1×10^{-4} mol of BPDC were dissolved in 10 ml DMF along with 3.3×10^{-2} mol of trifluoroacetic acid as the modulator. After adding appropriate amounts of RuDCBPY, the mixture was sonicated for 15 minutes then the vial was placed in an oven and heated at 120 °C for 7 days. The resulting composites (**CS-1, CS-2, and CS-3**) were collected by centrifugation, washed with DMF and acetone, and then activated by heating at 100 °C under vacuum. PXRD analysis was carried out to assess the phase composition of core–shell composites (Figure 2). Diffraction peaks corresponding to PCN-222 and UiO-67 were observed in the experimental PXRD patterns, indicating that PCN-222 and UiO-67 are the constituent components of the core-shell composites.

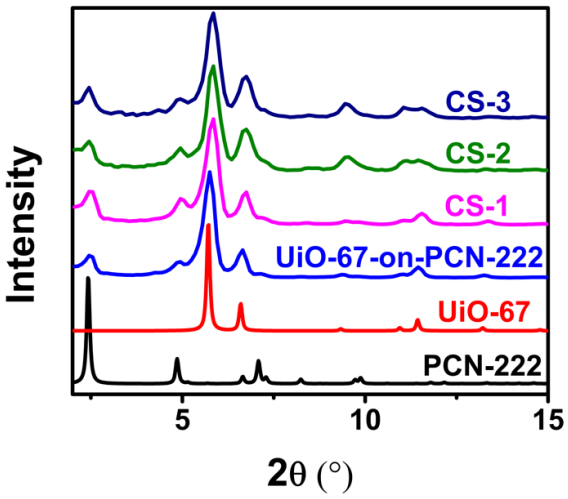

Figure 2. PXRD patterns of UiO-67-on-PCN-222, **CS-1**, **CS-2**, **and CS-3**.

SEM characterization was performed to confirm the core-shell nature of the composites. SEM imaging is a qualitative technique that is particularly useful for identifying the morphologies of MOF nanoparticles. SEM images from different cross sections of **CS-1**, **CS-2**, and **CS-3** confirmed the formation of core-shell composites (see Supplementary Information, Section 1). The SEM

images also detected small amounts of phase impurities (rod-shaped PCN-222 nanoparticles), indicating that **CS-1**, **CS-2**, and **CS-3** powders are a mixture of core–shell composites and PCN-222 nanoparticles. Hupp and co-workers have reported solvent-assisted separation of mixed MOFs on the basis of their density difference.[35] This method takes advantage of MOF density differences such that one MOF floats in a solvent of appropriate density while the other sinks. The densities of core–shell composites and PCN-222 nanoparticles should be distinctly different, allowing facile separation of the two phases. Efforts are currently underway to isolate the core–shell composites.

Incorporation of RuBPDCY in the composites was confirmed with the help of diffuse reflectance spectroscopy. The diffuse reflectance profiles of **CS-1**, **CS-2**, and **CS-3** are shown in Figure 3. The reflectance values corresponding to 480 nm show an increasing trend as we go from **Cs-1** to **Cs-3** (Figure 3). Bearing in mind that the λ_{max} of RuDCBPY is ~480nm, this trend indicates that RuDCBPY loading is lowest in **CS-1** and highest in **CS-3** (see Supplementary Information, Section 2). We were, therefore, successful in preparing core-shell composites with varying degrees of RuDCBPY loading.

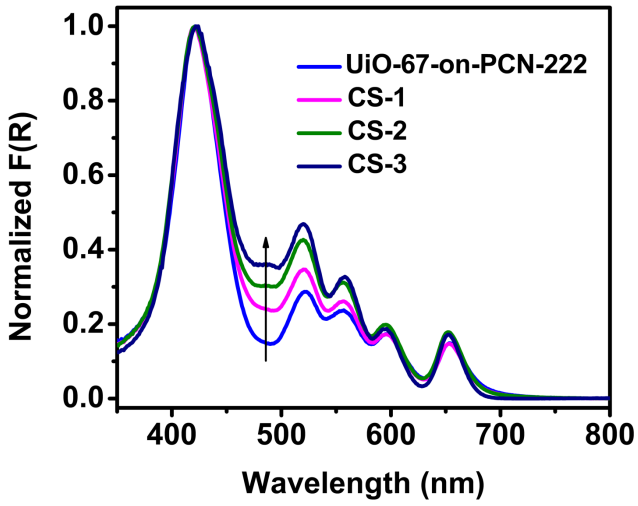

Figure 3. Diffuse reflectance spectra of UiO-67-on-PCN-222, **CS-1**, **CS-2**, **and CS-3**. The arrow indicates increasing reflectance values.

PCN-222 is a highly porous material, containing one of the largest known 1D open channels, with a diameter of up to 3.6 nm. Taking this into consideration, there is a possibility of RuDCBPY complexes getting trapped in the mesopores of PCN-222 core domain. N_2 adsorption/desorption experiments were conducted to investigate whether RuDCBPY complexes occupy the mesopores of PCN-222 core. The N_2 adsorption isotherm of the core-shell composites exhibits hysteresis loops characteristic of UiO-67 and PCN-222 MOFs (Figure 4a). Furthermore, the pore size distribution plot indicates the presence of 3.4 nm mesopores, which is a distinctive structural feature of PCN-222 MOF (Figure 4b). Based on this result, it was concluded that the mesopores of PCN-222 crystals in core domain are still accessible and not occupied by RuDCBPY complexes. It also implies that RuDCBPY is almost exclusively incorporated in the UiO-67 shell. The N_2 gas adsorption isotherm and pore size distribution plot of UiO-67-on-PCN-222 composite are provided in Supplementary Information (Section 4.6.3).

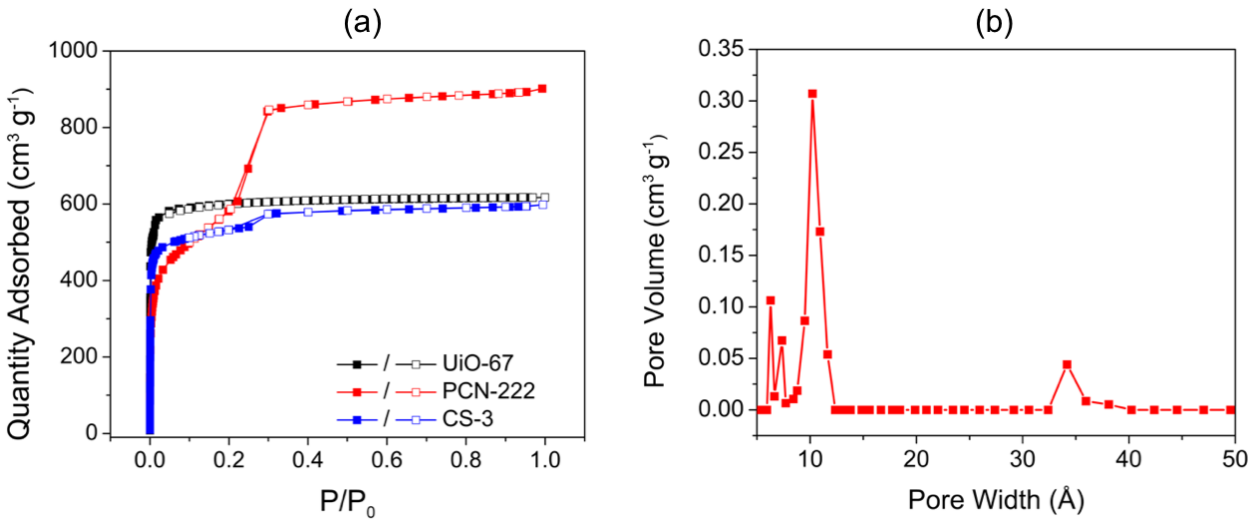

Figure 4. (a) N_2 gas adsorption isotherm of UiO-67, PCN-222, and CS-3 (core-shell composite with highest RuDCBPY loading), (b) Pore size distribution plot of CS-3. The peak at 3.4nm represents the PCN-222 mesopores.

4.4 Future Plans

1. Quantification of RuDCBPY loading in core-shell composites: In order to quantify the degree of RuDCBPY loading in the core-shell composite, two different approaches are being considered. In the first approach, known amounts of CS-1, CS-2, and CS-3 will be digested in 70% nitric acid and heated at 85 °C for 1 h. The resulting solution will be diluted with deionized water so that the final concentration of nitric acid is 7% by volume. The samples will be analyzed for Ru and Zr content using a Thermo Electron X-Series ICP mass spectrometer in accordance with Standard Method 3125-B. In the second approach, known amounts of **CS-1**, **CS-2**, and **CS-3** will be digested in a ~1M NaOH solution and electronic absorption measurements will be performed on the digested samples using an Agilent Technologies 8453 UV–Vis diode array spectrophotometer (1 nm resolution). Since the absorption spectrum of TCPP and RuDCBPY overlap with each other, "Spectral deconvolution analysis" will be performed on the resulting absorption spectra to decompose the peaks into separate additive components.[36] Absorbance of RuDCBPY will be determined at 480 nm and loading concentration calculated using the Beer-Lambert law.

2. Energy transfer investigations on RuDCBPY-doped core-shell composites: To explore the possibility of achieving interfacial energy transfer between the S_1 state of TCPP (in core domain) and ^{3}MLCT state of RuDCBPY (in shell layer), time-resolved fluorescence measurements will be performed. The time-correlated single photon counting (TCSPC) set-up will be used to excite the **CS-1**, **CS-2**, and **CS-3** samples with short pulses of light and then monitor the resulting fluorescence as a function of time. Excitation wavelength of 415 nm and emission wavelength of 660 nm will be chosen to ensure that the fluorescence signal being monitored is exclusively due

to TCPP. Additionally, steady state fluorescence measurements will be conducted on **CS-1**, **CS-2**, and **CS-3** to study the fluorescence intensity of TCPP as a function of RuDCBPY loading.

4.5 Conclusions

A series of UiO-67-on-PCN-222 core-shell composites with different loadings of RuDCBPY were synthesized and their structures characterized using various techniques. PXRD analysis of the composites confirmed that PCN-222 and UiO-67 are the constituent components of composites. SEM images of composites indicated the presence of core-shell structures along with small amounts of phase impurities (PCN-222 nanoparticles). The solvent-assisted phase separation technique, reported by Hupp and co-workers, is being utilized to isolate the composite particles.[35] Diffuse reflectance spectroscopy confirmed the varying degrees of RuDCBPY loading in composites. N_2 adsorption/desorption experiments on **CS-1**, **CS-2**, and **CS-3** suggest that mesopores of PCN-222 (in core domain) are still accessible and not occupied by RuDCBPY complexes, which means that RuDCBPY is almost exclusively incorporated in the UiO-67 shell. After completing structural characterization, time-resolved and steady state fluorescence measurements will be conducted on **CS-1**, **CS-2**, and **CS-3** to investigate the possibility of achieving interfacial energy transfer between the S_1 state of TCPP (in core domain) and ^{3}MLCT state of RuDCBPY (in shell layer).

4.6 Supplementary Information

4.6.1 Scanning electron microscopy images

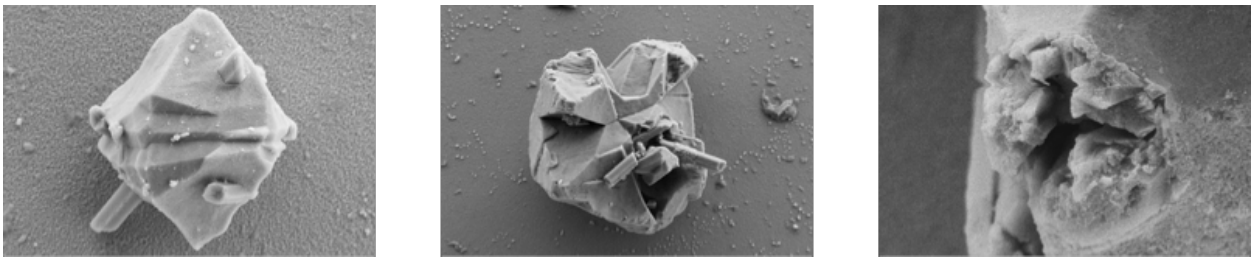

Figure S1. SEM images of UiO-67-on-PCN-222 composites

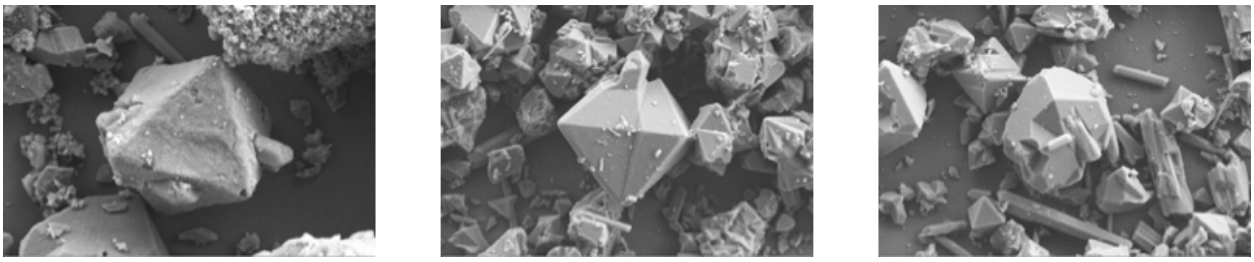

Figure S2. SEM images of CS-1 composites

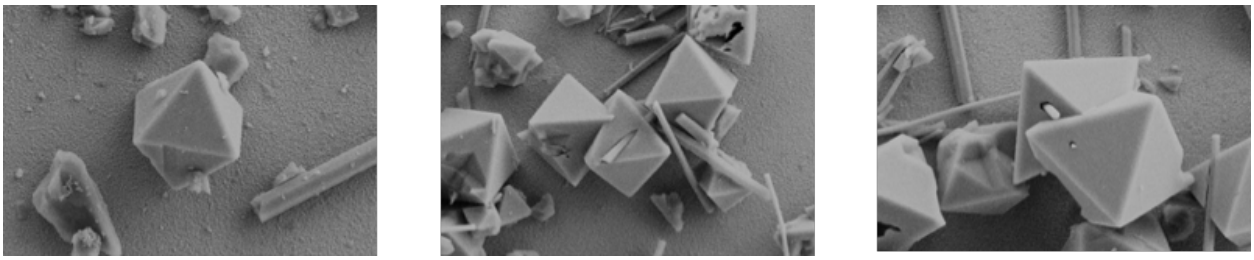

Figure S3. SEM images of CS-2 composites

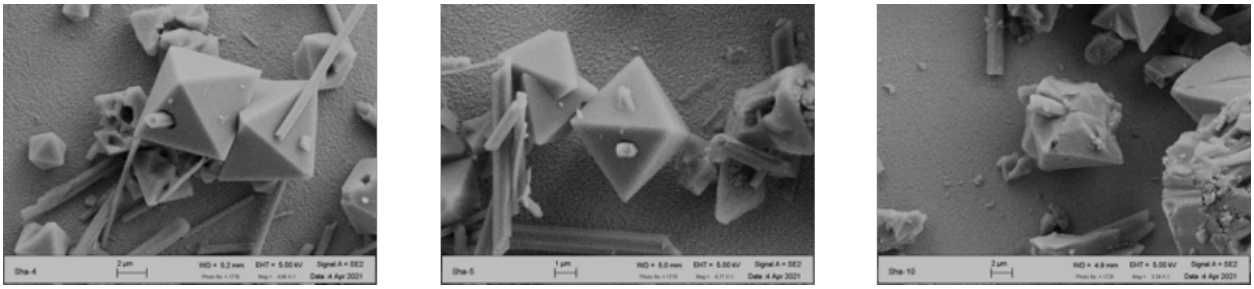

Figure S4. SEM images of CS-3 composites

4.6.2 Diffuse reflectance spectroscopy

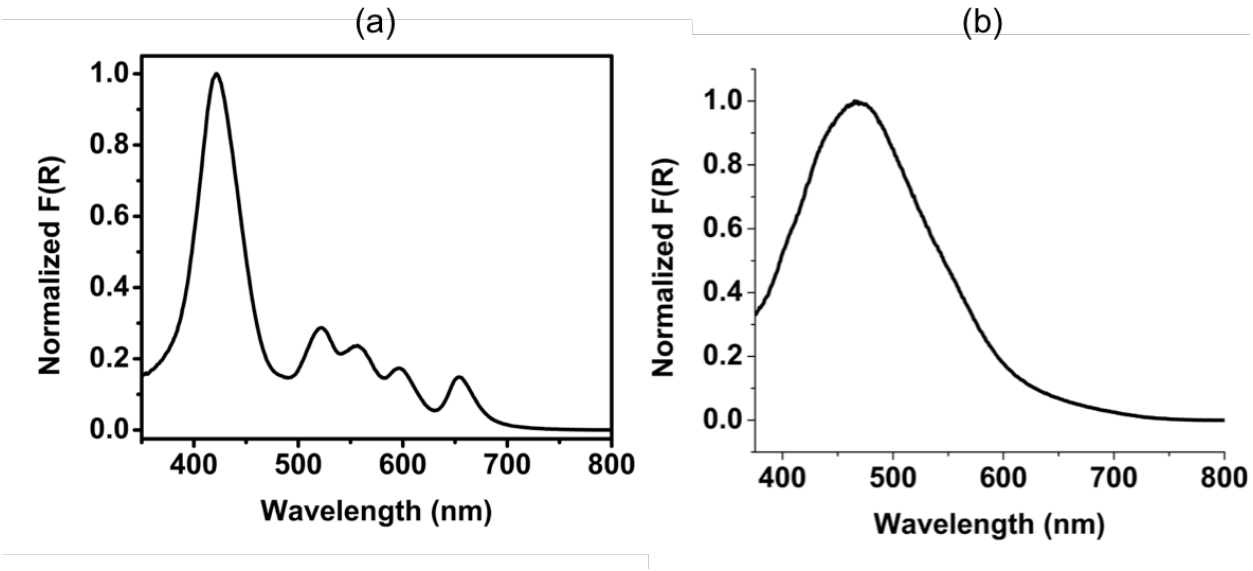

Figure S5. Diffuse reflectance spectra of (a) UiO-67-on-PCN-222 and (b) RuDCBPY

4.6.3 N_2 adsorption/desorption isotherms and pore distribution plots

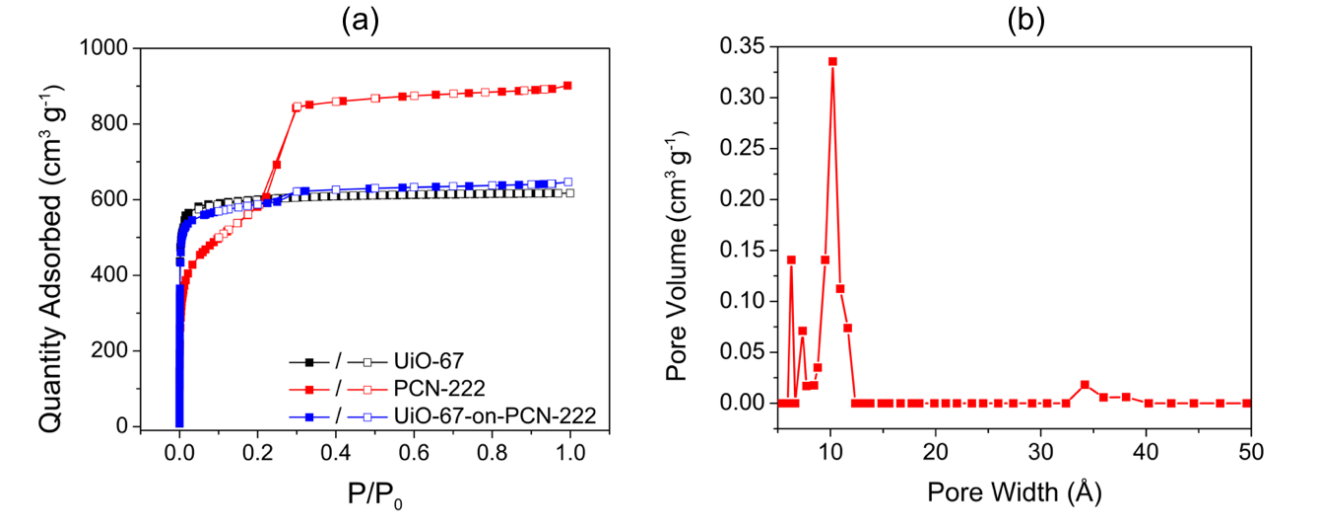

Figure S6. (a) N_2 gas adsorption isotherm of UiO-67, PCN-222, and UiO-67-on-PCN-222, (b) Pore size distribution plot of UiO-67-on-PCN-222. The peak at 3.4nm represents the PCN-222 mesopores.

4.7 References

(1) van Grondelle, R.; Novoderezhkin, V. I. Energy Transfer in Photosynthesis: Experimental Insights and Quantitative Models. *Phys Chem Chem Phys* **2006**, *8* (7), 793–807. https://doi.org/10.1039/b514032c.

(2) Mirkovic, T.; Ostroumov, E. E.; Anna, J. M.; van Grondelle, R.; Govindjee; Scholes, G. D. Light Absorption and Energy Transfer in the Antenna Complexes of Photosynthetic Organisms. *Chem. Rev.* **2017**, *117* (2), 249–293. https://doi.org/10.1021/acs.chemrev.6b00002.

(3) Park, H.; Heldman, N.; Rebentrost, P.; Abbondanza, L.; Iagatti, A.; Alessi, A.; Patrizi, B.; Salvalaggio, M.; Bussotti, L.; Mohseni, M.; et al. Enhanced Energy Transport in Genetically Engineered Excitonic Networks. *Nat. Mater.* **2016**, *15* (2), 211–216. https://doi.org/10.1038/nmat4448.

(4) Sola-Llano, R.; Fujita, Y.; Gómez-Hortigüela, L.; Alfayate, A.; Uji-i, H.; Fron, E.; Toyouchi, S.; Pérez-Pariente, J.; López-Arbeloa, I.; Martínez-Martínez, V. One-Directional Antenna Systems: Energy Transfer from Monomers to J-Aggregates within 1D Nanoporous Aluminophosphates. *ACS Photonics* **2018**, *5* (1), 151–157. https://doi.org/10.1021/acsphotonics.7b00553.

(5) Maity, D.; Bhaumik, C.; Mardanya, S.; Karmakar, S.; Baitalik, S. Light Harvesting and Directional Energy Transfer in Long-Lived Homo- and Heterotrimetallic Complexes of FeII, RuII, and OsII. *Chem. – A Eur. J.* **2014**, *20* (41), 13242–13252. https://doi.org/https://doi.org/10.1002/chem.201402591.

(6) Zhou, X.; Mandal, S.; Jiang, S.; Lin, S.; Yang, J.; Liu, Y.; Whitten, D. G.; Woodbury, N. W.; Yan, H. Efficient Long-Range, Directional Energy Transfer through DNA-Templated

Dye Aggregates. *J. Am. Chem. Soc.* **2019**, *141* (21), 8473–8481. https://doi.org/10.1021/jacs.9b01548.

(7) Son, H.-J.; Jin, S.; Patwardhan, S.; Wezenberg, S. J.; Jeong, N. C.; So, M.; Wilmer, C. E.; Sarjeant, A. A.; Schatz, G. C.; Snurr, R. Q.; et al. Light-Harvesting and Ultrafast Energy Migration in Porphyrin-Based Metal–Organic Frameworks. *J. Am. Chem. Soc.* **2013**, *135* (2), 862–869. https://doi.org/10.1021/ja310596a.

(8) Chen, G.; Damasco, J.; Qiu, H.; Shao, W.; Ohulchanskyy, T. Y.; Valiev, R. R.; Wu, X.; Han, G.; Wang, Y.; Yang, C.; et al. Energy-Cascaded Upconversion in an Organic Dye-Sensitized Core/Shell Fluoride Nanocrystal. *Nano Lett.* **2015**, *15* (11), 7400–7407. https://doi.org/10.1021/acs.nanolett.5b02830.

(9) Liu, J.; Kaczmarek, A. M.; Artizzu, F.; Van Deun, R. Ultraefficient Cascade Energy Transfer in Dye-Sensitized Core/Shell Fluoride Nanoparticles. *ACS Photonics* **2019**, *6* (3), 659–666. https://doi.org/10.1021/acsphotonics.8b01465.

(10) Ghosh Chaudhuri, R.; Paria, S. Core/Shell Nanoparticles: Classes, Properties, Synthesis Mechanisms, Characterization, and Applications. *Chem. Rev.* **2012**, *112* (4), 2373–2433. https://doi.org/10.1021/cr100449n.

(11) Zhou, B.; Tao, L.; Chai, Y.; Lau, S. P.; Zhang, Q.; Tsang, Y. H. Constructing Interfacial Energy Transfer for Photon Up- and Down-Conversion from Lanthanides in a Core–Shell Nanostructure. *Angew. Chemie Int. Ed.* **2016**, *55* (40), 12356–12360. https://doi.org/https://doi.org/10.1002/anie.201604682.

(12) Liu, J.; Fu, T.; Shi, C. Spatial Energy Transfer and Migration Model for Upconversion Dynamics in Core–Shell Nanostructures. *J. Phys. Chem. C* **2019**, *123* (14), 9506–9515. https://doi.org/10.1021/acs.jpcc.8b12300.

(13) Jin, S. Y.; Son, H. J.; Farha, O. K.; Wiederrecht, G. P.; Hupp, J. T. Energy Transfer from Quantum Dots to Metal-Organic Frameworks for Enhanced Light Harvesting. *J. Am. Chem. Soc.* **2013**, *135*, 955–958. https://doi.org/Doi 10.1021/Ja3097114.

(14) Zhang, Q.; Zhang, C.; Cao, L.; Wang, Z.; An, B.; Lin, Z.; Huang, R.; Zhang, Z.; Wang, C.; Lin, W. Förster Energy Transport in Metal-Organic Frameworks Is beyond Step-by-Step Hopping. *J. Am. Chem. Soc.* **2016**, *138* (16), 5308–5315. https://doi.org/10.1021/jacs.6b01345.

(15) Lee, C. Y.; Farha, O. K.; Hong, B. J.; Sarjeant, A. a; Nguyen, S. T.; Hupp, J.; Hupp, J. T. Strut-to-Strut Energy Transfer in Bodipy and Porphyrin-Based MOFs Light-Harvesting Metal-Organic Frameworks (MOFs): Effi- Cient Strut-to-Strut Energy Transfer in Bodipy and Porphyrin- Based MOFs. *Synthesis (Stuttg)*. **2011**, 15858–15861.

(16) Zhu, J.; Shaikh, S.; Mayhall, N. J.; Morris, A. J. Energy Transfer in Metal-Organic Frameworks. In *Elaboration and Applications of Metal-Organic Frameworks*; Series on Chemistry, Energy and the Environment; WORLD SCIENTIFIC, 2017; Vol. Volume 2, pp 581–654. https://doi.org/doi:10.1142/9789813226739_0014.

(17) Zhu, J.; Maza, W. A.; Morris, A. J. Light-Harvesting and Energy Transfer in Ruthenium(II)-Polypyridyl Doped Zirconium(IV) Metal-Organic Frameworks: A Look toward Solar Cell Applications. *J. Photochem. Photobiol. A Chem.* **2017**, *344*, 64–77. https://doi.org/https://doi.org/10.1016/j.jphotochem.2017.04.025.

(18) Kent, C. A.; Mehl, B. P.; Ma, L.; Papanikolas, J. M.; Meyer, T. J.; Lin, W. Energy Transfer Dynamics in Metal-Organic Frameworks. *J. Am. Chem. Soc.* **2010**, *132* (37), 12767–12769. https://doi.org/10.1021/ja102804s.

(19) Son, H. J.; Jin, S.; Patwardhan, S.; Wezenberg, S. J.; Jeong, N. C.; So, M.; Wilmer, C. E.;

Sarjeant, A. A.; Schatz, G. C.; Snurr, R. Q.; et al. Light-Harvesting and Ultrafast Energy Migration in Porphyrin-Based Metal-Organic Frameworks. *J. Am. Chem. Soc.* **2013**, *135* (2), 862–869. https://doi.org/10.1021/ja310596a.

(20) Shaikh, S.; Chakraborty, A.; Alatis, J.; Cai, M.; Danilov, E. O.; Morris, A. J. Light Harvesting and Energy Transfer in a Porphyrin-Based Metal Organic Framework. *Faraday Discuss.* **2018**. https://doi.org/10.1039/C8FD00194D.

(21) Patwardhan, S.; Jin, S.; Son, H.-J.; Schatz, G. C. Ultrafast Energy Migration in Porphyrin-Based Metal Organic Frameworks (MOFs). *Mater. Res. Soc. Symp. Proc.* **2013**, *1539*, 22–27. https://doi.org/10.1557/opl.2013.987.

(22) Rajasree, S. S.; Li, X.; Deria, P. Physical Properties of Porphyrin-Based Crystalline Metal–organic Frameworks. *Commun. Chem.* **2021**, *4* (1), 47. https://doi.org/10.1038/s42004-021-00484-4.

(23) So, M. C.; Wiederrecht, G. P.; Mondloch, J. E.; Hupp, J. T.; Farha, O. K. Metal-Organic Framework Materials for Light-Harvesting and Energy Transfer. *Chem. Commun.* **2015**, *51* (17), 3501–3510. https://doi.org/10.1039/C4CC09596K.

(24) Furukawa, H.; Cordova, K. E.; O'Keeffe, M.; Yaghi, O. M. The Chemistry and Applications of Metal-Organic Frameworks. *Science (80-.).* **2013**, *341* (August), 974. https://doi.org/10.1126/science.1230444.

(25) Sun, Y.; Zhou, H.-C. Recent Progress in the Synthesis of Metal–Organic Frameworks. *Sci. Technol. Adv. Mater.* **2015**, *16* (5), 054202. https://doi.org/10.1088/1468-6996/16/5/054202.

(26) Lee, J.; Farha, O. K.; Roberts, J.; Scheidt, K. A.; Nguyen, S. T.; Hupp, J. T. Metal-Organic Framework Materials as Catalysts. *Chem. Soc. Rev.* **2009**, *38* (5), 1450–1459.

https://doi.org/10.1039/B807080F.

(27) Allendorf, M. D.; Bauer, C. A.; Bhakta, R. K.; Houk, R. J. T. Luminescent Metal–Organic Frameworks. *Chem. Soc. Rev.* **2009**, *38* (5), 1330–1352. https://doi.org/10.1039/B802352M.

(28) Li, J.-R.; Kuppler, R. J.; Zhou, H.-C. Selective Gas Adsorption and Separation in Metal-Organic Frameworks. *Chem. Soc. Rev.* **2009**, *38* (5), 1477–1504. https://doi.org/10.1039/B802426J.

(29) Horcajada, P.; Serre, C.; Vallet-Regí, M.; Sebban, M.; Taulelle, F.; Férey, G. Metal–Organic Frameworks as Efficient Materials for Drug Delivery. *Angew. Chemie* **2006**, *118* (36), 6120–6124. https://doi.org/10.1002/ange.200601878.

(30) Horcajada, P.; Chalati, T.; Serre, C.; Gillet, B.; Sebrie, C.; Baati, T.; Eubank, J. F.; Heurtaux, D.; Clayette, P.; Kreuz, C.; et al. Porous Metal–Organic-Framework Nanoscale Carriers as a Potential Platform for Drug Delivery and Imaging. *Nat. Mater.* **2009**, *9*, 172.

(31) Yang, X.; Yuan, S.; Zou, L.; Drake, H.; Zhang, Y.; Qin, J.; Alsalme, A.; Zhou, H.-C. One-Step Synthesis of Hybrid Core–Shell Metal–Organic Frameworks. *Angew. Chemie Int. Ed.* **2018**, *57* (15), 3927–3932. https://doi.org/10.1002/anie.201710019.

(32) Maza, W. A.; Morris, A. J. Photophysical Characterization of a Ruthenium(II) Tris(2,2′-Bipyridine)-Doped Zirconium UiO-67 Metal–Organic Framework. *J. Phys. Chem. C* **2014**, *118* (17), 8803–8817. https://doi.org/10.1021/jp501140r.

(33) Maza, W. A.; Padilla, R.; Morris, A. J. Concentration Dependent Dimensionality of Resonance Energy Transfer in a Postsynthetically Doped Morphologically Homologous Analogue of UiO-67 MOF with a Ruthenium(II) Polypyridyl Complex. *J. Am. Chem. Soc.* **2015**, *137* (25), 8161–8168. https://doi.org/10.1021/jacs.5b03071.

(34) Flamigni, L.; Armaroli, N.; Barigelletti, F.; Balzani, V.; Collin, J.-P.; Dalbavie, J.-O.; Heitz, V.; Sauvage, J.-P. Photoinduced Processes in Dyads Made of a Porphyrin Unit and a Ruthenium Complex. *J. Phys. Chem. B* **1997**, *101* (31), 5936–5943. https://doi.org/10.1021/jp963773b.

(35) Farha, O. K.; Mulfort, K. L.; Thorsness, A. M.; Hupp, J. T. Separating Solids: Purification of Metal-Organic Framework Materials. *J. Am. Chem. Soc.* **2008**, *130* (27), 8598–8599. https://doi.org/10.1021/ja803097e.

(36) Blass, W. E.; Halsey, G. W. CHAPTER 1 - INTRODUCTION; Blass, W. E., Halsey, G. W. B. T.-D. of A. S., Eds.; Academic Press, 1981; pp 1–12. https://doi.org/https://doi.org/10.1016/B978-0-12-104650-7.50005-6.

(37) Wu, M.-X.; Wang, Y.; Zhou, G.; Liu, X. Core–Shell MOFs@MOFs: Diverse Designability and Enhanced Selectivity. *ACS Appl. Mater. Interfaces* **2020**, *12* (49), 54285–54305. https://doi.org/10.1021/acsami.0c16428.

5. Summary and Future Directions

5.1 Summary of Results

Chapter 1: Light harvesting antenna complexes (LHC's) in natural photosynthetic systems perform multistep energy cascade processes, where the first step is light absorption by chlorophyll and carotenoid pigments incorporated within the antenna assembly. The energy is then directionally transported to the reaction centers (PSI and PSII). The reactions centers use this energy to drive charge separation and perform dark-phase chemical reactions that generate biomolecules. The precise arrangement of pigment chromophores modulates interchromophoric interactions, which in turn determines the photophysical behavior and energy transfer dynamics in LHC's. Artificial molecular assemblies that can mimic the LHC's, in terms of the efficiency and directionality of energy transfer, are highly desirable. In order to mimic the LHC's, it is necessary to first understand how the chemical composition and structural organization of pigment chromophores influences the efficiency and directionality of energy transfer in LHC's. To achieve this objective, scientists have designed a wide-range of molecular and supramolecular constructs that can serve as model systems for studying energy transfer. In this chapter, we present examples of artificial model systems that investigate the effect of (a) photophysical properties of chromophores, (b) interchromophoric distances, and (c) relative orientation of chromophores on energy transfer. Energy transfer in rhenium-based molecular assemblies, porphyrin-based Donor−Bridge−Acceptor systems, pyrene- and porphyrin-based dendrimers, and conjugated polymers are discussed.

Photoactive metal-organic frameworks constitute an attractive class of nanoscale materials due to their light-harvesting, energy transfer and photocatalytic activities. With large photon

absorptivity, the frameworks provide novel energy-transfer pathways enabling long-distance energy migration both in singlet and triplet manifolds. MOFs demonstrate a high degree of structural flexibility that affords an opportunity to coordinatively attach different types of chromophores as linkers. The crystalline nature of MOFs allows for precise control of distances and orientations between chromophores by judicious choice of ligands and metal nodes. These qualities make MOFs ideal candidates to study energy transfer as a function of chromophoric properties and structural parameters. This chapter also provides examples of MOF-based systems that have explored the role of chromophoric properties and structural parameters in energy transfer. Energy transfer in porphyrin-based MOFs (crystalline powders and thin films) and ruthenium-based MOFs is discussed.

Chapter 2: We present a detailed investigation of the photophysical properties of mixed-ligand pyrene- and porphyrin-based metal organic frameworks as a function of their 3D structure. Solvothermal reactions between metal salts ($InCl_3$, $Zr(acac)_4$, $ZrCl_4$) and suitable ratios of 1,3,6,8-tetrakis(p-benzoic acid)pyrene (TBAPy) and meso-tetrakis(4-carboxyphenyl)porphyrin (TCPP) were performed to prepare a series of mixed-ligand ROD-7, NU-901 and NU-1000 MOFs. Time resolved and steady state fluorescence measurements were conducted on the mixed-ligand MOFs to study their photophysics. Based on the results, we concluded that upon excitation of TBAPy linkers in the MOFs, singlet excitation energy migrates across TBAPy linkers until it finds a TCPP unit. TCPP acts as an energy trap and quenches the excitation.[1-3] The efficiency of TBAPy-to-TBAPy energy transfer was found to be sensitive to the structural parameters of MOFs. Stern-Volmer analysis of TBAPy lifetime data revealed that energy transfer is most efficient in ROD-7, followed by NU-901 and NU-1000. Excitation energy transfer (EET) efficiencies (calculated using steady state fluorescence data) agreed with the results of Stern-Volmer analysis. We propose that

(a) shorter interchromophoric distances, (b) co-facial arrangement of TBAPy linkers and (c) larger spectral overlap integral (*J*) are responsible for higher EET efficiency in ROD-7. The strength of electronic coupling between the excited states of donor and acceptor chromophores is influenced by their separation distance, a shorter distance resulting in stronger coupling. Similarly, co-facial arrangement of TBAPy linkers ensures that the transition dipole moments of donor and acceptor are aligned favorably to undergo rapid energy transfer. Excitonic coupling calculations were also performed to determine energy transfer rate constants along different directions and assess the directionality of energy transfer in these MOFs.[4] The magnitude of rate constants indicated that energy transfer in ROD-7 should be highly anisotropic along the stacking direction. These findings suggest that ROD-7 is a promising candidate to play the role of the light harvesting and energy-transfer component in solar energy conversion devices, where directional energy transfer is required.

Chapter 3: We present synthesis and photophysical characterization of a water stable PCN-223(freebase) MOF constructed from meso-tetrakis(4-carboxyphenyl)porphyrin (TCPP). Photophysical properties of the synthesized crystalline material were studied by using a wide range of steady-state and time-resolved spectroscopic techniques. Quenching experiments performed on TCPP and PCN-223 demonstrated that the extent and the rate of quenching in the MOF is significantly higher than in the monomeric ligand. Based on these results, we propose that upon photo-excitation, the excitation energy migrates across neutral TCPP linkers until it is quenched by a N-protonated TCPP linker. The N-protonated linkers act as trap states that deactivate the excited state to the ground state. Variable temperature measurements aided in understanding the mechanism of singlet-singlet energy transfer in PCN-223 MOF. The rate of energy transfer and the total exciton hopping distance in PCN-223 were calculated to quantify the energy transfer

characteristics of PCN-223. Nanosecond transient absorption spectroscopy was used to study the triplet excited state photophysics in both free ligand and PCN-223 MOF. Furthermore, femtosecond transient absorption spectroscopy was employed to get a better understanding of the photophysical processes taking place in ligand and MOF on ultrafast timescales. Efficient energy transfer (Förster radius = 54.5 Å) accompanied with long distance exciton hopping (173 Å) was obtained for PCN-223 MOF.

Chapter 4 (Ongoing project): Optical materials that allow control over the directionality of energy transfer are highly desirable for light-harvesting applications and photocatalysis. MOF-on-MOF composites with core-shell architecture provide a unique platform for studying directional energy transfer.[5] We report synthesis and structural characterization of UiO-67-on-PCN-222 core-shell composites that can be used as model systems for exploring directional energy transfer. Suitable amounts of Ruthenium(II) tris(5,5′-dicarboxy-2,2′-bipyridine), RuDCBPY, were doped in the shell layer to produce a series of Ru-UiO-67-on-PCN-222 composites with varying degree of RuDCBPY loading. We hypothesize that upon photo-excitation of TCPP units in the core, interfacial energy transfer should occur from the lowest singlet excited sate of TCPP (S_1) to the triplet metal-to-ligand charge-transfer state of RuDCBPY (^{3}MLCT). Powder X-ray diffraction (PXRD), scanning electron microscopy (SEM) imaging, N_2 adsorption-desorption isotherms, and diffuse reflectance spectroscopy were employed for structural characterization. After completing structural characterization, time-resolved fluorescence measurements will be performed on the MOFs to elucidate the dynamics of interfacial energy transfer. Steady state fluorescence measurements will also be conducted on the Ru-UiO-67-on-PCN-222 composites to study the fluorescence intensity of TCPP as a function of RuDCBPY loading.

5.2 Future Directions

The work presented in this dissertation has provided insight into the role of 3D structure of MOFs in energy transfer. The highly efficient energy transfer demonstrated by ROD-7 and PCN-223 suggests that these MOFs can potentially serve as the light harvesting and energy-transfer component in artificial light harvesting devices. ROD-7, in particular, is very attractive due to the highly anisotropic EET along its stacking direction. Future studies on ROD-7 should focus on exploring the ultrafast photophysical processes taking place in mixed-ligand ROD-7 MOFs. Transient absorption spectroscopic data in the femtosecond time domain will provide useful information regarding k_{EET} and also shed light on the mechanism of EET.[6] It will be interesting to explore whether the EET process in ROD-7 is coherent or incoherent or a combination of both. Due to the short interchromophoric distance (~7Å) and large κ^2 value (1.00) in ROD-7, a coherent EET process cannot be completely ruled out. Incorporation of ROD-7 in a core-shell MOF composite is extremely attractive because its geometrical layout is conducive for achieving directional energy transfer. A core-shell composite consisting of ROD-7 and a TCPP-based MOF should enable efficient, directional energy transfer. Fabrication of ROD-7 in thin-film form should also be pursued to facilitate its integration in solar energy conversion devices.

5.3 References

(1) Porcu, P.; Vonlanthen, M.; Ruiu, A.; González-Méndez, I.; Rivera, E. Energy Transfer in Dendritic Systems Having Pyrene Peripheral Groups as Donors and Different Acceptor Groups. *Polymers* . 2018. https://doi.org/10.3390/polym10101062.

(2) Zaragoza-Galán, G.; Fowler, M.; Rein, R.; Solladié, N.; Duhamel, J.; Rivera, E. Fluorescence Resonance Energy Transfer in Partially and Fully Labeled Pyrene Dendronized Porphyrins Studied with Model Free Analysis. *J. Phys. Chem. C* **2014**, *118*

(16), 8280–8294. https://doi.org/10.1021/jp501445n.

(3) Rojas-Montoya, S. M.; Vonlanthen, M.; Porcu, P.; Flores-Rojas, G.; Ruiu, A.; Morales-Morales, D.; Rivera, E. Synthesis and Photophysical Properties of Novel Pyrene–Metalloporphyrin Dendritic Systems. *Dalt. Trans.* **2019**, *48* (28), 10435–10447. https://doi.org/10.1039/C9DT00855A.

(4) Kistler, K. A.; Spano, F. C.; Matsika, S. A Benchmark of Excitonic Couplings Derived from Atomic Transition Charges. *J. Phys. Chem. B* **2013**, *117* (7), 2032–2044. https://doi.org/10.1021/jp310603z.

(5) Yang, X.; Yuan, S.; Zou, L.; Drake, H.; Zhang, Y.; Qin, J.; Alsalme, A.; Zhou, H.-C. One-Step Synthesis of Hybrid Core–Shell Metal–Organic Frameworks. *Angew. Chemie Int. Ed.* **2018**, *57* (15), 3927–3932. https://doi.org/10.1002/anie.201710019.

(6) Gutiérrez Tovar, M.; Cohen, B.; Sánchez, F.; Douhal, A. Zr-Based MOFs Photochemistry: Ligand-to-Cluster Charge Transfer, Energy Transfer and Excimer Formation, What Else Is There? *Phys. Chem. Chem. Phys.* **2016**, *18* (40), 27761–27774. https://doi.org/10.1039/C6CP03791G.